Femtochemistry and Reactive Intermediates:

Application to Atmospheric and Organic Chemistry

Thesis by

Jennifer L. Herek

In Partial Fulfillment of the Requirements for the Degree of
Doctor of Philosophy

California Institute of Technology
Pasadena, California
1996

(submitted 6 June 1996)

Acknowledgments

While this thesis bears the name of a single author, it is nonetheless the product of the combined efforts of many. Foremost amongst these is my advisor, Professor Ahmed Zewail, whose guidance, encouragement, and, most of all, belief in my ability to do science has carried me through much of my graduate career. I thank him for the opportunity to work and play in Femtoland, and to collaborate with many talented scientists. I would also like to thank my other mentors, Professor John Brandenberger of Lawrence University and Dr. Ralph Weston, Jr. of Brookhaven National Laboratory; without their support and encouragement I would likely not have made it to (and through) Caltech.

I have perhaps learned the most from interactions with my colleagues, not only scientifically, but also culturally and personally. I feel fortunate to have worked with such a great group of people. All of the members of the Zewail group, past and present, are warmly thanked for many stimulating interactions, especially Amine Mokhtari, Peijun Cong, Bob Bowman, Marcos Dantus, Martin Gruebele, Thomas Baumert, Arnulf Materny, Sang Kyu Kim, Søren Pedersen, Marcos Motzkus, and Brent Horn. Earl Potter, Dean Willberg, and Chuck Williamson deserve special recognition for always being there throughout the many ups and downs.

My association with the Weitekamp group extends beyond coffee club membership; I am grateful to all of them for providing scientific perspective and friendship. I would also like to acknowledge the Bercaw and Dougherty groups, especially Roger Quan and Kraig Anderson, for assisting with sample preparation (for those times when it didn't come out of a bottle). They made my work a lot easier and I thank them.

I have made many friendships over the past six years which greatly enriched my experience. Thanks to Alison McCurdy, Sakae Suzuki, Geoffrey Smith, Richard

iii

Chou and family, Chuck Williamson and Jeanine Renne, Len and Shelley Mueller, John Marohn and Patty Sipman, Paul Carson, and especially Jim Kempf. Amy Zesbaugh and Soozung Sa, while far from Caltech, provided frequent reality checks and helped me keep things in perspective.

Finally, I'd like to dedicate this thesis to my family, both near and far, for their unending support and encouragement, for which thanks have too frequently gone unsaid. Thank you Mom, Dad, Keith, and Lee, for always being there for me. And to Ted, Terri, Emma, Britti, and Alan — thank you for letting me be a part of your family these last "couple of months."

Abstract

The logical sequence of primary steps in a reaction mechanism is governed by the reactive intermediates which are postulated to ensure smooth transformations between stable species. Historically, such constructs were merely hypothetical as their (assumed) extreme reactivity and/or unstable nature precluded their observation. The introduction of femtosecond lasers to chemistry has allowed insight and understanding to many fundamental processes in reaction dynamics. This thesis presents applications of femtosecond spectroscopy to atmospheric and organic chemistry, specifically probing the reactive intermediates mediating various chemical transformations. Direct observation of these fleeting species can validate previously proposed mechanisms as well as offer new perspectives to their reaction dynamics.

Studies of diradicals, the molecular species hypothesized to be archetypal of chemical bond transformations in many reactions in organic chemistry, have been made using femtosecond laser techniques combined with mass spectrometry in a molecular beam. Evolution of the diradical intermediate is monitored in real time throughout the course of the chemical reaction. These studies offer the first direct evidence of singlet 1,3- and 1,4-diradicals.

Hydrogen-atom transfer processes are fundamental to many reactions in organic chemistry. The dynamics of the motion may be localized, with little nuclear motion aside from the H-atom transfer between two "anchors," or may be global, involving a multidimensional potential. Using methyl salicylate as a prototype system, direct studies of the nuclear motion in this important transformation are made with femtosecond resolution.

Many reactive intermediates have been linked to stratospheric ozone depletion in recent years. In particular, catalytic cycles involving halogens are considered critical to establishing the overall mechanism for ozone depletion. Direct studies of the photochemically-activated dissociation of key species in atmospheric chemistry can offer insight to the global dynamics by providing important rate constants and branching ratios. Femtosecond reaction dynamics of OClO in a supersonic molecular beam are reported. The observations reveal the nuclear motions and couplings between potential energy surfaces relevant to the dissociation process. Comparisons with results of ab initio calculations are made.

Table of Contents

Standard Terms and Abbreviations

CB	Cyclobutanone
d_2-CB	3,3-d_2-cyclobutanone
d_4-CB	2,2,4,4-d_4-cyclobutanone
CP	Cyclopentanone
d_4-CP	2,2,5,5-d_4-cyclopentanone
CPM	Colliding-pulse mode-locked laser
DEA	*N,N*-Diethylaniline
DODCI	3,3'-diethyloxadicarbocyanine iodide, CPM saturable absorber dye
fs	Femtoseconds
fwhm	Full width at half maximum
Hz	Hertz
KDP	Potassium dihydrogen phosphate
μm	Micrometers
MPI	Multi-photon ionization
MS	Methyl salicylate
μs	Microseconds
Nd:YAG	Neodymium:Yttrium-Aluminum-Garnet
nm	Nanometers
ns	Nanoseconds
OClO	Chlorine Dioxide
PDA	Pulsed dye amplifier
ps	Picosecond
R590	Rhodamine tetrafluoroborate, CPM gain dye
SHG	Second harmonic generation
S/N	Signal to noise
t_0	Time zero; the time at which the pump and probe pulses are temporally overlapped.
t_d	Time delay between pump and probe pulses
TOF	Time of Flight

Introduction

Behind the scenes of any production lies the real action. When stage lights dim between the scenes of a play, a few frantic moments of changing costumes and arranging props and sets provide continuity in the flow of the story. In general, the audience misses the activity that transforms actor and stage, though is blindly aware of the changes involved. The main stage for chemistry involves similar choreography. The drama of chemical transformation is mediated by fleeting intermediates and transition-state species that provide continuity between the steps of a reaction mechanism.

First introduced in 1987,[1] techniques of femtosecond spectroscopy are a means of peering "behind the scenes" of a chemical reaction. The fundamental dynamics of bond-breaking and bond-formation processes in many classes of chemical reactions can be observed directly with temporal resolution characteristic of the nuclear motion (see Refs. 2 and 3, and references therein). Figure 1 shows the breadth and range of applications of femtosecond spectroscopy to systems in physics, chemistry, and biology. As the field has matured, the novelty of simply observing nuclear dynamics has been replaced by a quest to choreograph them. The future of femtochemistry will build upon the insight and understanding gleaned from studies of fundamental molecular dynamics in designing and directing new productions of chemical transformation. Indeed, steps to that end have already been taken; control of branching ratios and product formation by femtosecond techniques have already been demonstrated in simple molecular systems (for examples from this laboratory, see Refs. 4-6).

LIQUIDS

Coherent Dissociation
Geminate Recombination
Dephasing
Proton Transfer
Electron Transfer
Vibrational Relaxation
Barrierless Reactions
Bimolecular Reactions
Ionic Reactions
Solvation Dynamics
Friction Dynamics
Polarization

GAS PHASE

Barrier Reactions
Electron Transfer
vdW Reactions
Rydberg Reactions
Exchange Reactions
Cycloaddition Reactions
Norrish Reactions
Dissociation
Proton/H-atom Transfer
Bimolecular Reactions
Isomerization
Elimination Reactions

SOLIDS

Caging Reactions
Harpoon Reactions
Excimers
Exciplexes
Polymer Reactions
Semiconductor Reactions

Femtosecond Resolution in Physics, Chemistry, & Biology

CONTROL

r^* t^*

Φ^* $V^*(\varepsilon)$

CLUSTERS

Acid-Base Reactions
Stepwise Solvation
Metal Clusters
Ionization Dynamics
Coulomb Explosion
Ion-Molecule Reactions
Cage Effect
Proton Transfer

DENSE FLUIDS

Dissociation Reactions
Recombination Reactions
Dephasing
Vibrational Relaxation

SURFACES

Desorption
Melting
Molecular Structure Changes
Electron Transfer
Femto-STM dynamics

BIOLOGICAL SYSTEMS

Ligand-myoglobin
Protein Dynamics
Bacteriorhodopsin
Light-harvesting
Pigment-protein Complexes
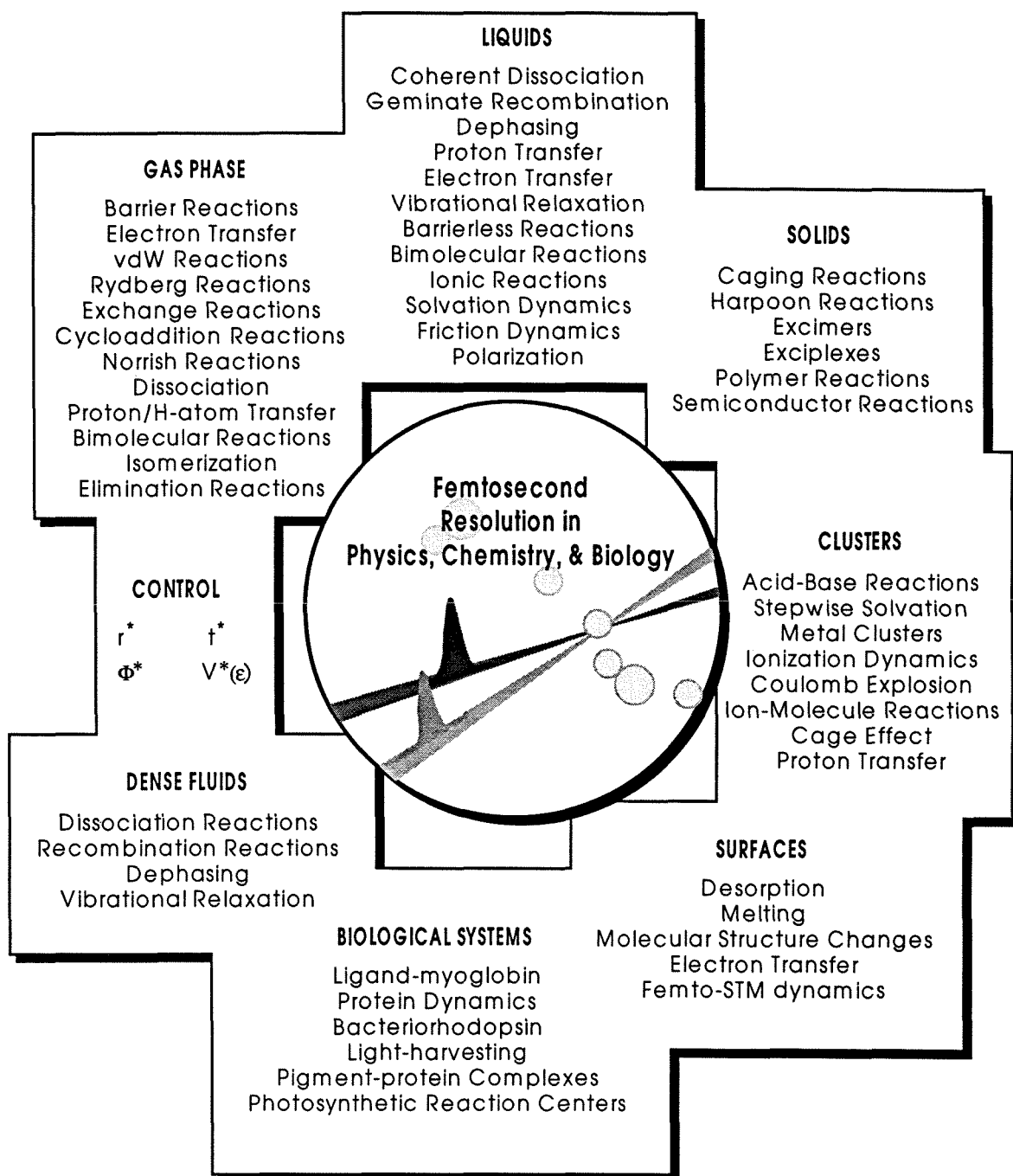Photosynthetic Reaction Centers

Figure 1   Applications of femtosecond spectroscopy to studies in physics, chemistry, and biology (adapted from Ref. 7).

This thesis relates applications of femtosecond spectroscopy to organic and atmospheric chemistry, two research areas in which the fundamental dynamics of reactive intermediates are critical in solving mechanistic puzzles. The challenge of contributing to a global understanding of the precise mechanism of stratospheric ozone depletion and the reward of uncovering fine details of classic reactions in organic chemistry motivate these studies. Chapters 1 and 2 discuss the general concept of femtosecond spectroscopy and the experimental methodology while the remainder of the thesis is devoted to its application to three distinct chemical systems. All of this work has been performed in collaboration with several coworkers; the contributors to each project are detailed below.

Chapters 3 and 4 present results of our work on trimethylene and tetramethylene diradicals, reactive intermediates which characterize chemical bond transformations in many classes of organic reactions. Preliminary results have been published in *Science*,[8] but the account given here is the most complete to date. Søren Pedersen was a collaborator and co-author on the early work, especially regarding the experiments on tetramethylene and related 1,4-diradicals. Kraig Anderson (Caltech) contributed immensely to these experiments by synthesizing numerous precursor molecules. A sample of deuterium-labeled cyclobutanone was also provided by Prof. John Baldwin (Syracuse University).

Chapter 5 reports studies of intramolecular hydrogen-atom transfer dynamics within the prototype system of methyl salicylate. The experiments were performed in collaboration with Søren Pedersen and Luis Bañares, and have been published in the Journal of Chemical Physics.[9] The version here is nearly identical, with the exception that the Appendix (which details the construction of a kinetic model illustrative of the transfer dynamics) has been omitted. A thorough discussion of kinetic models in reaction dynamics can be found in Ref. 10.

Chapter 6 presents our foray into atmospheric chemistry, detailing studies of the photodissociation of chlorine dioxide, a key player in many catalytic cycles resulting in net losses of ozone. Thomas Baumert collaborated on this project, the results of which were published in the Journal of Chemical Physics.[11] The discussion here has been updated to include more recent considerations on the role of halogen compounds in stratospheric ozone depletion.

Other research projects, not detailed in this thesis, include femtosecond control of reaction dynamics,[5,6] studies of the photodissociation of NaI,[12-14] and recent work on understanding the mechanism of the retro Diels-Alder reaction.[15]

References

[1] M. Dantus, M. J. Rosker, and A. H. Zewail, J. Chem. Phys. **87**, 2395 (1987).

[2] A. H. Zewail, *Femtochemistry: Ultrafast Dynamics of the Chemical Bond* (World Scientific, Singapore, 1994).

[2] *Femtosecond Chemistry* edited by J. Manz and L. Wöste (VCH Publishers, Inc., New York, 1995).

[4] J. J. Gerdy, M. Dantus, R. M. Bowman, and A. H. Zewail, Chem. Phys. Lett. **171**, 1 (1990).

[5] E. D. Potter, J. L. Herek, S. Pedersen, Q. Liu, and A. H. Zewail, Nature **355**, 68 (1992).

[6] J. L. Herek, A. Materny, and A. H. Zewail, Chem. Phys. Lett. **228**, 15 (1994).

[7] A. H. Zewail, J. Phys. Chem., Centennial Edition, to be published Aug. 1996.

[8] S. Pedersen, J. L. Herek, and A. H. Zewail, Science **266**, 1359 (1994).

[9] J. L. Herek, S. Pedersen, L. Bañares, and A. H. Zewail, J. Chem. Phys **97**, 9046 (1992).

[10] S. Pedersen, Ph.D. thesis, California Institute of Technology, 1996.

[11] T. Baumert, J. L. Herek, and A. H. Zewail, J. Chem. Phys. **99**, 4430 (1993).

[12] A. Mokhtari, P. Cong, J. L. Herek, and A. H. Zewail, Nature **348**, 225 (1990).

[13] A. Materny, J. L. Herek, P. Cong, and A. H. Zewail, J. Phys. Chem., **98**, 3352 (1994).

[14] P. Cong, G. Roberts, J. L. Herek, A. Mokhtari, and A. H. Zewail, J. Phys. Chem. **100**, 7832 (1996).

[15] B. Horn, J. L. Herek, and A. H. Zewail, to be published.

1. Principles of Femtosecond Spectroscopy

The key feature of femtosecond spectroscopy is its ability to resolve nuclear motion on the time scale at which it occurs. Indeed, an "ultimate time scale" has been reached in ultrafast spectroscopy,[1] where bonding changes in chemical transformation are observed directly. The observations can be related to classical trajectories or quantum wave-packet descriptions for chemical reactions, as well as to statistical concepts such as intramolecular vibrational energy redistribution (IVR) and reaction rates.

This chapter summarizes some of the fundamental principles of femtosecond spectroscopy. The time scales for fundamental dynamics are discussed, as well as the general concept of pump-probe experiments. The relation to time-integrated techniques in the frequency domain is presented, including a brief discussion of the consequences of resolution (temporal and spectral) in femtosecond techniques.

Time Scales in Chemical Dynamics

The fundamental dynamics of chemical transformation center on bond breakage and formation processes. The time required to break a bond can be estimated by classical concepts. Since atoms and molecules have typical velocities on the order of 1 km/s, the elementary dynamics of a reaction occur on the time scale of femtoseconds, assuming a resolution of angstroms (1 km/s = 0.01 Å/fs). This classical estimate of femtoseconds for the time scale of nuclear motion is evident in trajectory calculations[3] as well as statistical transition-state theory of reaction rates,[4] both developed in the 1930's. Indeed, the theoretical foundation for femtochemistry has long been set!

Figure 1.1 shows estimated time scales for fundamental dynamics in chemistry. Each of these processes has been resolved by techniques of ultrafast spectroscopy (for examples, see Ref. 1 and references therein).
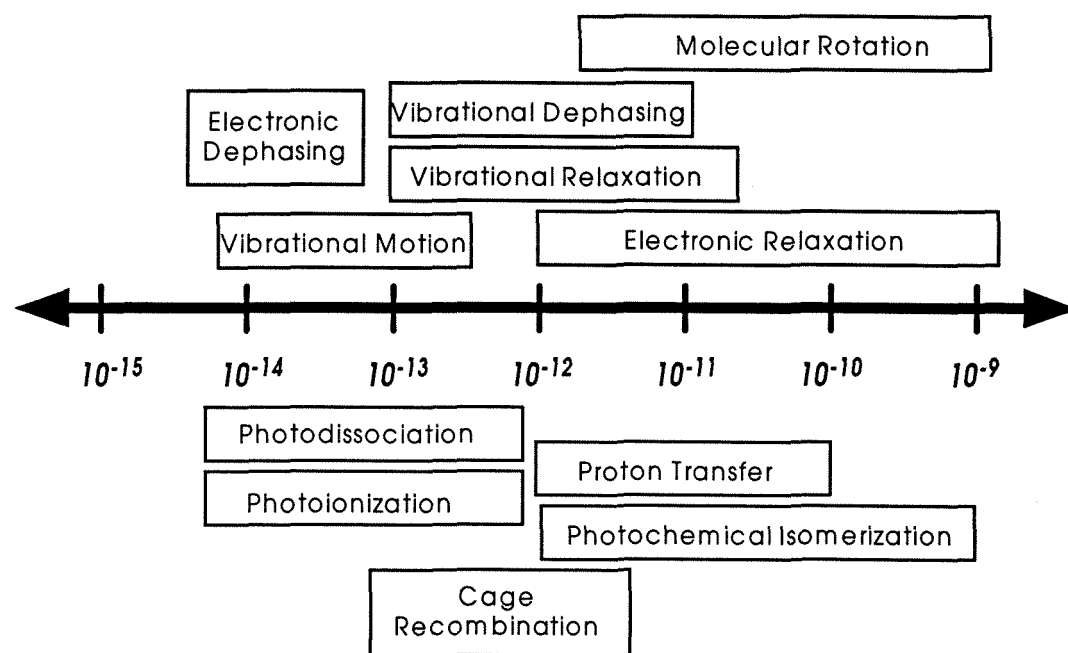

Figure 1.1 Approximate time scales for fundamental chemical dynamics. Adapted from Ref. 2.

General Concept

Figure 1.2 shows cuts of model potential energy surfaces (PESs) for introducing the concept of femtosecond probing of reaction dynamics. Such PESs are typical of a real molecular system, in which excitation to the upper electronic state (V_1) leads to dissociation.
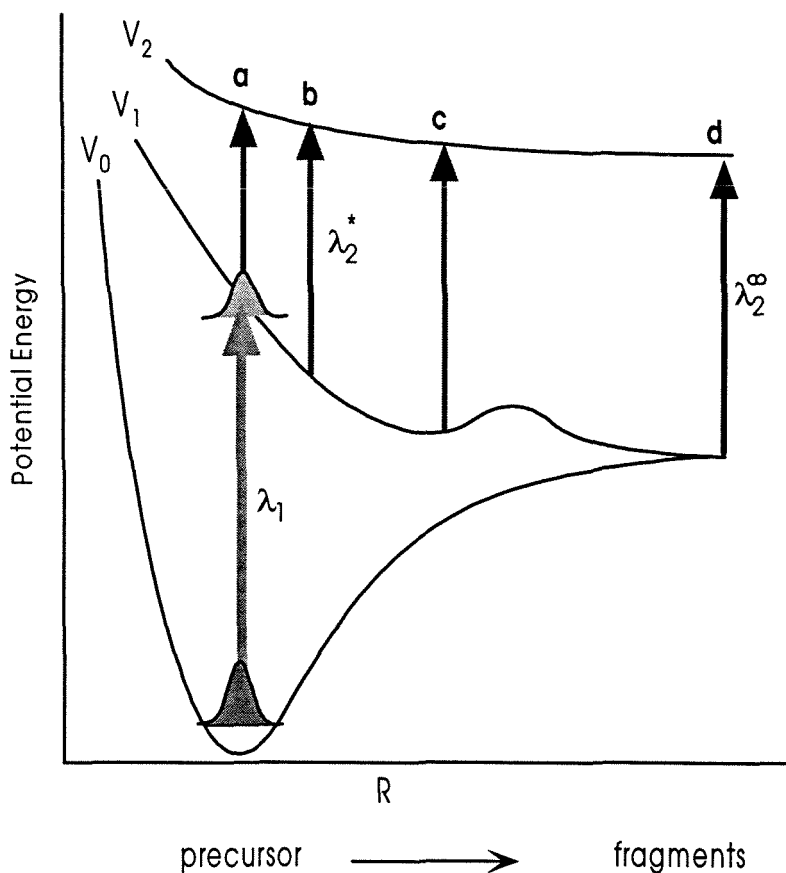

Figure 1.2 Model potential energy curves for a bound molecule (V_0) and two of its excited electronic states (V_1 and V_2). The femtosecond pump pulse takes the molecule from V_0 to V_1, where repulsion between fragments leads to bond breaking. Probing the dynamics of the dissociation process at four discrete time delays (a – d) is described in the text.

A small barrier to dissociation indicates that the reaction proceeds by way of a short-lived intermediate. The only relevant configurational parameter for describing the reaction dynamics is assumed to be R, the internuclear separation of the fragments in the center-of-mass frame. Initially, the molecule is in its lowest electronic state, V_0. This surface has a well-defined minimum that occurs at an equilibrium separation R_e.

Monitoring the real-time evolution of a chemical reaction is achieved by a pump-probe experiment. A femtosecond optical pulse with wavelength $\lambda_1 \equiv \lambda_{pump}$ initiates the reaction. For a unimolecular dissociation, this entails an electronic excitation of the precursor molecule from the V_0 ground state to a dissociate state (here V_1). The initial internuclear separation R_0 is defined as the distance between fragments at $t = 0$. As a rule, all times are taken to be relative to the temporal midpoint of this pump pulse (the "zero-of-time," t_0).

After the system evolves for some time delay, $t = t_d$, it is irradiated by a second femtosecond (probe) pulse, with wavelength $\lambda_2 \equiv \lambda_{probe}$. The probe pulse is absorbed only if the configuration of the system at time t_d is appropriate for a vertical transition from V_1 to a higher-excited PES, V_2. Alternatively, absorption of the probe pulse may reach the ionization potential of the species of interest, generating a positive ion and an electron. Those configurations which allow for absorption of the probe photon are called the "optically-coupled region" of the PES. This region depends on the energy difference between the PESs as a function of internuclear separation, $V_2(R) - V_1(R)$, and on the energy and spectral width of the probe pulse.

The observed signal is a measure of the absorption of the probe pulse as a function of the time delay t_d between λ_1 and λ_2. While, in principle, the change in transmission of the probe pulse could be monitored, such detection would not be background free, nor very sensitive as the change in intensity would be slight in a

gas-phase experiment. Instead, detection of laser-induced fluorescence (LIF) or multiphoton ionization (MPI) generated by the probe yields far better sensitivity. Typically, the signal is measured when λ_2 is tuned to an absorption resonance of the free fragment, λ_2^∞ (where ∞ denotes $R \to \infty$), and at a number of wavelengths corresponding to resonances of the transition-state or intermediate species, λ_2^* (* denotes wavelengths corresponding to the region of R between R_0 and R_*). A "surface" of measurements can be constructed and related to the potential energy surface and dynamics of the reaction.

From Transients to Dynamics

The shape of the femtosecond transients recorded for parent and fragment species reflects the dynamics of the evolving system. Preparation of the excited state involves transfer of a fraction of the ground state population to the reactive surface via a resonant transition. The initial wave packet is generated by the coherent superposition of the energy levels spanned by the pump laser, taking on the characteristic shape (*i.e.* Gaussian, sech^2; see Chapter 2) of the pump pulse. The evolution of this wave packet is henceforth determined by the potential energy surface on which it is prepared, as well as the allowed couplings and crossings with neighboring surfaces.

As an example, consider the model potential energy surfaces drawn in Fig. 1.2. The wave packet prepared on the repulsive branch of the V_1 excited state follows a downhill slope to products, with a small mogul interrupting the descent. By probing the system at a few discrete points along the way, we ascertain the influence of the potential and perhaps better determine the subtleties of its shape.

In Fig. 1.3, the expected femtosecond transients are presented for signal detection at four sites upon the excited electronic state surface in Fig. 1.2. The first

transient (a) corresponds to detection of the excited precursor, formed upon a steep

repulsive branch. The coherent nature of the system is reflected in the transient;

the rapid departure of the wave packet from its initial position at R_0 results in a

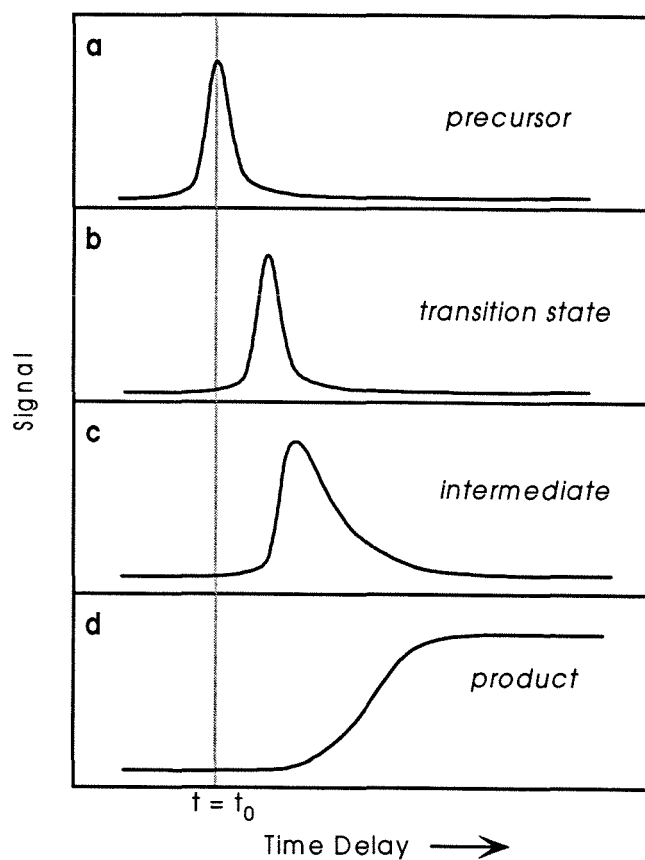narrow signal whose fwhm is given by the cross correlation of the pump and probe

Figure 1.3 Femtosecond transients (schematic) for probing different species of the dissociating system (see text).

pulses. At point (b), still on the repulsive branch of the potential energy curve but

now in the transition-state region, the wave packet passes through the detection

window, producing a transient signal that again reflects the cross-correlation, but

now shifted from time zero. The potential felt by the evolving wave packet changes significantly at (c), owing to the presence of a small exit-channel barrier. The wave packet may dwell here, such that the corresponding transient reflects a more statistical dynamical behavior. By point (d), the system is essentially fragmented; the associated transient shows a build-up of signal that reaches a constant level at long times.

Uncertainty Principle

A key feature of femtosecond spectroscopy is the initial localization of atoms by coherent preparation of the nuclear configuration. This is a direct consequence of the ultrashort time duration of the pump pulse and the accurate establishment of the zero-of-time. The ultrashort time duration of the pump pulse, however, is associated with broad energy distribution, given the relation between time and energy characterized by the Heisenberg uncertainty principle. Questions of resolution, both temporal and spectral, are hence natural; specifically, how can a broad-energy pulse probe a sharp resonance?

Indeed, such an energy span is necessary to allow for the coherent superposition of energy eigenstates which creates the initial wave packet. In studies of bound systems (such as I_2), the wave packet oscillates within the potential well, moving in and out of resonance with the probe laser window located at a particular coordinate along the trajectory. The measured intensity of the probe signal images the motion and provides the eigenstate frequencies of which the wave packet is composed. Spectroscopic information is retained in femtosecond spectroscopy, in spite of the fact that the energy width of the pulses is much broader than the vibrational energy spacings of the resonance. All spectral information is contained within the transient signals, and may be extracted via Fourier

transformation. Direct inversion to the potential energy surface governing the motion has been shown to be in excellent agreement with results from high-resolution techniques (see Ref. 5 for examples from Caltech).

Relation to Frequency Domain

Prior to the advent of femtosecond lasers, techniques to glean information of the transition region were applied to many chemical systems; today they remain complementary methods for understanding the complete picture of reaction dynamics. Time-integrated methods such as absorption, emission, scattering, and ion spectroscopy can be directed at the transition-state region to obtain model potentials characterizing the reaction coordinates. High detection sensitivity is required, however, in order to compensate for the approximately five orders of magnitude difference between the lifetimes of the transition states and the time scales of the experiments.

References

[1] *Femtosecond Chemistry*, edited by J. Manz and L. Wöste (VCH Publishers, Inc., New York, 1995) Vol. 1 & 2.

[2] G. R. Fleming, *Chemical Applications of Ultrafast Spectroscopy* (Oxford University Press, New York, 1986).

[3] J. O. Hirschfelder, H. Eyring, and B. Topley, J. Chem. Phys. **4,** 170 (1936); M. Karplus, R. N. Porter, and R. D. Sharma, J. Chem. Phys. **43,** 3258 (1965).

[4] H. Eyring, J. Chem. Phys. **3,** 107 (1935); M. G. Evans and M. Polanyi, Trans. Faraday Soc. **31,** 875 (1935); *ibid.* **33,** 448 (1937).

[5] A. H. Zewail, *Femtochemistry: Ultrafast Dynamics of the Chemical Bond* (World Scientific, Singapore, 1994) Vol. 1 & 2.

2. Experimental Methodology

The experiments described in Chapters 3 – 6 all involve the application of femtosecond pump-probe spectroscopy to gaseous systems prepared in a static cell or molecular beam. The salient features of the laser system, the molecular beam, the pump-probe technique, and the data acquisition procedures are discussed briefly here. A thorough examination of these topics is found in Ref. 1. Specific details relevant to the individual experiments, such as sample preparation and data analysis, are presented in later chapters.

The Femtosecond Laser System

In 1986, the Femtosecond Laser Facility was built at Caltech with the intent of applying ultrashort pulses to studies of chemical dynamics. Adapting the newly-developed design by C.V. Shank and co-workers at Bell Laboratories,[2] members of the Zewail group built[3] the colliding-pulse mode-locked (CPM) ring dye laser, capable of producing 50 fs laser pulses with a wide wavelength tuning range. This achievement marked the first application of femtosecond lasers to chemical reaction dynamics, and the last step in reaching the time domain characteristic of nuclear motion (see Chapter 1). At the time of this writing, the Caltech Femtosecond Laser Facility has become known as *Femtoland*, with five laboratories housing various laser systems, including both CPM and state-of-the-art Ti:Sapphire femtosecond lasers.
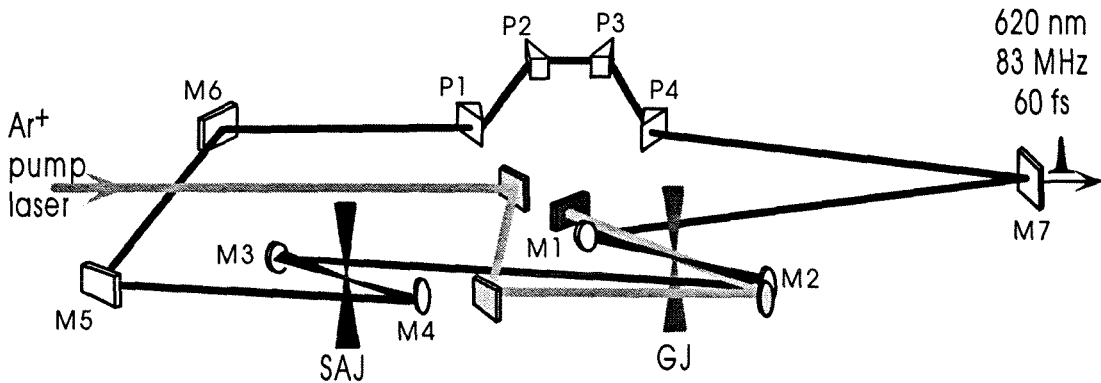
CPM

Figure 2.1 Schematic drawing of CPM laser. The lasing cavity consists of seven mirrors, labeled M1-7. The gain jet is GJ and saturable absorber jet is SAJ. The four prisms are labeled P1-4. Mirror M7 is 2 % transmissive and serves as the output coupler. The output pulses have typical widths (fwhm) of 60 fs with a central wavelength of 620 nm. The repetition rate is 83 MHz, determined by the cavity length.

The CPM dye laser is shown schematically in Fig. 2.1. A continuous-wave Ar^+ laser (Coherent, Innova 100) serves to pump the gain dye (R590) whose isotropic fluorescence is captured in part by two curved mirrors, M1 and M2. This fluorescence is directed both clockwise and counterclockwise around the ring cavity formed by the seven mirrors and four prisms. The function of the prisms extends beyond waveguiding; the geometric arrangement is designed to eliminate positive dispersion introduced by the other optical elements (see below). The saturable absorber (DODCI) prevents completion of the cycle until intensities are sufficiently high such that the dye is bleached. An intensity spike in the gain fluorescence can penetrate the saturable absorber and the resulting pulse will be further amplified upon passing through the gain jet again. The shortest pulses are obtained when two counterpropagating light pulses collide simultaneously at the saturable absorber, as

the leading edges are absorbed by the dye prior to saturation. The emerging pulses

are mode-locked, *i.e.* the relative phases of all resonant modes in the cavity are

equal to zero given the ultrafast response of the saturable absorber "shutter." M7

serves as the output coupler, allowing passage of 2% of the internal radiation. The

pulses at this point have a repetition rate of 83 MHz (defined by the cavity length),

and are typically 60 fs in duration with a central wavelength of 620 nm and pulse
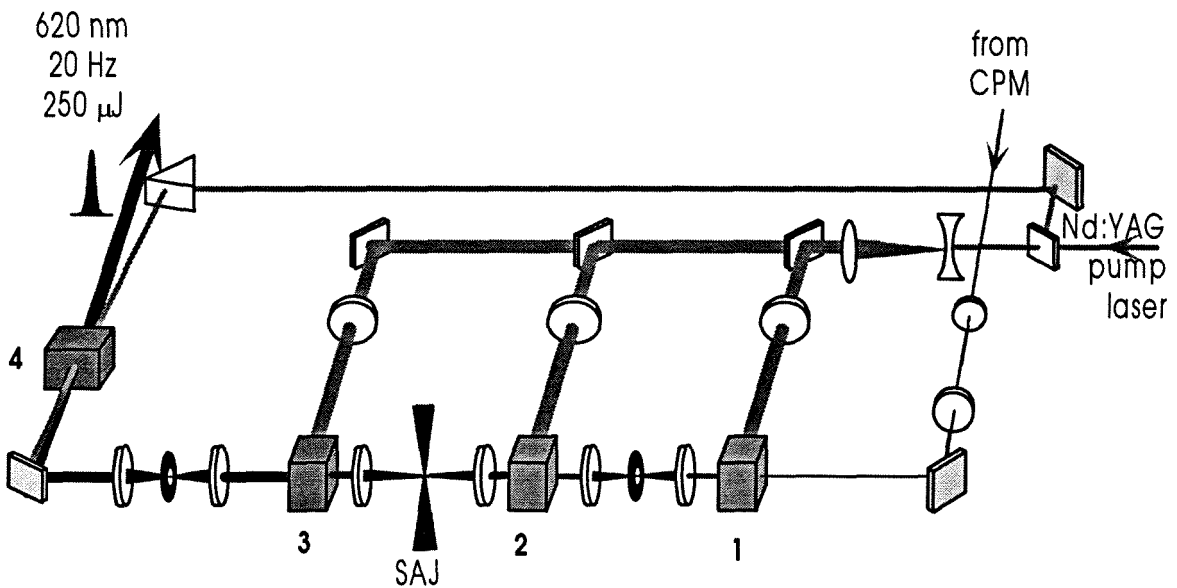
energies on the order of 250 pJ.

Figure 2.2 Schematic drawing of the pulsed dye amplifier. The CPM light is directed though four dye cells, each pumped by the 532 nm Nd:YAG laser. A saturable absorber jet (SAJ) placed after the 2nd stage reduces amplified spontaneous emission, as do the pinhole apertures located after the 1st and 3rd stages.

The pulsed dye amplifier (PDA) is shown schematically in Fig. 2.2. A Nd:YAG laser (Spectra Physics, DCR 3-G) operating at 20 Hz serves as the pump source; the 532 nm light is divided and focused into four dye cells. The Nd:YAG is triggered by the CPM, with a delay generated by a synchronizer module (Spectra Physics SM1) to ensure good temporal overlap of the YAG pulses with the CPM pulses. A saturable absor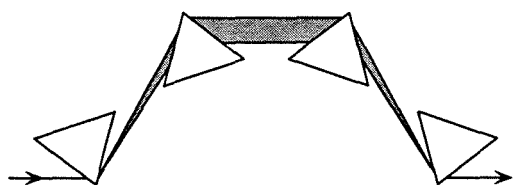ber (malachite green) is placed after the second stage to reduce background signal; while the amplified pulses have sufficient intensity to penetrate, other sources such as amplified spontaneous emission do not. The CPM pulses are amplified by a factor of $\sim 10^6$ in this four-stage amplifier. In addition, however, they are temporally broadened by a factor of ~ 10 due to group velocity dispersion through the dye cells.

Figure 2.3 Sequence of prism pairs for compensation of positive group velocity dispersion.

To correct for dispersion effects, the pulses are guided through a sequence of four equilateral prisms (Fig. 2.3). The geometric arrangement of the prisms is such that the reddest parts of the pulses (leading edge) will travel a longer pathlength than the blue. Carefully aligned, this setup will recompress the pulses back to their original pulse width, $\sim$ 60 fs.

Pulse Characterization

Both the temporal and energetic profiles of the laser pulses were routinely monitored throughout the course of the experiments. Typically, such characterizations were limited to PDA pulses, though analogous measurements may be made upon the CPM pulses prior to amplification.

The spectral profile of the femtosecond pulses was obtained directly by dispersing the light into a monochromator (Spex, 0.3 m). With the narrowest slit width possible, the resolution was 0.1 nm. A typical PDA pulse spectrum is shown in Fig. 2.4.
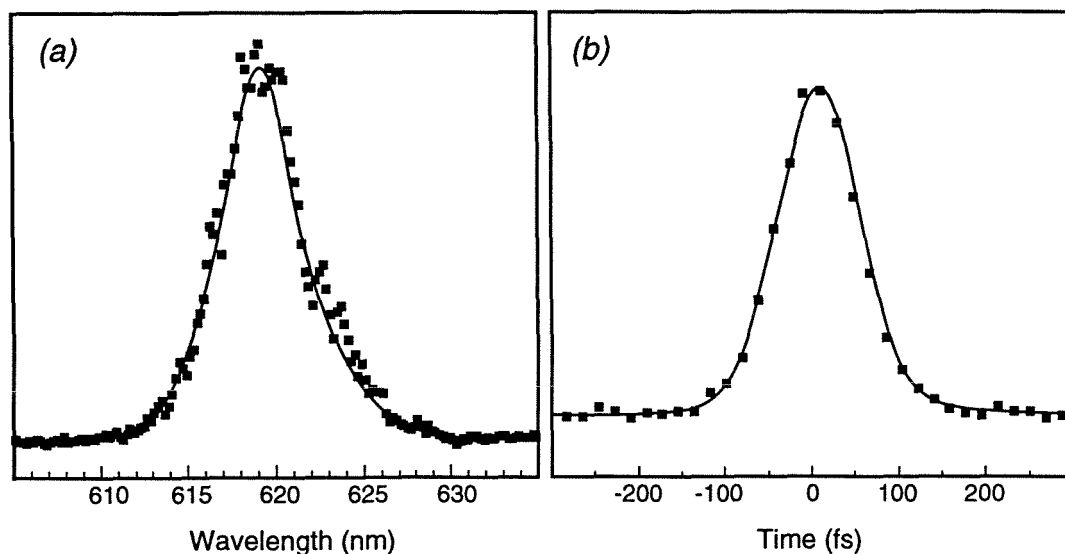

Figure 2.4 (a) Pulse spectrum and (b) intensity autocorrelation of (recompressed) femtosecond pulses from PDA.

The temporal profile of the femtosecond pulses was obtained indirectly, via an optical intensity autocorrelation fitted to an assumed pulse shape. Direct methods for characterization of ultrafast pulses are limited by detector response times to a resolution of ~1 ps.[4] In an intensity autocorrelation, the pulse is split into two pulses by a 50/50 beam-splitter, see Fig. 2.5. One pulse follows a fixed-length path while the other traverses a
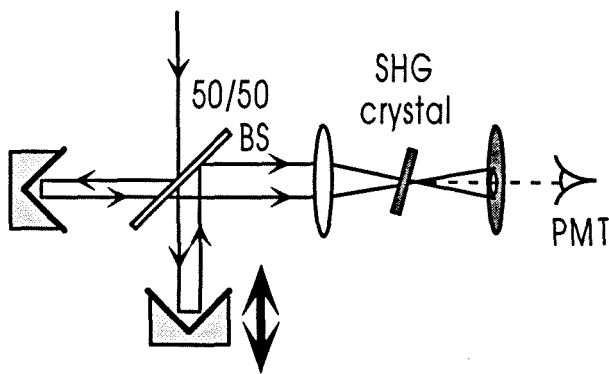

Figure 2.5 Background-free autocorrelation setup.

variable-length delay line. The two pulses are focused to intersect in a nonlinear optical crystal which doubles the optical frequency. By carefully choosing the phase-matching condition and suppressing the frequency-doubled light from each independent pulse, the signal generated upon the overlap of the two pulses can be isolated and detected. The measured optical correlation (see Fig. 2.4b) must be fit to an assumed function to determine the real pulse profile.[5] Generally, Gaussian or sech^2 functions are used to describe the pulse shape.

Pump–Probe Techniques

Pump–probe techniques are ideally suited to measurements of ultrafast dynamical processes. For studies of unimolecular reaction dynamics, the femtosecond pump pulse prepares the parent molecule on an excited electronic surface. A probe pulse with a variable time delay monitors the time evolution of the population density of parent or fragment species (see Chapter 1 for discussion of the general concept of femtosecond pump-probe spectroscopy). The time resolution is only limited by the pulse widths of the two pulses and not by the time constants of the detector.
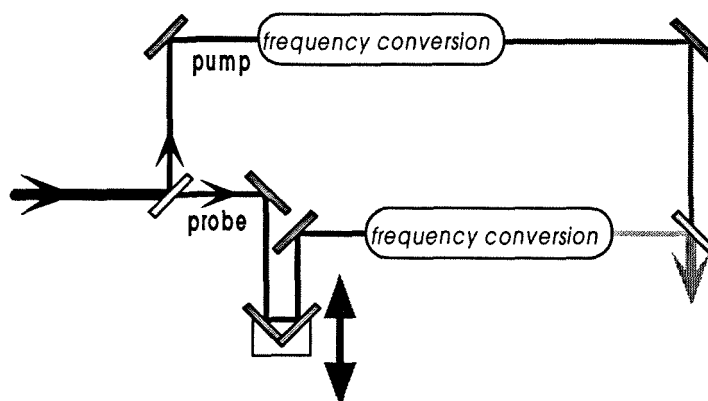

Figure 2.6 Schematic drawing showing the optical paths for generation of the pump and probe beams.

The femtosecond pulses of the PDA are divided into two arms, forming the pump and probe beams as shown schematically in Fig. 2.6. Each beam must undergo necessary frequency conversion processes (described below) to generate the appropriate photon energies for pumping or probing the species of interest. By varying the time delay between the pump and probe pulses and recording the signal at discrete steps, the evolution of the chemical reaction may be monitored in real time.

The Delay Line

The precision associated with controlling the pump-probe delay is a critical factor in determining the overall resolution of the experiment. Because light pulses travel at a speed of 0.3 μm/fs, sub-micron control of the delay line is necessary. We employ an optically-encoded micropositioner (MicroKinetics) with a step size of approximately 60 nm (~0.4 fs/step). The controller is interfaced with the computer, allowing automated positioning and scanning. The maximum travel length of the actuator is 25 mm, corresponding to a maximum transient length of ~150 ps.

Frequency Conversion

The pump and probe beams must be tuned to wavelengths appropriate to the specific molecular system under investigation. The fundamental lasing wavelength of the CPM/PDA is approximately 620 nm and tunability based on the parameters within the CPM is limited. By decreasing the DODCI concentration, for example, the central lasing wavelength can be blue-shifted as far as 610 nm. To expand the tunability throughout the UV and visible regions of the electromagnetic spectrum, other techniques of frequency conversion, such as doubling, mixing, and continuum generation, are employed.
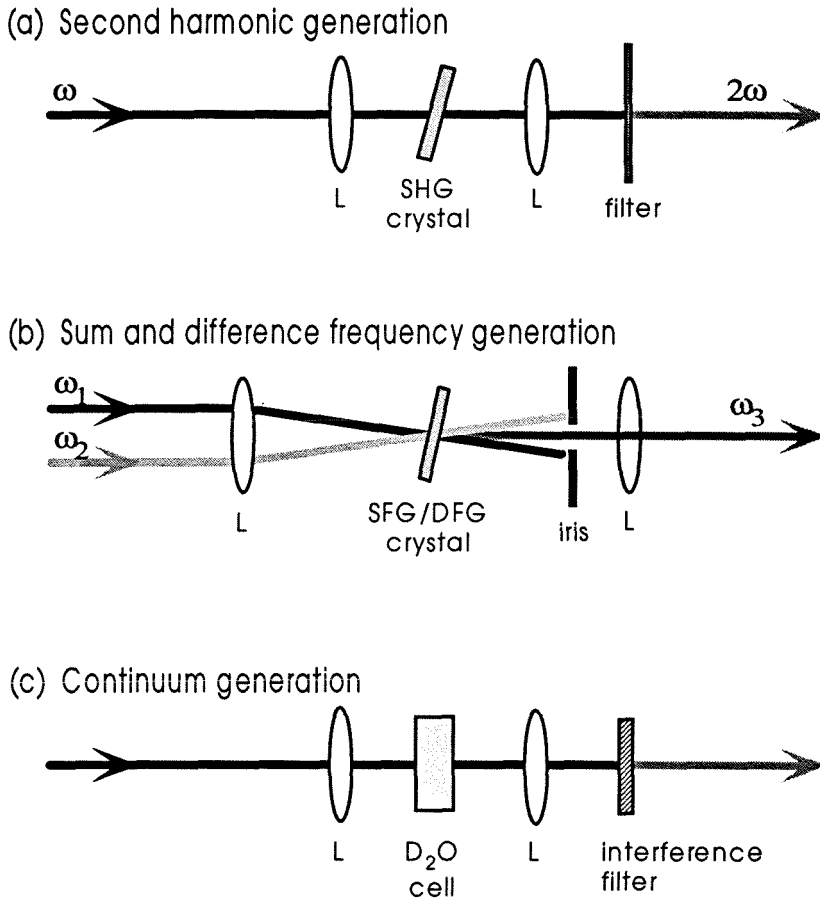
(a) Second harmonic generation

(b) Sum and difference frequency generation

(c) Continuum generation

Figure 2.7 Optical arrangements used for frequency conversion: (a) second harmonic generation, (b) sum and difference frequency generation, and (c) continuum generation.

Frequency doubling is achieved by second harmonic generation in a thin nonlinear crystal.[6] In essence, two identical photons of frequency ω combine to generate a single photon of twice the energy, 2ω. For example, the 620 nm light is focused onto a 0.1 – 0.2 mm thick KDP or KD*P crystal, generating output light is at 310 nm (see Fig. 2.7a). The efficiency of this process is better than 15%, given the high peak intensities of the femtosecond pulses.

Frequency mixing, *i.e.* sum and difference frequency generation, is also possible. The interaction of two photons of different frequencies ω_1 and ω_2 in a

nonlinear crystal produces a third photon at the sum ($\omega_3 = \omega_1 + \omega_2$) or difference ($\omega_3 = \omega_1 - \omega_2$) frequency. This technique has successfully generated femtosecond pulses at 391 nm by summing the 620 nm pulses with residual Nd:YAG pulses at the fundamental lasing wavelength of 1064 nm, as well as 266 nm (= 620 nm + Nd:YAG second harmonic at 532 nm). The optical arrangement for these processes is shown in Fig. 2.7b.

Broader tunability is achieved by continuum generation. A white-light continuum is produced upon focusing the femtosecond pulses into a cell of D_2O. The physics behind this effect is discussed in Ref. 7. While the continuum extends from the UV to the IR regions of the electromagnetic spectrum, we have succeeded in using only the range from ~ 490 – 700 nm without amplification. Wavelength selection is achieved with interference filters which allow transmission of only a narrow bandpass. Typical interference filter bandwidths are 10, 5, and 2 nm. The resulting pulses are broadened by a factor of 1.5 – 2, given the dispersion introduced in the continuum setup, see Fig. 2.7c.

Amplification of pulses generated by the continuum is performed using residual light of the Nd:YAG laser to pump a dye cell. For wavelengths greater than ~550 nm, the Nd:YAG second harmonic at 532 nm is employed, where for shorter wavelengths, the third harmonic at 355 nm may be used. This arrangement amplifies the pulse energy by a factor of 100. The amplified pulses may then undergo frequency doubling as described above to produce desired wavelengths in the UV region.

The Molecular Beam

The molecular beam apparatus is shown schematically in Fig. 2.8. The assembly consists of two chambers, differentially pumped by 510 and 240 *l/s* turbomolecular vacuum pumps (Balzers). The source chamber houses the pulsed

valve which can be translated by a kinematic carriage. The valve was kept close to the skimmer for the ionization experiments reported here; it can also be moved back for LIF studies within the source chamber (see Fig. 2.8). The ionization chamber, separated from the source chamber by a skimmer (~1.5 mm diameter), is equipped with a TOF mass spectrometer. The repeller, extractor, and ground grids accelerate the ions toward the microchannel plate (MCP) detector (Galileo), located at the end of the TOF drift tube approximately 20 cm from the interaction region. Typical operating conditions were +3.0 and –2.0 keV on the repeller and extractor plates, respectively, and 1.7 to 2.0 keV on the MCP. Time-of-flight mass spectra are recorded by either a transient digitizer (LeCroy 8818A) or a 300 MHz digital oscilloscope (LeCroy 9361).
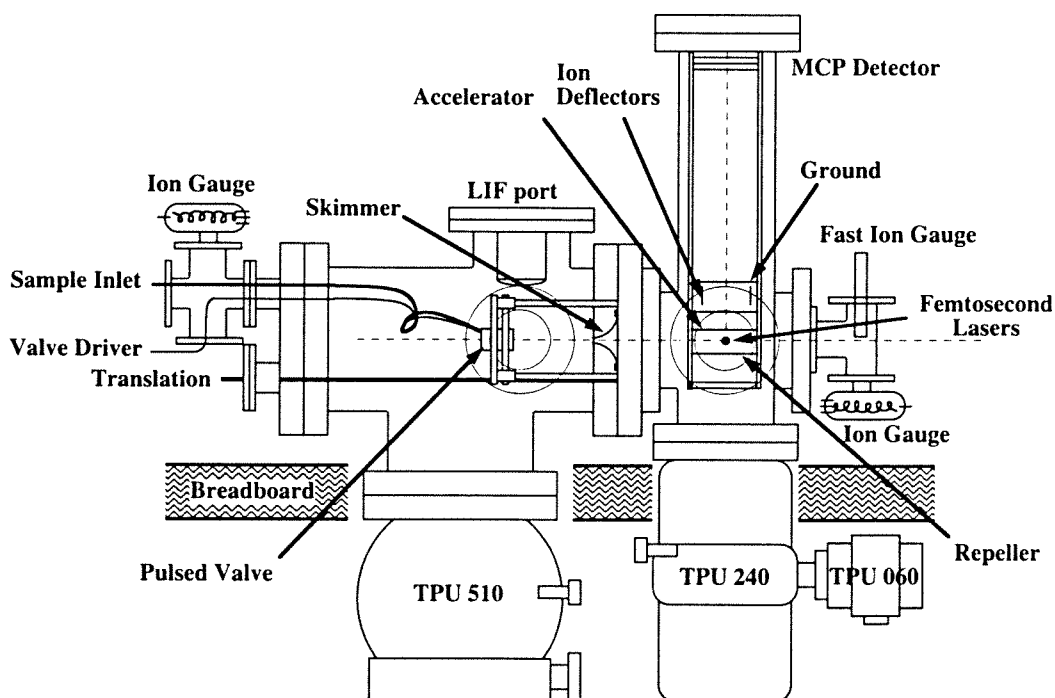

Figure 2.8 Schematic drawing of molecular beam apparatus (from Ref. 8).

The molecular beam was produced by a 20 Hz pulsed valve with a 0.3 mm diameter orifice. To ensure good overlap of the molecular beam with the femtosecond pump and probe pulses, the valve was synchronously triggered by the laser system. The samples are typically seeded in He with a backing pressure of ~20 psi. The ionization region, approximately 12 cm from the valve outlet, was maintained at pressures on the order of 10^{-6} torr.

Data Acquisition

The data acquisition scheme requires setting the time delay, collecting the signal (by PMT, MCP, etc.), averaging in a boxcar integrator, and sending the averaged value for a given time delay to the computer. The entire data acquisition procedure is performed by a Macintosh II computer, with software written by M. Rosker, L. Peng, and M. Dantus (see Ref. 1 for additional details and source code).

For typical femtosecond transients, the species of interest was selected by its mass according to the TOF using a gated boxcar integrator (Stanford Research 250). The ion signal was then monitored as a function of the time delay between the pump and probe pulses.

References

[1] M. Dantus, Ph. D. thesis, California Institute of Technology, 1991.

[2] R. L. Fork, B. I. Green, and C. V. Shank, Appl. Phys. Lett. **38,** 671 (1981).

[3] M. J. Rosker, M. Dantus, and A. H. Zewail, J. Chem. Phys. **89,** 6113 (1988).

[4] W. Demtroder, *Laser Spectroscopy; 2nd enlarged edition* (Springer-Verlag, Berlin, 1996).

[5] G. R. Fleming, *Chemical Applications of Ultrafast Spectroscopy* (Oxford University Press, New York, 1986).

[6] A. Yariv, *Quantum Electronics*, 3rd ed. (Wiley, New York, 1989).

[7] *The Supercontinuum Laser Source*, edited by R. R. Alfano (Springer-Verlag, New York, 1989).

[8] M. H. M. Janssen, M. Dantus, H. Guo, and A. H. Zewail, Chem. Phys. Lett. **214,** 281 (1993).

Application to Organic Chemistry

Femtosecond lasers have a special appeal to organic chemistry, where mechanistic puzzles have long been hidden under electron-pushing arrows. The fundamental mechanisms of many classic reactions in organic chemistry are based on inference and indirect implication, as the precise nature of the transition states and intermediates postulated to ensure a smooth progression from reactants to products has eluded researchers. Given the ultrafast time scale of most bond-breaking, bond-formation, and rearrangement processes, (See Ref. 1 and references therein) direct observation of these fundamental chemical events requires femtosecond resolution. As such, techniques of femtosecond pump-probe spectroscopy have been extended to organic molecular systems in the gas phase.

A number of classic reactions in organic chemistry have already been re-examined with femtosecond resolution, uncovering details of the dynamics and unraveling mechanistic mysteries. At Caltech, for example, such studies include *cis-trans* isomerization,[2] proton-[3] and hydrogen-transfer[4] processes, Norrish α-cleavage,[5] and Diels-Alder[6] and other cycloaddition reactions.[7] The implications of such studies are far reaching. Studies of hydrogen-transfer processes,[4b] for example, have direct consequences to the mechanism of mutation in DNA replication.

Chapters 3–5 present studies of two important classes of reactions in organic chemistry: cycloaddition reactions mediated by diradical intermediates, and intramolecular hydrogen-atom transfer. The motivation for these studies is presented below.

Diradicals

The study of organic diradicals has been at the forefront of research in physical organic chemistry in recent years. Interest in the field stems largely from the desire to better understand reaction mechanisms and electronic structure. To underscore the logical sequence of primary steps in a reaction mechanism, chemists often postulate feasible intermediates which ensure smooth transitions between stable species. Historically, such constructs were merely hypothetical as their (assumed) extreme reactivity and/or unstable nature precluded their observation. Diradicals are often invoked as intermediate species in many thermal[8] and photochemical[9] transformations. Direct evidence for their existence and a study of their reactivity can not only help chemists understand these important reactions, but also improve their predictive ability in reaction mechanisms.

Intuitively, a diradical intermediate may be formed simply by stretching a carbon-carbon bond in a carbocyclic ring to its breaking point.

Scheme 1 Diradical formation.
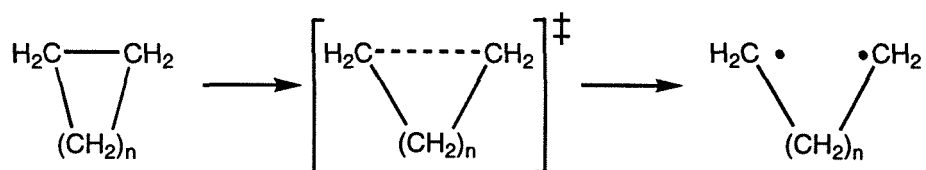
Such homolytic bond rupture, in which each of the two bound atoms retains one of the bonding electrons, is a building block of chemical transformation. It is the mainstay of organic dissociation reactions, far more prevalent than the heterolytic (ionic) process in which both bonding electrons end up on one atom.[10] When the dissociation site is part of a ring system, as in Scheme 1, the radical pair is

restrained from complete separation, allowing insight in the interaction between radical centers.
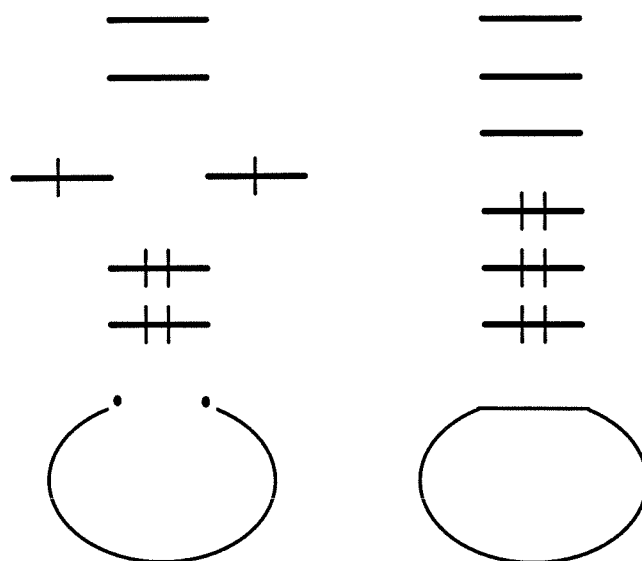

Figure 1 Simple molecular orbital representation of an organic diradical and its closed-shell carbocyclic species.

A diradical can be defined as an even-electron species with one fewer bond than allowed by the standard rules of valence.[11] As such, they are often referred to as "open-shell" structures. In terms of molecular orbitals, this translates to the presence of a pair of singly-occupied degenerate or nearly degenerate non-bonding orbitals; see Fig. 1. The two electrons can either be paired (spin quantum number S = 0; singlet) or parallel (S = 1; triplet).

Thermodynamically, diradicals lie quite close to transition states for reactions involving the formation or homolytic cleavage of C—C single bonds. Direct observations thus provide important information about the structure and properties of transition states. For example, it is still not clear whether diradicals, especially singlet diradicals, are best thought of as transition states or as true

intermediate species. Recent studies of triplet diradicals have shown these species to occupy local minima on potential energy surfaces, with barriers ascribed to the electron spin inversion which must precede product formation.[12,13] In general, however, theoretical calculations and experimental stereochemical studies have failed to provide any conclusive evidence for the presence of an energy barrier to the closure of a singlet diradical.

Key questions have focused on the structure and chemical behavior of such diradical species. What reactions may compete with the simple re-formation of the chemical bond? How do methods of generation affect diradical behavior? How significant are interactions between radical centers? What effects do alkyl substitution and/or isotope exchange have on the relative rates of reactions? How does the spin state affect the reaction dynamics? And, perhaps most central to our understanding of diradical behavior, what is the nature of the potential energy surface?

trimethylene
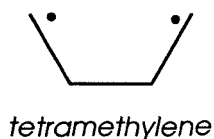
tetramethylene

Chapters 3 and 4 are devoted to femtosecond studies of the two smallest nonconjugated organic diradicals, trimethylene and tetrametylene.[7] Direct observation and characterization of these archetypal species via femtosecond spectroscopy has led to deeper understanding of their role as intermediates in cyclization and rearrangement reactions. The results are interpreted in terms of the corresponding reaction mechanisms, and comparisons are drawn with theoretical predictions for the diradical lifetimes and kinetic isotope effects.

Hydrogen-atom transfer

Many fundamental reactions in organic chemistry involve hydrogen atom (or proton) transfer processes. Intuitively, one might expect that the associated dynamics reflect localized motion of the light hydrogen within a "frozen" molecular frame. The general description of the reaction coordinate is of the type

$$O_a—H———O_b ,$$
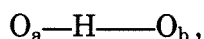
where the hydrogen is between two oxygen (or other electronegative) atoms. As the hydrogen is transferred from O_a to O_b, the O_a–H bond is broken and a new bond between H and O_b is formed. In reality, however, the molecular motion may not be so simple. While the transfer process may be localized, it may also involve additional nuclear motions with a simultaneous redistribution of electrons in many bonds.

With femtosecond time resolution, the dynamics of this fundamental process may be observed directly. Chapter 5 is devoted to studies of intramolecular hydrogen atom transfer studies in a prototype system, methyl salicylate.[4a] The goal is to resolve the elementary reaction dynamics and to examine the associated mechanism of the hydrogen atom transfer.
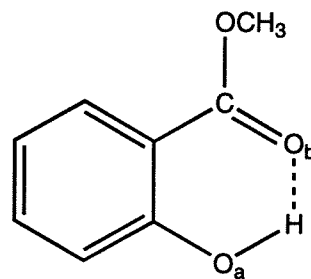
methyl salicylate

References

1. A. H. Zewail, *Femtochemistry: Ultrafast Dynamics of the Chemical Bond* (World Scientific, Singapore, 1994) Vols. 1 & 2.

2. L. Bañares, A. A. Heikal, and A. H. Zewail, J. Phys. Chem. **96,** 4127 (1992); S. Pedersen,.... and A. H. Zewail, to be published.

3. S. K. Kim, J. K. Wang, and A. H. Zewail, Chem. Phys. Lett. **228,** 369 (1994).

4. (a) J. L. Herek, S. Pedersen, L. Bañares, and A. H. Zewail, J. Chem. Phys **97,** 9046 (1992); (b) A. Douhal, S. K. Kim, and A. H. Zewail, Nature **378,** 260 (1995).

5. S. K. Kim and A. H. Zewail, Chem. Phys. Lett. **250,** 279 (1996).

6. B. Horn, J. L. Herek, and A. H. Zewail, to be published.

7. S. Pedersen, J. L. Herek, and A. H. Zewail, Science **266,** 1359 (1994).

8. J. J. Gajewski, *Hydrocarbon Thermal Isomerizations* (Academic Press, New York, 1981).

9. P. J. Wagner, in *Rearrangements in Ground and Excited States*, Vol. 1, edited by P. d. Mayo (Academic Press, New York, 1980).

10. N. J. Turro, *Modern Molecular Photochemistry* (University Science Books, Mill Valley, 1991).

11. *Diradicals*, edited by W. T. Borden (Wiley, New York, 1982).

12. R. Jain, Ph.D. thesis, California Institute of Technology, 1987.

13. C. Doubleday, N. J. Turro, and J. F. Wang, Acc. Chem. Research **22,** 199 (1989).

3. Trimethylene[*]

The trimethylene diradical epitomizes the challenge presented to experimental and theoretical chemists to understand the behavior of singlet diradicals as intermediates in chemical reactions. It is the smallest nonconjugated diradical, with radical centers insulated by only one methylene unit. As such, trimethylene may exhibit unique properties stemming from interaction of the radical centers.[1]

In this chapter, the nature of 1,3-diradicals in organic reactions is explored by femtosecond spectroscopy. The experimental methodology affords isolation and direct observation of the elusive intermediate species, given femtosecond resolution coupled with mass spectrometric detection. The results are interpreted in terms of the reaction mechanism, and comparisons are made with theoretical predictions of reaction rates and kinetic isotope effects.

---

[*] Preliminary report given in S. Pedersen, J. L. Herek, and A. H. Zewail, *Science*, **266**, 1359 (1994).

I. Background

The existence of trimethylene was first postulated more than 60 years ago in studies of the thermal decomposition of cyclopropane. Chambers and Kistiakowsky found that the reaction was unimolecular and that propylene was its sole product.[2] Assuming a single homolytic bond rupture occurred within the carbocyclic ring, they suggested that the trimethylene diradical might be an intermediate.

Scheme 3.1

cylopropane   trimethylene   propylene

Support for this diradical hypothesis came in 1958, when Rabinovich, Schlag, and Wiberg examined the thermal interconversion of *cis* and *trans* isomers of 1,2-d_2-cyclopropane.[3]

Scheme 3.2

trans   cis
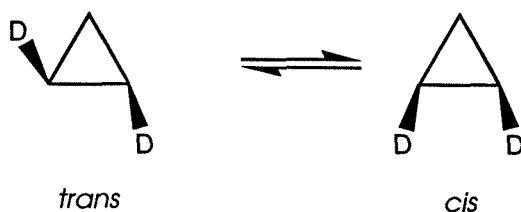
The *trans* isomer was found to rearrange to the *cis* species in competition with formation of d_2-propylene, demonstrating the existence of a reaction pathway involving rotation of at least one C—C bond. This observation, along with copious

other examples of stereomutation in substituted cyclopropanes,[4-20] has been regarded as "permissive evidence" for 1,3-diradical intermediates.[21,22]

No matter how permissive the evidence, however, the existence of the trimethylene diradical as an intermediate species is implied *indirectly* by such experiments. Further experimental attempts to characterize the 1,3-diradical have employed substituted cyclopropanes, pyrazolines (cyclic five-membered 1,2-diazenes), spiropentanes, and other precursors to generate trimethylene (for review, see Ref. 22), of which kinetic studies could be conducted. However, commonalities in the behavior of the 1,3-diradicals so generated are few; the nature of the trimethylene intermediate is strongly dependent on its mode of production. This behavior is likely a consequence of the interaction of radical centers in trimethylene and is not generally true for diradical intermediates. Tetramethylene, for example, with a larger separation of radical centers, has been shown to be a "common intermediate" whose behavior is independent of its mode of generation (see Ref. 23 and Chapter 4).
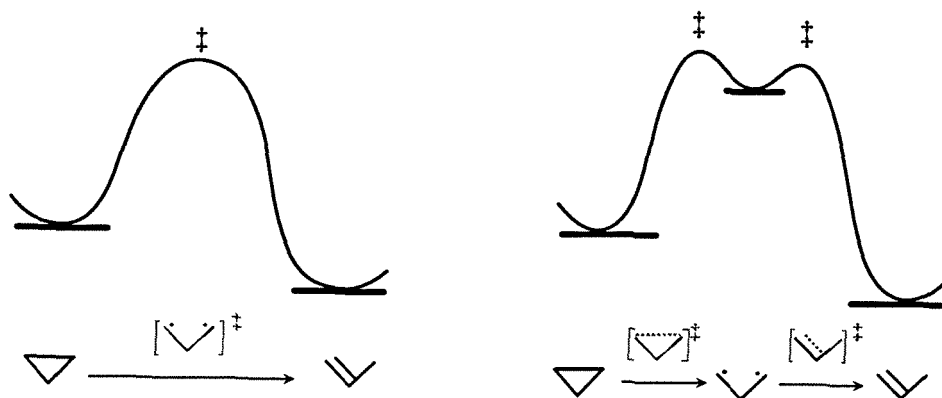

Figure 3.1   Schematic potential energy curves reflecting possible reaction coordinates for cyclopropane-propylene isomerization involving a trimethylene diradical. In (a), the diradical is described as a "true" intermediate, residing in a shallow well, while in (b), the diradical represents a transition state along the reaction coordinate.

Direct studies of trimethylene and related 1,3-diradicals are hence imperative in determining the nature of these species, as well as in understanding the fundamental concept of diradicals as intermediates in organic reactions, see Fig. 3.1. With femtosecond resolution and mass selection, the evolution of the elusive intermediate may be tracked in real time. In the experiments presented here, trimethylene is generated by a cyclobutanone precursor which undergoes a controlled decarbonylation process to prepare trimethylene in the saddle region of the cyclopropane–propylene surface. The subsequent dynamics of the trimethylene decay to cyclopropane and/or propylene are studied via lifetime measurements and substitution experiments. To avoid collisional deactivation and other perturbations, the reaction is carried out in a skimmed molecular beam.

II. Experimental

To observe the formation and evolution of the diradical species, we employed the combined techniques of femtosecond pump/probe spectroscopy and TOF mass spectrometry. The general methodology is described in Chapter 2, while specific features relevant to this experiment are detailed below.

A. Precursors

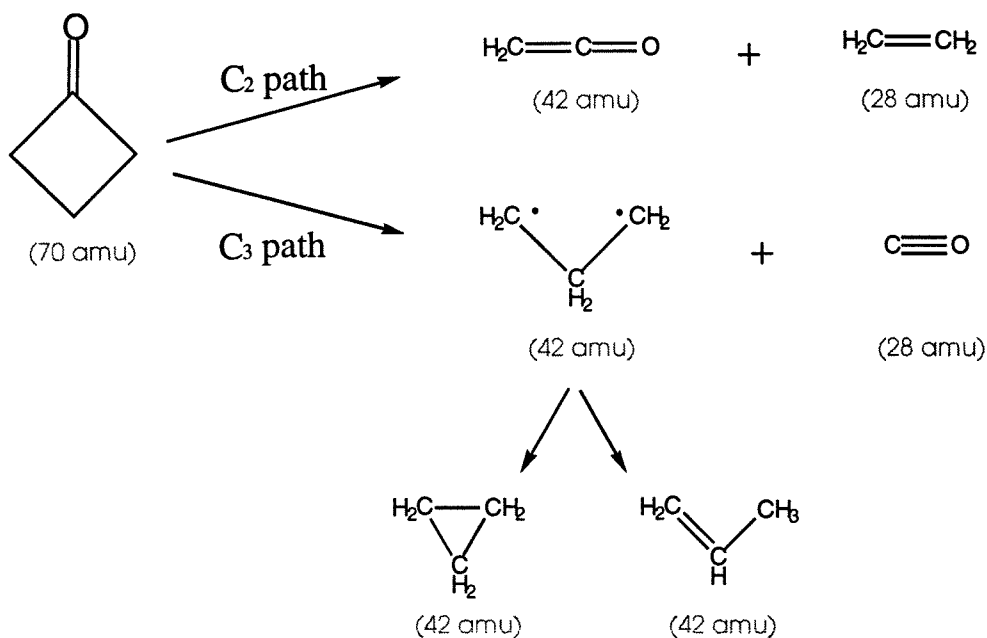*(i)*   *(ii)*   *(iii)*   *(iv)*
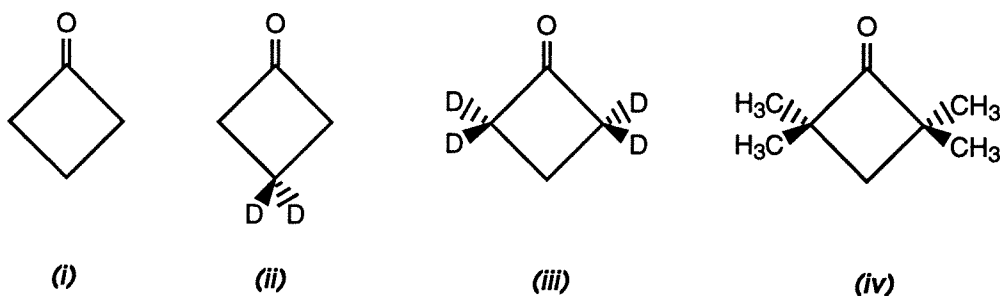
The diradicals were obtained by decarbonlyation of cyclic ketone precursors, *i.e.* cyclobutanone and its derivatives. Cyclobutanone **(i)** was purchased directly from Aldrich (99%) and used without further purification. The deuterium-labeled cyclobutanone precursors, namely 3,3-d_2-cyclobutanone **(ii)** and 2,2,4,4-d_4-cyclobutanone **(iii)**, were provided by Prof. J. Baldwin (Syracuse University) and Dr. K. Anderson (Caltech), respectively. Mass spectroscopy and NMR analyses indicated purities in excess of 95%. The methyl-substituted cyclobutanone, 2,2,4,4-tetramethylcyclobutanone **(iv)**, was also synthesized by Anderson, with a purity of approx. 90%.

B.   *Diradical Preparation*

The molecular beam was prepared by flowing He (*g*) over the liquid sample maintained at room temperature. The resulting mixture of the cyclobutanone vapor and He carrier gas (backing pressure ~20 psi) was directed to a pulsed nozzle (orifice diameter = 0.3 mm), triggered by the Nd:YAG laser at 20 Hz. The background pressure in the TOF chamber was maintained at 1×10^{-6} Torr when the nozzle was open.

The cyclobutanone precursors are known to dissociate by two possible pathways,[24] labeled the C_2 and C_3 channels according to the nature of the final products. The C_2 channel produces ethylene (C_2H_4) and ketene (CH_2CO), while the C_3 channel produces CO and vibrationally-excited cyclopropane (c-C_3H_6*) and/or propylene. The C_3 channel is likely to be mediated by a trimethylene diradical, as depicted in Scheme 3. The expected C_2/C_3 branching ratio at these energies (λ_{pump} = 2×310 nm) is estimated to be approximately 0.5.[25]

Scheme 3.3

$$H_2C\!=\!C\!=\!O \quad + \quad H_2C\!=\!CH_2$$

(42 amu)   (28 amu)

C$_2$ path

(70 amu)   C$_3$ path

$$H_2C^{\bullet} \qquad {}^{\bullet}CH_2$$

(42 amu)   + $C\!\equiv\!O$

(42 amu)   (28 amu)

$H_2C\!-\!CH_2$ $H_2C \qquad CH_3$

(42 amu)   (42 amu)

The fact that the products of both channels have overlapping masses makes identification of the trimethylene species difficult by standard techniques of TOF mass spectrometry. This accidental overlap of fragment masses may be avoided via deuterium substitution. In the 2,2,4,4-d$_4$-cyclobutanone system, for example, the products of the C$_2$ channel have masses 44 and 30 amu, while for the C$_3$ channel, the product masses are 46 and 28 amu. Hence, isolation of the trimethylene signal is possible in deuterium-labeled isotopes.

Decarbonylation of the cyclobutanone precursor is induced by a two-photon process (as confirmed by power dependence studies of related cyclic and acyclic ketone molecules), given a pump wavelength of 2 × 310 nm. Spectroscopic studies in this region performed by O'Toole *et al.* have revealed an absorption spectrum rich with broad, overlapping Rydberg (n = 3) and valence bands.[26] The resulting unimolecular reaction (C$_3$ path) from this high energy will create a vibrationally

excited diradical species, as well as the residual carbon monoxide species (and C_2-channel products). The evolution of the reaction is probed by multi-photon absorption of the 620 nm probe pulse to the ionization potential of the precursor of fragment species of interest. The mechanism of the cyclobutanone dissociation, as well as the partitioning of the available energy to the fragment species is discussed further in Section IV.C.

C. Data Analysis

Autocorrelation traces of the 620 nm probe pulses were fitted to a Gaussian function with width (hwhm) of 40 ± 20 fs. The cross correlation of the pump and probe pulses, *i.e.* the instrumental response function, was taken to be ~ 70 ± 20 fs (hwhm).

Two types of data were obtained: complete TOF mass spectra, which could be recorded at different (discrete) time delays, and time-resolved transients, in which the temporal behavior of an individually selected mass peak of the TOF spectrum was selected and monitored. The mass spectra were recorded by a digital oscilloscope with a mass resolution $m/\Delta m \approx 150$. The ion signal for a specific mass was selected using a gated boxcar integrator. Transients were then obtained by monitoring the signal as a function of the delay time between the pump and probe pulses.

Transients were analyzed by fitting the data to an appropriate molecular response function convoluted with the cross-correlation (instrument-response) function. A least-squares fitting routine using commercial software (Scientist, Micromath) was employed for this purpose.
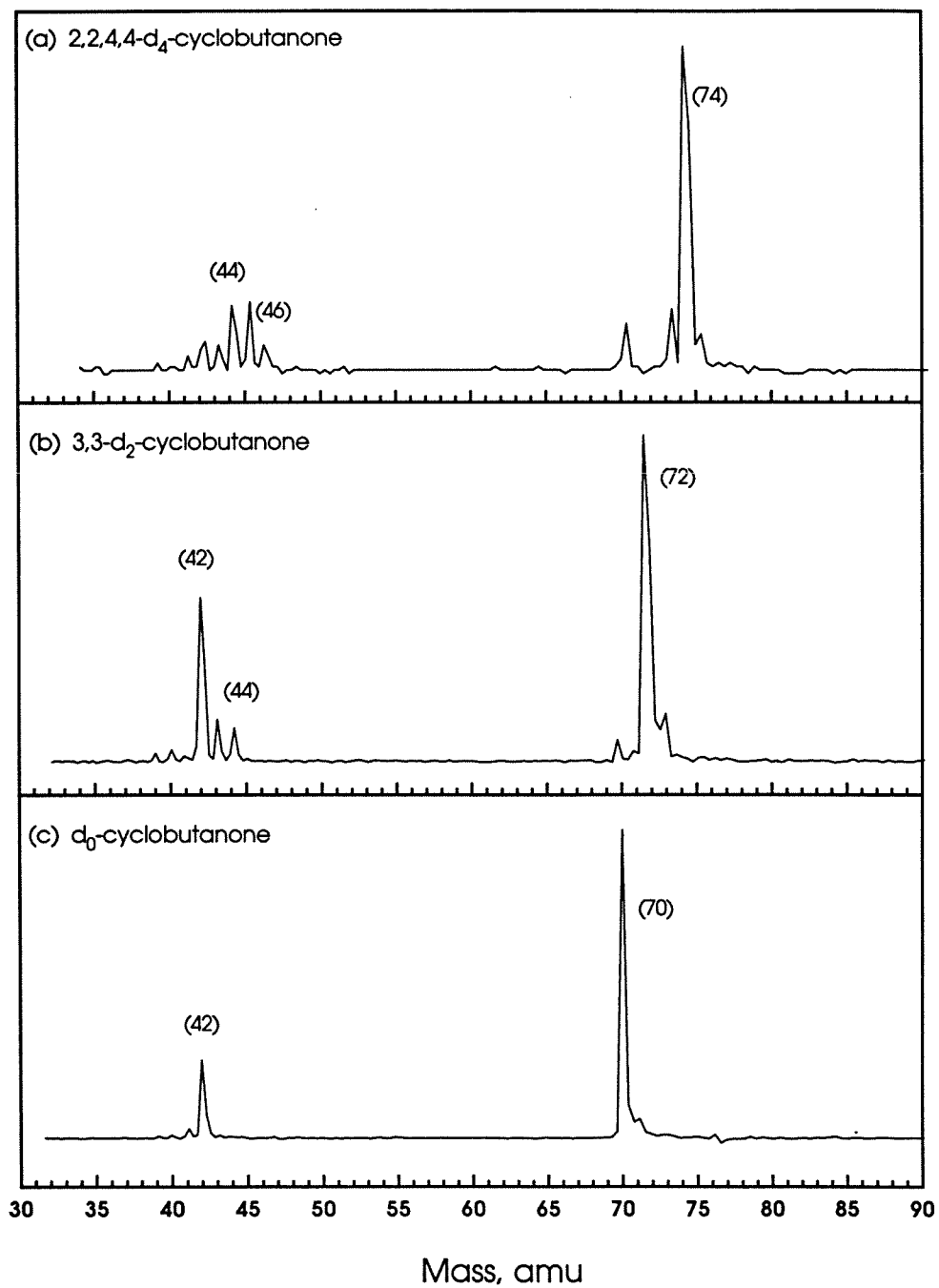
Figure 3.2 Time-of-flight mass spectra for cyclobutanone systems. Excitation is by a 310 nm pump pulse followed approx. 50 fs by a 620 nm probe pulse.

III.   Results

A.   Mass Spectra

The TOF mass spectra recorded ~50 fs after time zero are presented in Fig. 3.2 for cyclobutanone and its deuterated isotopes. For each system, the parent ion signal dominates, while fragment species for both the C_2 and C_3 channels appear at earlier times with significantly lower intensities. For the d_0-cyclobutanone system in panel (c), the peak at mass 42 contains both C_2 (ketene) and C_3 (trimethylene, cyclopropane, propylene, etc.) signal, whereas in the deuterated systems, a fragment cluster appears, cleanly separating the products of the C_2 and C_3 channels.
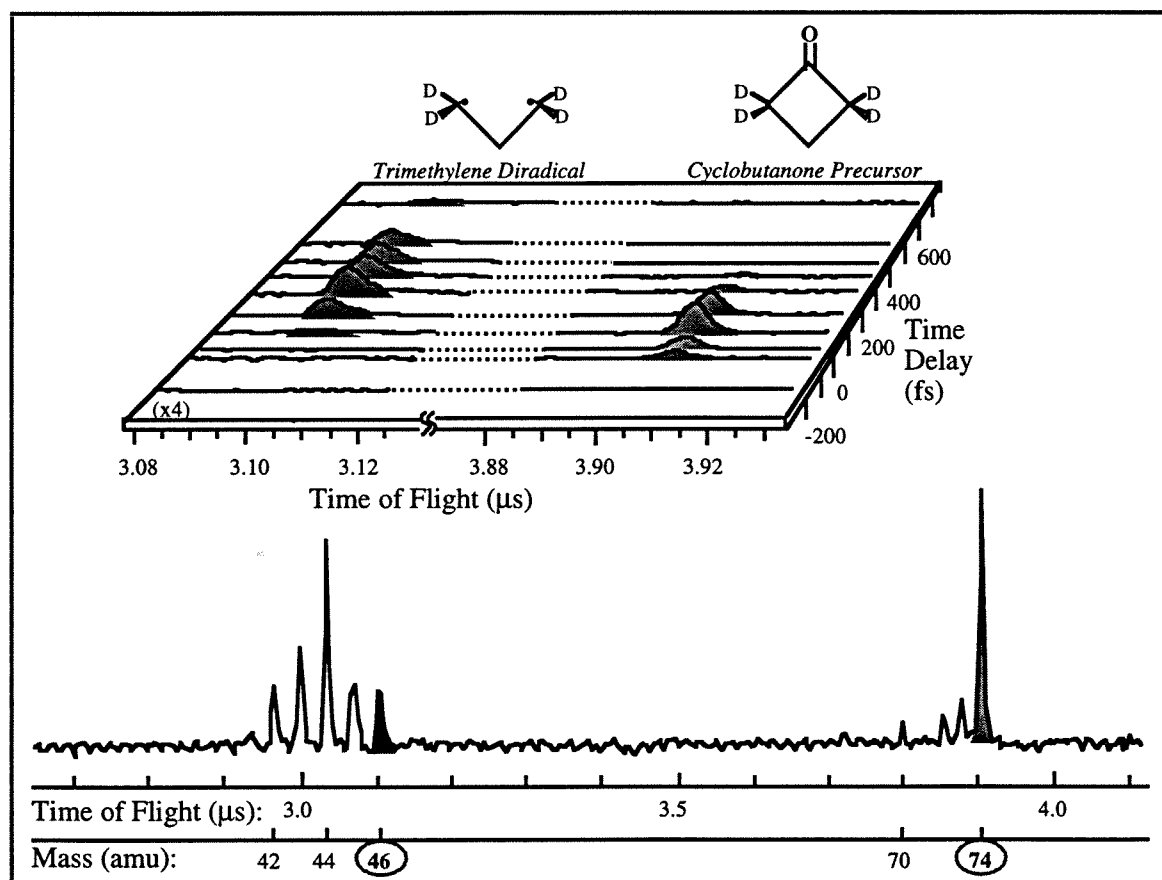

Figure 3.3   Mass spectra obtained for different pump-probe delay times. The precursor molecule, here 2,2,4,4-d4-cyclobutanone (74 amu) appears at time zero and promptly decays. The fragment signal (46 amu) appears later, peaking at about 300 fs and decays within a few hundred fs.

The mass spectra obtained at different time delays are shown in Fig. 3.3 for the 2,2,4,4-d_4-cyclobutanone system (chosen for the clean resolution of C_2 and C_3 fragment peaks). At negative times, *i.e.* when the probe arrives before the pump pulse, there is no signal present. At time zero, the cyclobutanone precursor signal (74 amu) is observed, while the fragment mass of 46 amu is not yet apparent. As the time delay increases, we observe the decrease of the precursor signal and the evolution of the fragment signal. The fragment signal peaks at about 200 fs after time zero, then decays back to zero within a few hundred fs. These mass spectra were recorded with low probe intensities to minimize signal resulting from ionic fragmentation channels (*vide infra*).
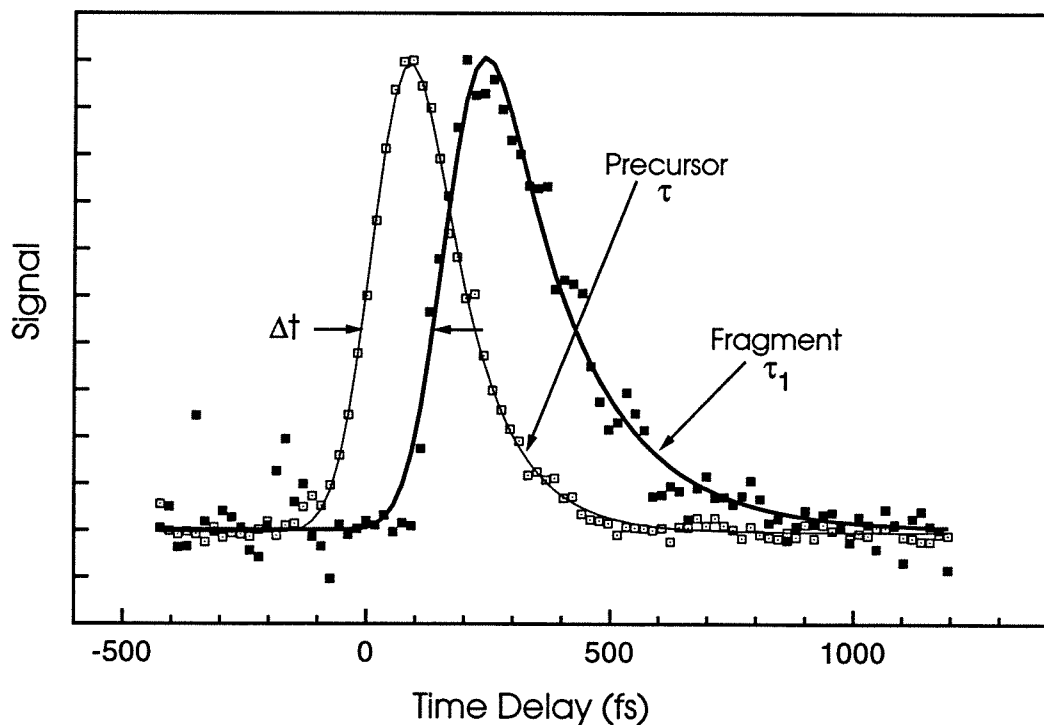
B. Femtosecond Transients

Figure 3.4 Femtosecond transients for precursor (m/e = 74) and fragment (m/e =46) species in 2,2,4,4-d₄- cyclobutanone system.

Typical femtosecond transients are shown in Fig. 3.4. Again, the 2,2,4,4-d_4-cyclobutanone system is presented, as the mass spectrum allowed clean separation of the fragment species corresponding to the decarbonylated precursor (parent − CO). Also for these experiments, the probe was kept attenuated such that no ion signal was generated by multiphoton absorption of the probe pulse alone.

C. Intense Probe Effect

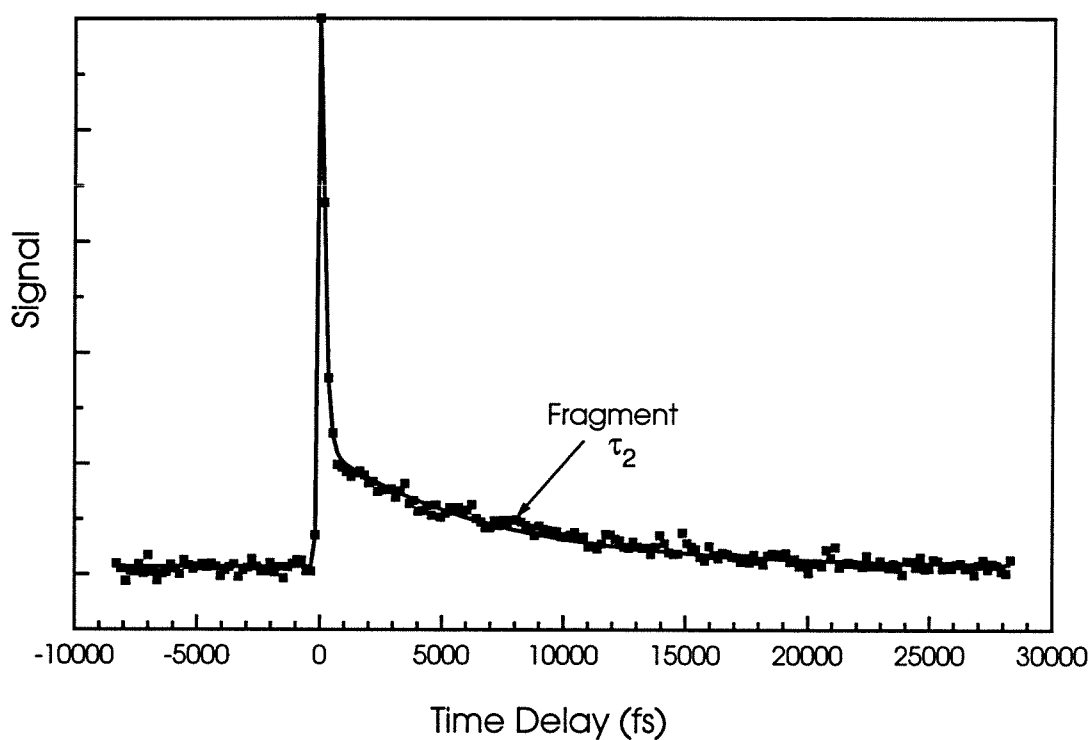**Figure 3.5** Picosecond transient of the fragment (m/e = 42) species in the d_0-cyclobutanone system.

Upon increasing the intensity of the probe beam, two significant effects were observed in the transients recorded for the mass peak corresponding to the decarbonylated precursor. Most apparent was the growth of a signal component due to ionic fragmentation which was identical to that of the precursor. Indeed,

only with extreme attenuation of the probe laser could this component be removed and the weak time-shifted signal be isolated. Also present at high probe intensities was a weak signal that persisted for some picoseconds (see Fig. 3.5). This component could not be completely isolated, for it was always accompanied by the precursor-type signal described above. Nonetheless, the transient was observed reproducibly with an intensity of approximately 10% of the time-shifted fragment signal. Note that this picosecond component was observed only in the fragment (m/e = precursor − CO) transient; it was not present in the precursor transients.

Hence three components are observed in the transients recorded for the mass peak corresponding to the decarbonylation precursor:

(1) Precursor-like signal. As this component is identical to the precursor signal, *i.e.* with a rise dictated by the instrumental response and a single-exponential decay with an associated time constant of approximately 105 fs, it is identified as being due to fragmentation of the precursor ion.

(2) Femtosecond component. This component, isolated upon weak probe conditions, is shifted from the precursor signal by ~155 fs. The rise is sharp, analogous to that of the precursor, but the decay is slightly longer. A single exponential fit yields a time constant of 122 ± 12 fs for the d_0-cyclobutanone system.

(3) Picosecond component. While the rise is obscured by the presence of the precursor-like signal, this small component persists for ~6 ps for the d_0-cyclobutanone system.

In addition, given the problem of overlapping masses in the d_0-cyclobutanone system, the transient recorded for the fragment mass in this system is complex, containing both C_2- and C_3-channel signal. From studies of the deuterated isotopes, where the fragments could be isolated, it was observed that the signal due to the C_2

fragment channel followed exactly that of the precursor, suggesting that its origin is simply fragmentation of the precursor ion. No unique dynamics were observed for this fragment. Hence, the C_3 channel signal in the d_0-cyclobutanone experiments could be extracted by fitting the observed fragment transient to a sum of two single exponential decay functions, with one matching the precursor and the other time shifted by a constant ~155 fs.

D. *Deuterium Substitution*

When the same dynamical processes were probed on deuterium-labeled systems, interesting effects were observed. First, it is important to note that the decay of the precursor mass peak is unaffected by isotopic substitution. In each of the three systems, cyclobutanone, 3,3-d_2-cyclobutanone, and 2,2,4,4-d_4-cyclobutanone, the parent decay is fit to a single exponential with a time constant of 105 ± 10 fs. Furthermore, the time delay between the precursor and fragment transient signals is, within the estimated uncertainty, independent of deuterium substitution (see Table 3.1), approximately 155 ± 15 fs.

Given the problem of overlapping masses, however, the transient recorded for the fragment mass is complex, containing both C_2- and C_3-channel signal. The signal due to the ketene (C_2 product) was found to follow exactly that of the precursor, suggesting that its origin is simply fragmentation of the precursor ion. Even in the deuterated systems where isolation of the ketene signal was possible, no unique dynamics were observed for this fragment.

The subsequent dynamics of the fragment species (*i.e.* the mass peak corresponding to decarbonylation of the precursor) do exhibit significant isotope effects. On the femtosecond time scale, deuterium substitution on the middle carbon atom results in no significant change in the lifetime of this fragment. When the hydrogen atoms on the terminal carbons are replaced by deuterium, however,

this lifetime increases by a factor of 1.5. These results are summarized in Table 3.1.

Table 3.1. Deuterium isotope effect on fs dynamics

Compound	Δt, fs	τ_1, fs
d_0-trimethylene	155 ± 10	122 ± 12
2,2-d_2-trimethylene	160 ± 10	129 ± 10
1,1,3,3-d_4-trimethylene	150 ± 10	183 ± 12

The small picosecond component observed in the fragment transients at high probe intensities was also affected by deuterium substitution, see Table 3.2. The ratio of extracted time constants for d_0-, 2,2-d_2-, and 1,1,3,3-d_4-trimethylene is approximately 1 : 2 : 1.5.

Table 3.2. Deuterium isotope effect on ps dynamics

Compound	τ_2, ps
d_0-trimethylene	6.2 ± 0.5
2,2-d_2-trimethylene	12.1 ± 0.8
1,1,3,3-d_4-trimethylene	8.7 ± 0.5

E.   Energy Dependence

As noted previously, the experiments were performed with a pump wavelength of 310 nm. The 2-photon excitation of the precursor molecule generated trimethylene at a total energy E = 99 kcal/mol (see Section IV.C.). Pump tuning experiments were performed on the 2,2,4,4-d_4-cyclobutanone system (again selected

for fragment resolution), varying the total energy by −5 and +18 kcal/mol. No significant change in the time constants for each detected species was observed, though poor signal to noise ratios and increased laser pulse widths precluded a precise analysis of the transient dynamics. Crude fits of the femtosecond transients, however, yielded time constants of 190 ± 40 fs.

IV. Discussion

From the above results, we can deduce the reaction mechanisms of the diradical species, as well as the mechanism of their formation. We begin by exploring the possible reaction channels available to the trimethylene, as well as details of the potential energy surface involved. A postulated mechanism is then compared with theoretical analyses of reaction rates and isotope effects. In the final section, we discuss the entry channel for formation of trimethylene from the cyclobutanone precursor.

A.   *Reactivity and Mechanism*

1. Possible Decay channels

Scheme 3.4
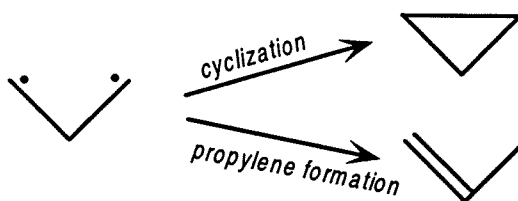
Trimethylene can decay to form two products: cyclopropane and propylene. Various pathways are possible for each of the channels. Considering cyclization,

the precise mechanism for linkage of the terminal carbons depends on trimethylene's initial conformation. Three possible (idealized) rotamers can be defined, labeled (0,0), (0,90), and (90,90) according to the angles by which each of the terminal methylenes is twisted out of the carbon plane.[27]

(0,0)   (0,90)   (90,90)
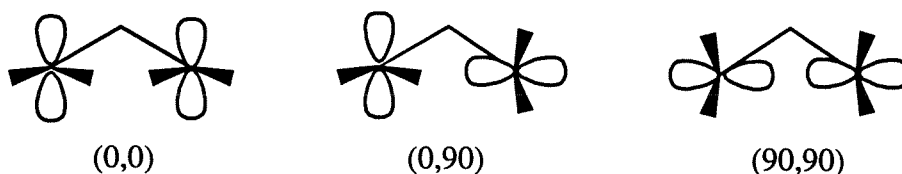
Each of these rotamers may cyclize to form a carbocyclic ring. The (0,0) and (0,90) geometries, however, must first undergo rotation prior to formation of cyclopropane. Double rotation via a (0,0)-trimethylene will lead to cyclization, as will single rotation involving a (0,90)-trimethylene:

Scheme 3.5

Double twist
conrotatory

Double twist
disrotatory

Single twist
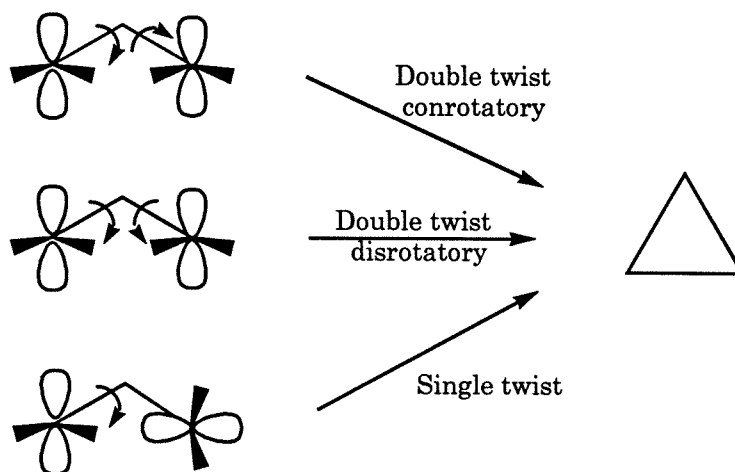
For trimethylene to form propylene, rearrangement of the hydrogen atoms is necessary. The most direct mechanism involves a 1,2-hydrogen transfer from the

central to carbon to either terminus. This rearrangement will shift the electron density so as to form a double bond. Alternatively, a 1,3-hydrogen transfer between the two terminal methylene groups will form ethylcarbene, an unstable intermediate which will promptly undergo 1,2-hydrogen transfer to give propylene.[28] These two pathways, direct and stepwise formation of propylene, are shown schematically below:

Scheme 3.6
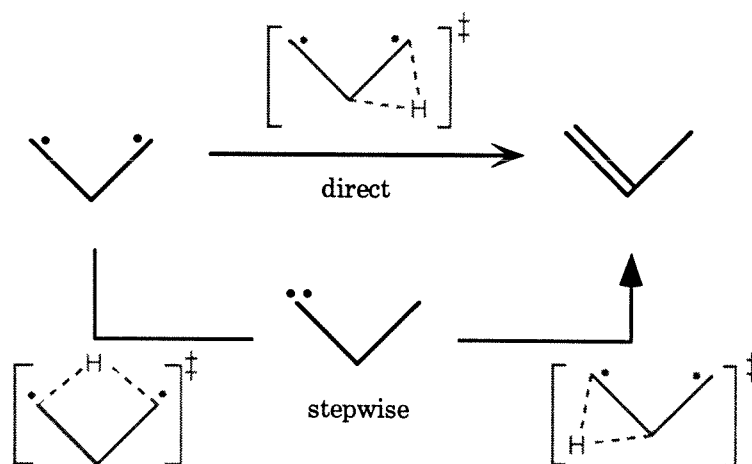
2. Energetics and Potential Energy Surfaces

As an intermediate species, trimethylene must lie in a shallow potential well at the top of the pass connecting cyclopropane and propylene, as shown schematically in Fig. 3.6. Transition states for ring closure and rearrangement mark the highest points of the potential. While consistent with many experimental observations and thermodynamic calculations, the validity of such a picture has been questioned by several quantum theoretical calculations which indicate no barrier to ring closure to cyclopropane. An accurate representation of the energetics involved in the interconversion of cyclopropane and propylene via the

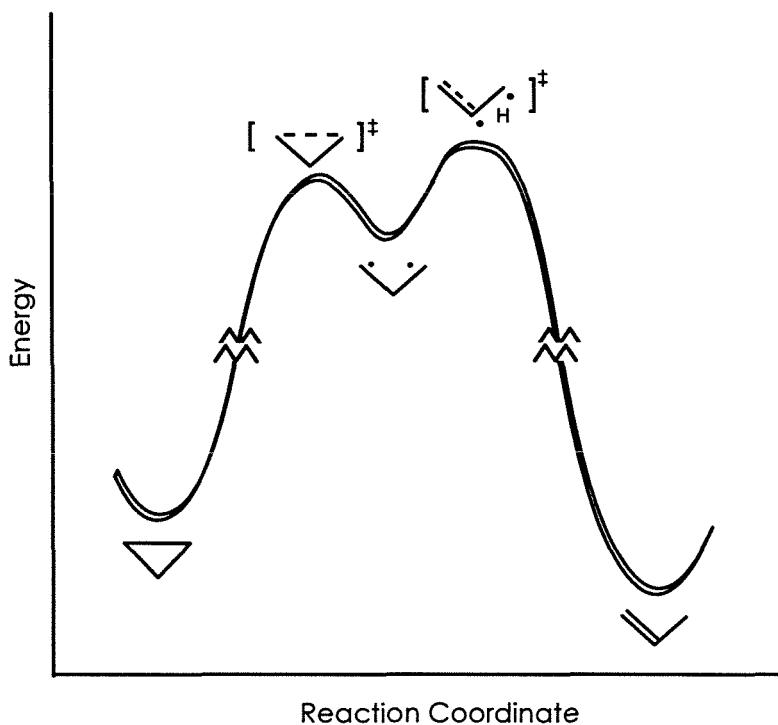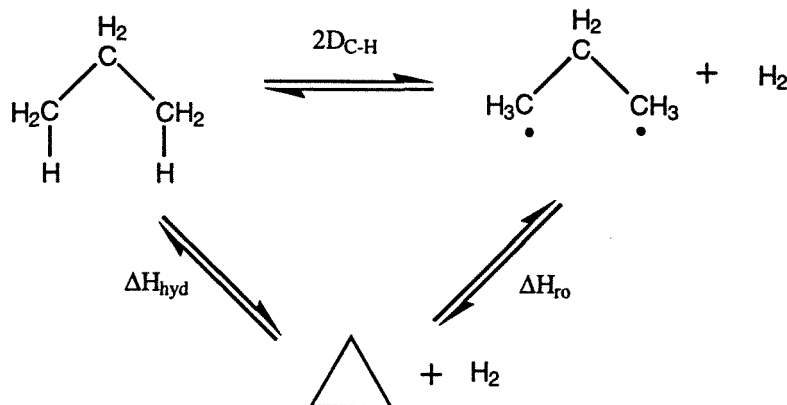proposed trimethylene intermediate is crucial to our understanding of the associated mechanism.

Figure 3.6 Schematic potential energy curve along the reaction coordinate associated with the cyclopropane-propylene isomerization reaction.

Scheme 3.7

A thermodynamic cycle may be employed to calculate the energies of the intermediates and transition states using experimentally-obtained activation energies and enthalpies. Bergman shows[21] how the heat of formation of trimethylene can be estimated by the thermodynamic cycle illustrated in Scheme 3.7. The ring-opening energy ΔH_{ro} is equal to the energy required to first hydrogenate cyclopropane to propane and then remove two hydrogen atoms from the terminal carbons:

$$\Delta H_{ro} = \Delta H_{hyd} + 2D_{C-H} - D(H_2) \,,$$

where ΔH_{hyd} may be calculated by the difference in heats of formation of cyclopropane and propane. An implicit assumption in this procedure is that the two C-H bond strengths in propane and propyl are identical. In 1968, Benson applied this cycle to calculate a ring-opening energy[29] that was 9.3 kcal/mol below the energy of the transition state for geometrical isomerization (stereomutation).[30]

While recent upward revisions of C-H bond strengths serve to raise the enthalpy of formation of trimethylene by about 5 kcal/mol,[31] a barrier of 4.3 kcal/mol to ring closure still defines trimethylene as a thermodynamically-stable intermediate.[32]

Quantum theoretical attempts at describing the trimethylene diradical, however, have never found a significant barrier to ring closure. Hoffmann's early extended Hückel calculations[27] located a minimum on the trimethylene surface for the (0,0) rotamer. The lowest-energy barrier for ring closure to cyclopropane was found to be ~1 kcal/mol, corresponding to conrotatory rotation of the terminal methylene groups.

Subsequent *ab initio* calculations[33-52] have employed both the (0,0) and (0,90) trimethylene rotamers in studies of cyclopropane stereomutations. While the results concur with Hoffmann's finding that the (0,0) rotamer is an intermediate,

the energy difference between the (0,0) and (0,90) geometries is very small, less than 1 kcal/mol (see Ref. 50 for review). In general, the potential energy surface has been found to be relatively flat with respect to rotation of the terminal methylene groups. While significant in describing stereomutation dynamics, the "moguls" in the potential energy surface reflect subtleties in single- and double-rotation processes and are likely negligible in characterizing ring-closure and rearrangement schemes.

Ignoring the subtleties of the potential energy surface, then, the relevant energetics of trimethylene and its products via cyclization and rearrangement processes are shown in Fig. 3.7. The ground state energies are given by the measured heats of formation. The energy of trimethylene is approximated to be the same as the measured activation energy for *cis-trans* isomerization.
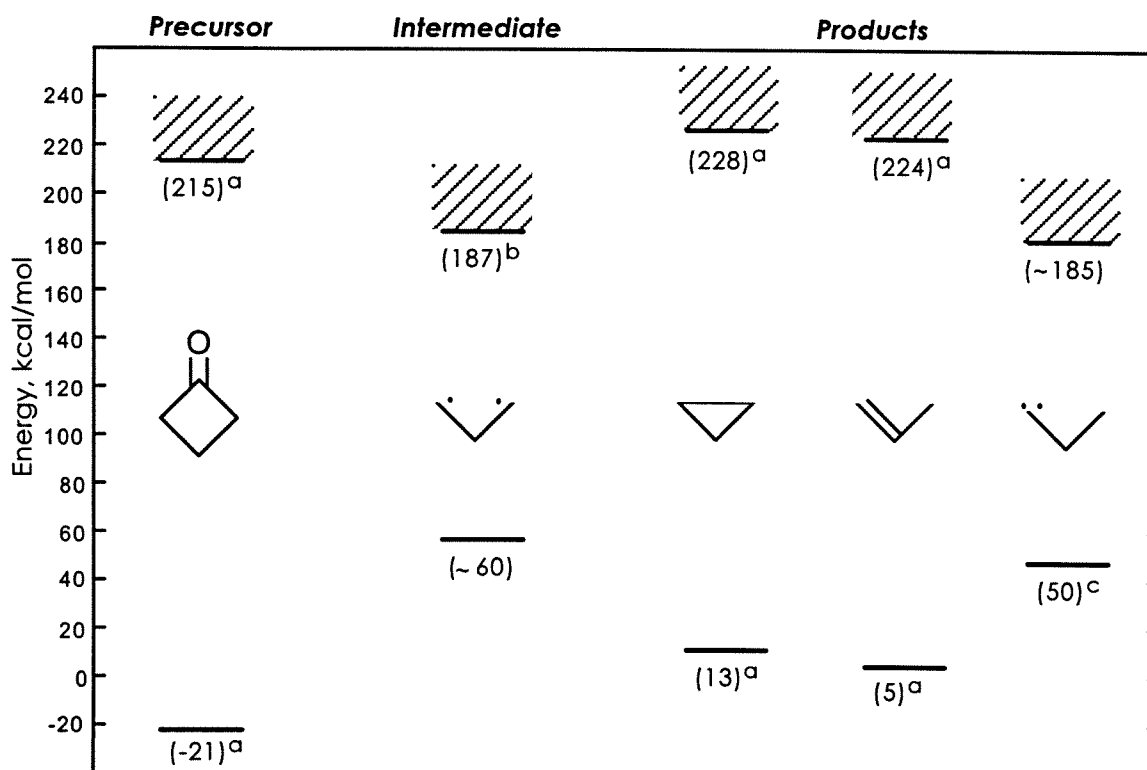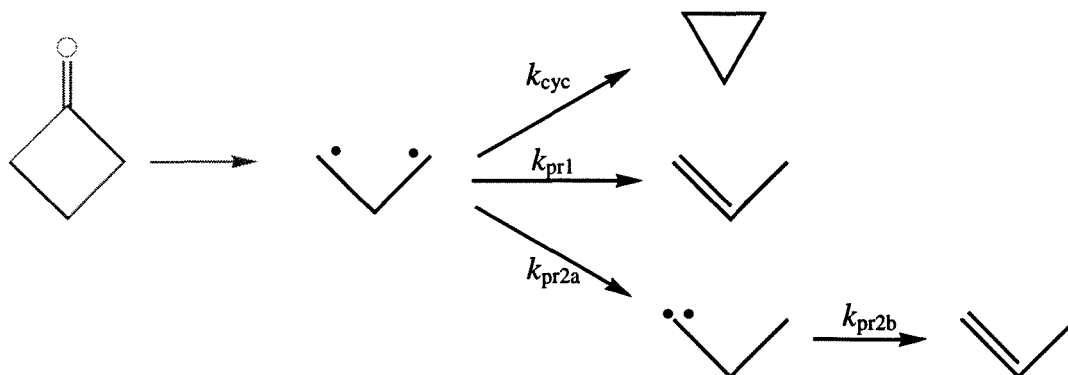

Figure 3.7 Ground-state energies and ionization potentials for cyclobutanone system. The superscripts correspond to the following references: a = Ref. 53; b = Ref. 54; and c = Ref. 55.

3. Kinetic Models

Scheme 3.8

To help illustrate the reaction mechanism, simple kinetic models are developed to relate the transients to the various rates involved. In a kinetic model, the continuous nature of the system's evolution on the potential surface is neglected; instead, the reaction is represented by transitions between discrete states, as shown in Scheme 8. The model predicts the dependence of the signal on decay rates, power of the pulses, and absorption cross sections. Naturally, to consider the continuous nature of the motion, including coherence effects, the equations of motion must be solved in all possible configurations, be it done classically, semiclassically, or quantum mechanically.

The kinetic model ignores the dissociation of the cyclobutanone precursor and instead begins with the trimethylene intermediate (see Sec. IV.C for discussion of the entry channel). All three decay channels discussed above, cyclization, direct propylene formation, and indirect propylene formation via ethylmethylene, are included, with associated rate constants k_{cyc}, k_{pr1}, and k_{pr2}, respectively (see Scheme 3.8). The rate constant for cyclization, k_{cyc}, reflects all possible ring-closure

channels (conrotatory, disrotatory, etc.), as the slight differences in the potential energy surfaces are expected to be negligible at our energies.
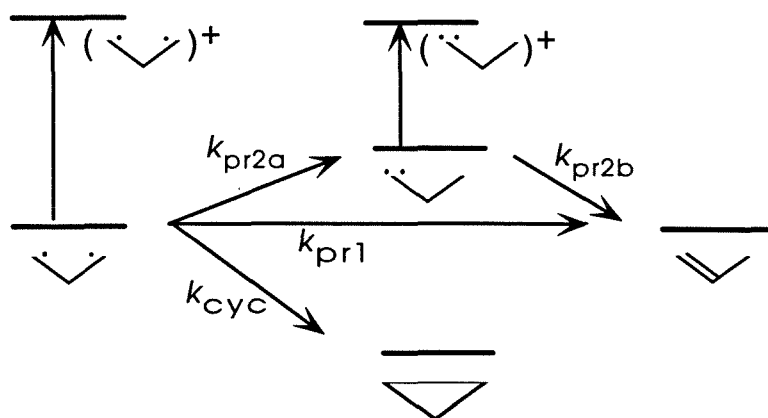
Figure 3.8. Level diagram for kinetic model.

A level diagram of the kinetic model, including the final states accessed by the probe pulse, is shown in Fig. 3.8. If we assume that both trimethylene and ethylmethylene are sampled by the probe laser, then the observed signal will reflect the dynamics of both species. As our detection scheme cannot distinguish trimethylene (m/e = 42) and ethylmethylene (m/e = 42), the ion signal will be the sum of the two contributions. If it could be isolated, the signal corresponding to the trimethylene diradical would be a single exponential decay with an associated time constant (reflecting the lifetime of trimethylene) of $\tau = (k_{cyc} + k_{pr1} + k_{pr2a})^{-1}$. The signal corresponding to the ethylmethylene would be characterized by a biexponential function. The rise would be determined not simply by k_{pr2a}, but by considering the overall decay of the trimethylene precursor. The decay of this signal would be given by k_{pr2b}.

The transients simulated by this model reproduce the observed dynamics, given time constants on the order of 100 fs for k_{cyc} and k_{pr1}, 10 ps for k_{pr2a}, and 5 ps for k_{pr2b}.

4. Interpretation of Observed Transients

The shapes and associated time constants of the observed transients provide direct insight into the nature of the diradical. By analyzing the qualitative features and trends, we begin to deduce the mechanism of the reaction.

a. Lifetime of Diradical

Considering the predominant signal observed for the mass species corresponding to the precursor minus CO, we recognize a short-lived intermediate, most likely corresponding to the trimethylene diradical. The signal appears after a delay of approximately 150 fs, and decays with at time constant of 120 fs. The single exponential fit to the data reflects a statistical decay process, indicating that the trimethylene diradical must exist in a shallow potential well. For if the trimethylene were purely a transition-state species along the reaction coordinate, we would expect a signal characteristic of a wave packet (*i.e.* having no discernible decay). Instead, the system lingers for some time before continuing on to form products.

Considering the dynamics of the nuclei at the top of the barrier, it is impossible at these velocities to achieve such time scales if a wave packet is moving translationally on a flat surface. For example, over a distance of 0.5 Å, the time in the transition-state region will be approx. ~50 fs. To explain the observed times, other degrees of freedom must be involved (*vide infra*).

b. Femtosecond Dynamics and Mechanism

The observed transients immediately implicate ring closure to cyclopropane as the major decay channel. Such a processes requires minimal nuclear motion of the carbon skeleton; only rotation of the terminal methylene groups is necessary. Hence kinetic isotope effects should be limited to the terminal methylene groups. Indeed, our experiments showed that deuterium substitution at the central carbon had little effect on the femtosecond dynamics, while at the terminal carbons, the trimethylene lifetime increased by a factor of 1.5.

Direct propylene formation involves a 1,2-hydrogen exchange mechanism, hence a significant kinetic isotope effect should be observed in the trimethylene decay for the 2,2-d_2-trimethylene relative to the d_0-trimethylene. The lack on any effect on the observed dynamics suggests that this channel is not a major decay pathway for trimethylene.

c. Picosecond Dynamics

The origin of the picosecond component which overlaps the trimethylene signal is likely due to a second active decay channel involving 1,3-hydrogen exchange to form ethylcarbene. Doubleday was the first to recognize such a trajectory in considering the lifetime of the trimethylene intermediate.[52] Formation of ethylcarbene from trimethylene is expected to be at least an order of magnitude slower than direct processes such as ring closure. As such, evidence of this channel does not appear in the trimethylene decay, whose associated time constant is dominated by the faster channels of cyclization and direct propylene formation.

Probing the ethylcarbene so formed will result in an added component to the trimethylene signal, as both species share the same mass. The buildup of the ethylcarbene signal is determined by the decay of its precursor, namely the trimethylene intermediate. Hence, despite the fact that the time constant

associated with 1,3-hydrogen exchange is on the order of picoseconds, the signal will grow in on a time scale equal to the lifetime of the trimethylene, ~ 100 fs.

The lifetime of the ethylcarbene is measured to be on the order of picoseconds, given the decay of the transient signal. The ethylmethylene is expected to undergo a second rearrangement, this time a 1,2-hydrogen exchange to form propylene. The significant kinetic isotope effect observed for the deuterium-labeled diradicals supports this mechanism.

B. Comparison with Theory

The direct observation of the trimethylene diradical in these experiments marks a significant step toward understanding the overall reactivity and mechanisms of diradicals in organic reactions. Further analyses must couple the results of experimental stereochemical studies as well as theoretical calculations.

Recent calculations by Doubleday demonstrate the applicability of variational unimolecular rate theory in predicting the lifetime of trimethylene.[52] Despite the ultrafast time scales (which often reflect a markedly non-statistical behavior), the calculations predicted the lifetime of trimethylene in excellent agreement with the experimental observation: $\tau_{calc} = 118$ fs *vs.* $\tau_{obs} = 122 \pm 12$ fs at a total energy of 99 kcal/mol.

The calculated trimethylene lifetime included consideration of both cyclization and rearrangement channels. The rate constants for ring closure (conrotatory and disrotatory) and direct propylene formation were nearly identical, both on the order of 2×10^{12} s^{-1}.[52] The rate constant for 1,3-hydrogen transfer to form ethylmethylene, however, is predicted to be 2 orders of magnitude smaller, $k_{em} = 2 \times 10^{10}$ s^{-1} and hence is negligible in consideration of the trimethylene lifetime.[52] This latter prediction serves as validation of our assignment of the picosecond component of our fragment transient to ethylmethylene formation.

Further support for the proposed mechanism comes in comparisons with predicted isotope effects. Baldwin recently calculated the deuterium kinetic isotope effects for trimethylene ring closure.[51,56] The relative lifetimes for d_0-, 2,2-d_2-, 1,1,3,3-d_4-, and d_6-trimethylene are estimated to be 1.00, 1.01, 1.35, and 1.37. The experimental results for d_0-, 2,2-d_2-, and 1,1,3,3-d_4- diradicals are in good agreement: 1.00, 1.06 ± 0.1, and 1.5 ± 0.2.

C.   The Entry Channel

The cyclobutanone precursor must undergo decarbonylation to yield the trimethylene diradical. The mechanism of such a process, an example of Norrish type-I α-cleavage, has been studied extensively.[57]

Scheme 3.9
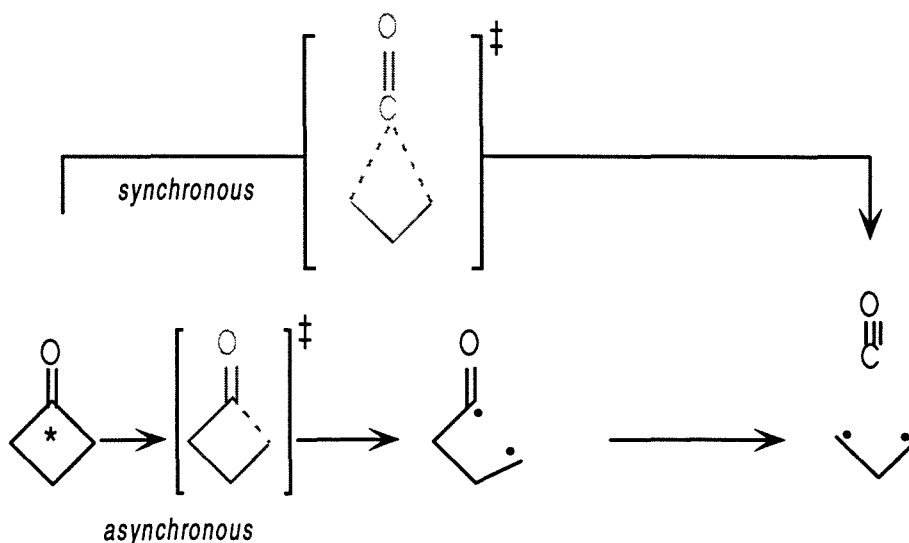
The excited cyclobutanone, given its rigid structure, may dissociate synchronously by a symmetric stretch of the two C–C bonds adjacent to the carbonyl, thereby extruding the C≡O fragment. As such, the system will retain its

initial coherence, forming the trimethylene intermediate with little change in nuclear configuration at a time delay of ~150 fs.

Alternatively, the excited cyclobutanone precursor may undergo an asynchronous dissociation process, in which a single C–C bond adjacent to the carbonyl is broken, forming a 1,4-acyl-alkyl diradical. The impulsive scission of the C–C bond snaps open the ring, creating a floppy intermediate with significant excess energy. The subsequent internal energy redistribution may lead to a number of reaction products, including cyclization to reform cyclobutanone, H-atom exchange to form various unsaturated species, or decarbonylation to leave trimethylene. The rate constant corresponding to the decay of this species will reflect the sum of all processes involved.

V.   Conclusions

The application of femtosecond spectroscopy to studies of ring-opening reactions provides new insight to the nature of diradicals. Trimethylene and related 1,3-diradicals are observed directly, validating their existence as intermediates in the structural and geometrical isomerization reactions of cyclopropane, first proposed more than 60 years ago.

The real-time evolution of trimethylene is related to a reaction mechanism involving both cyclization and rearrangement channels. Direct decay to cyclopropane is observed to occur on a time scale of femtoseconds, while rearrangement to form propylene requires a two-step process (involving formation of an ethylmethylene intermediate) that is completed in picoseconds. Direct 1,2-H-atom transfer to form propylene is not a major decay channel, according to the observed kinetic isotope effects.

Further studies of 1,3 diradicals are needed to establish the nature of the global PES. For example, initiating the reaction from different precursors will help with mapping the PES and identifying the available dynamical routes.

References

[1]   *Diradicals* , edited by W. T. Borden (Wiley, New York, 1982).

[2]   T. S. Chambers and G. B. Kistiakowsky, J. Am. Chem. Soc. **56,** 399 (1934).

[3]   B. S. Rabinovich, E. W. Schlag, and K. B. Wiberg, J. Chem. Phys. **28,** 504 (1958).

[4]   M. R. Willcott and V. H. Cargle, J. Am. Chem. Soc. **91,** 4310 (1969).

[5]   J. A. Berson and J. M. Balquist, J. Am. Chem. Soc. **90,** 7343 (1968).

[6]   W. Carter and R. G. Bergman, J. Am. Chem. Soc. **90,** 7344 (1968).

[7]   R. G. Bergman and W. Carter, J. Am. Chem. Soc. **91,** 7411 (1969).

[8]   R. J. Crawford and T. R. Lynch, Can. J. Chem. **46,** 1457 (1968).

[9]   A. Chmurny and D. J. Cram, J. Am. Chem. Soc. **95,** 4237 (1973).

[10]   W. von E. Doering and K. Sachdev, J. Am. Chem. Soc. **96,** 1168 (1974).

[11]   J. A. Berson and L. D. Pederson, J. Am. Chem. Soc. **97,** 238 (1975).

[12]   J. A. Berson, L. D. Pederson, and B. K. Carpenter, J. Am. Chem. Soc. **97,** 240 (1975).

[13]   J. A. Berson, L. D. Pederson, and B. K. Carpenter, J. Am. Chem. Soc. **98,** 122 (1976).

[14]   J. T. Wood, J. S. Arney, D. Cortes, and J. A. Berson, J. Am. Chem. Soc. **100,** 3855 (1978).

[15]   W. Kirmse and M. Zeppenfeld, J. Chem. Soc. Chem. Commun. , 124 (1977).

[16]   W. von E. Doering and E. A. Barsa, Tetrahedron Lett. 2495 (1978).

[17]   W. von E. Doering and E. A. Barsa, Proc. Natl. Acad. Sci. U.S.A. **71,** 2355 (1980).

[18]   J. E. Baldwin and C. Carter, J. Am. Chem. Soc. **100,** 3942 (1978).

[19]   J. E. Baldwin and C. Carter, J. Am. Chem. Soc. **101,** 1325 (1979).

[20] J. E. Baldwin and C. G. Carter, J. Am. Chem. Soc. **104,** 1362 (1982).

[21] R. G. Bergman, in *Free Radicals*, edited by J. K. Kochi (Wiley, New York, 1973), pp. 191.

[22] P. B. Dervan and D. A. Dougherty, in *Diradicals*, edited by W. T. Borden (Wiley, New York, 1982), pp. 107.

[23] P. B. Dervan and D. S. Santilli, J. Am. Chem. Soc. **102,** 3863 (1980).

[24] J. C. Hemminger, C. F. Rusbult, and E. K. C. Lee, J. Am. Chem. Soc. **93,** 1867 (1971).

[25] K. A. Trentelman, D. B. Moss, S. H. Kable, and P. L. Houston, J. Phys. Chem. **94,** 3031 (1990).

[26] L. O'Toole, P. Brint, C. Kosmidis, G. Boulakis, and P. Tsekeris, J. Chem. Soc. Faraday Trans. **87,** 3343 (1991).

[27] R. Hoffmann, J. Am. Chem. Soc. **90,** 1475 (1968).

[28] *Kinetics and Spectroscopy of Carbenes and Biradicals*, Vol. , edited by M. S. Platz (Plenum Press, New York, 1990).

[29] H. E. O'Neal and S. W. Benson, Journal of Physical Chemistry **72,** 1866 (1968).

[30] E. W. Schlag and B. S. Rabinovitch, J. Am. Chem. Soc. **82,** 5996 (1960).

[31] W. von E. Doering, Proc. Natl. Acad. Sci. U.S.A. **78,** 5279 (1981).

[32] J. A. Berson, Science **266,** 1338 (1994).

[33] R. J. Buenker and S. C. Peyerimhoff, Proc. Natl. Acal. Sci. U.S.A. **78,** 1695 (1969).

[34] A. K. O. Siu, W. M. St.John, and E. F. Hayes, J. Phys. Chem. **92,** 7249 (1970).

[35] Y. Jean, L. Salem, J. S. Wright, J. A. Horsley, C. Moser, and R. M. Stevens, Pure Appl. Chem. Suppl. (23rd Congr.) **1,** 197 (1971).

[36] Y. Jean and L. Salem, J. Chem. Soc., Chem. Commun. , 382 (1971).

[37] E. F. Hayes and A. K. O. Siu, J. Am. Chem. Soc. **93,** 2090 (1971).

[38] J. A. Horsley, Y. Jean, C. Moser, L. Salem, R. M. Stevens, and J. S. Wright, J. Am. Chem. Soc. **94,** 279 (1972).

[39] P. J. Hay, W. J. Hunt, and W. A. Goddard III, J. Am. Chem. Soc. **94**, 638 (1972).

[40] K. Yamaguchi and T. Fueno, Chem. Phys. Lett. **22**, 471 (1973).

[41] Y. Jean and X. Chapuisat, J. Am. Chem. Soc. **96**, 6911 (1974).

[42] X. Chapuisat and Y. Jean, J. Am. Chem. Soc. **97**, 6325 (1975).

[43] K. Yamaguchi, K. Ohta, S. Yabushita, and T. Fueno, Chem. Phys. Lett. **79**, 555 (1977).

[44] K. Yamaguchi, A. Nishio, S. Yabushita, and T. Fueno, Chem. Phys. Lett. **53**, 109 (1978).

[45] S. Kato and K. Morokuma, Chem. Phys. Lett. **65**, 19 (1979).

[46] C. Doubleday, J. W. McIver, and M. Page, J. Am. Chem. Soc. **104**, 6533 (1982).

[47] A. H. Goldberg and D. A. Dougherty, J. Am. Chem. Soc. **105**, 284 (1983).

[48] Y. Yamaguchi, Y. Osamura, and H. F. Schaefer, J. Am. Chem. Soc. **105**, 7506 (1983).

[49] C. Doubleday, J. W. McIver, and M. Page, J. Phys. Chem. **92**, 4367 (1988).

[50] S. J. Getty, E. R. Davidson, and W. T. Borden, J. Am. Chem. Soc. **114**, 2085 (1992).

[51] J. E. Baldwin, Y. Yamaguchi, and H. F. Schaefer, J. Phys. Chem. **98**, 7513 (1994).

[52] C. Doubleday, J. Phys. Chem. **100**, 3520 (1996).

[53] S. G. Lias, J. E. Bartmess, J. F. Liebman, J. L. Holmes, R. D. Levin, and W. G. Mallard, J. Phys. Chem. Ref. Data **17**, 76 (1988).

[54] P. Du, D. A. Hrovat, and W. T. Borden, J. Am. Chem. Soc. **110**, 3405 (1988).

[55] Y. Yamaguchi and H. F. Schaefer, J. Am. Chem. Soc. **106**, 5115 (1984).

[56] J. E. Baldwin, (personal communication).

[57] S. K. Kim and A. H. Zewail, Chem. Phys. Lett. **250**, 279 (1996).

4. Tetramethylene*

Perhaps the most-studied nonconjugated diradical is tetramethylene. Its behavior has been characterized by both theorists and experimentalists and is generally consistent with our chemical intuition of a "classic" diradical intermediate.[1] In this chapter, we present direct studies of this archetypal reactive intermediate by femtosecond pump-probe spectroscopy, a full account of the preliminary results presented in Ref. 2. Once again, the combination of laser and molecular beam techniques affords isolation of the elusive intermediate species, such that its evolution may be followed directly. The experiments presented here track the tetramethylene from its initial generation via decarbonylation of a cyclopentanone precursor to its decay by closure and cleavage channels. The observations establish the nature of the tetramethylene diradical as a true intermediate along the reaction coordinate. The effects of excess energy and substitution (methyl, deuterium) on the observed dynamics are related to the mechanism and the potential energy surface, as well as to recent calculations of electronic structure and reaction rates.

---

* Preliminary report given in S. Pedersen, J. L. Herek, and A. H. Zewail, *Science*, **266**, 1359 (1994).

I.   Background

The ring opening of cyclobutane to yield two ethylenes (or the reverse cycloaddition of two ethylenes to form cyclobutane) is a textbook example of a Woodward-Hoffmann concerted reaction.[3]

$$\square \rightleftharpoons \| + \| \qquad\qquad (1)$$
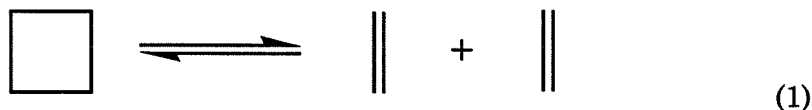
The correlation diagram for this system (Fig. 4.1) reveals the connection between a bonding reactant level with an antibonding product level, and vice versa. Hence, if orbital symmetry is to be conserved, a concerted reaction between ground state ethylene and cyclobutane is met with a large symmetry-imposed barrier. Note that a photochemical reaction does not suffer the same fate; an excited cyclobutanone molecule has no barrier to dissociation, as the antibonding orbital has the same symmetry as (and is therefore directly connected to) the ground state ethylenes.

Previous experimental studies of tetramethylene were capable of only indirect evidence for the existence of an intermediates species. In general, the experimental approach has been based on studies of the stereochemistry of reactants and products, chemical kinetics, and the effect of different precursors on the generation of diradicals. The time "clock" for rates is internal, inferred from the rotation of a single bond, and is used to account for any retention of stereochemistry from reactants to products. The problem with this approach is that rotational time constants may be much longer than the reaction trajectories. Studies of stereochemical retention are an inadequate test for establishing the nature of a chemical reaction (*i.e.* concerted, step-wise) in that the fundamental dynamics may not be directly correlated.
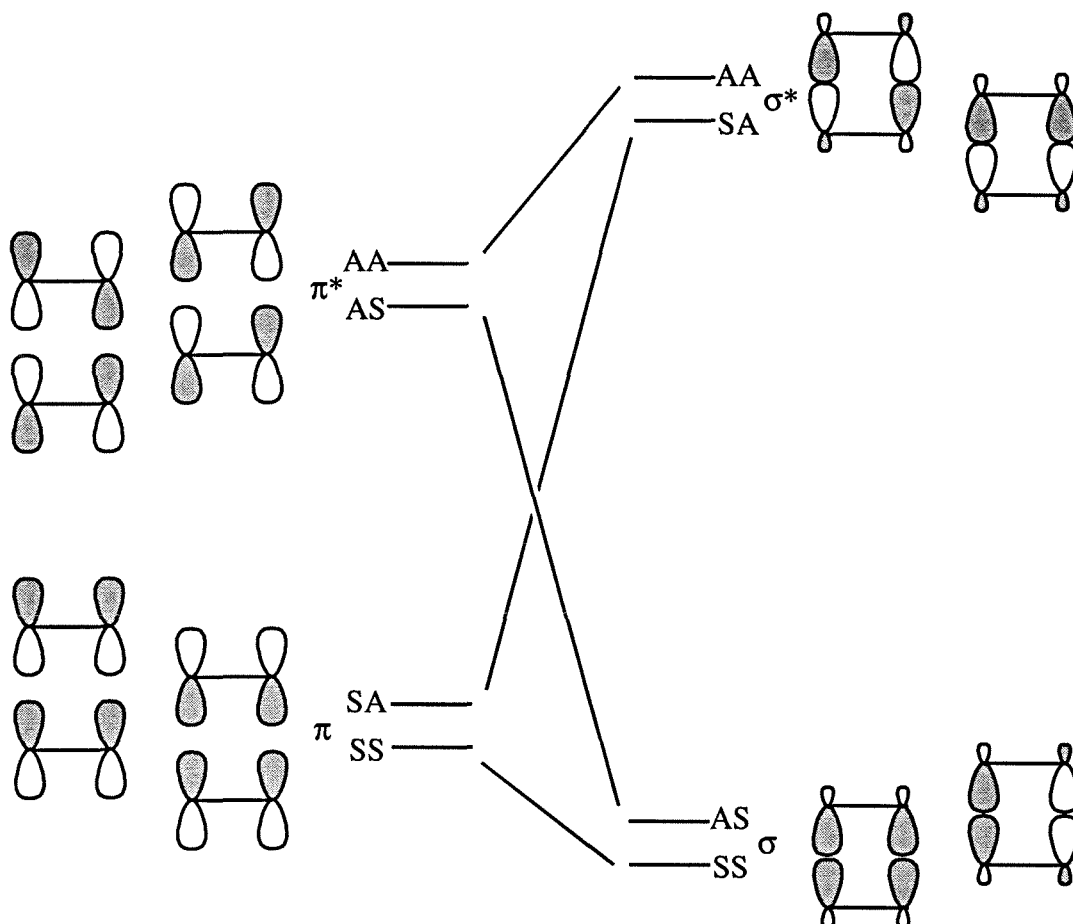
Figure 4.1 Correlation diagram for the formation of cyclobutanone from two molecules of ethylene (see Ref. 3). The correlation of a bonding reactant level with an antibonding product level implies that, if orbital symmetry is to be conserved, two ground-state ethylene molecules cannot combine in a concerted reaction to give ground-state cyclobutane — nor can cyclobutane decompose in a concerted fashion to yield two ethylene molecules.

Nonetheless, various experimental observations have been interpreted by this notion to establish the nature of tetramethylene as an intermediate species. By measuring competitive ratios, many groups have exploited the stereochemistry of tetramethylene to establish the "common diradical" hypothesis.[1,4-15] Studies of 1,2-dimethyl-tetramethylene generated by diazene,[1,6,8] cyclobutane,[14] or olefin[15]

precursors found the same ratio for $k_{rot}:k_{frag}:k_{cyc}$. The observation of identical ratios from three different precursors indicates the existence of a single diradical species common to all three modes of generation. Similar studies of deuterium-labeled tetramethylene[1,4,5,10,12] found that while the retention of stereochemistry depends on the precursor, the fragmentation/cyclization product ratio is independent of the method of generation.[16]

A number of model potential energy surfaces (PESs) were proposed to explain the observed behavior of tetramethylene. While further discussion of the qualitative and quantitative features of the PES is presented in Section IV, Fig. 4.2 shows three schemes for the reaction of cyclobutanone to ethylene, with representative potential energy curves drawn along the reaction coordinate. In (a), the reaction proceeds through a transition state at the saddle region of an activation barrier. The bonding transformation is characterized as a synchronous process, in which both bonds are broken (or formed) simultaneously. The other extreme, represented by (c), involves a two-step mechanism, beginning with the breakage of one σ-bond to produce tetramethylene as a diradical intermediate, which in turn passes through a transition state before yielding final products. Intermediate to these two schemes is a flat-topped potential energy curve, shown in (b). Here, the diradical can spend considerably more time (relative to scheme (a)) in the transition-region (termed "twixtyl") connecting reactants and products, a necessary consideration for explaining the observed stereomutation.

Recently, Marcus presented potential energy contour plots for this system,[17] offering a "bird's eye view" of the overall topography of the potential energy surface. Such a global plot allows depiction of multiple intermediates and transition states, making it perhaps more useful than a single 2-*d* cut of the multidimensional potential energy surface.
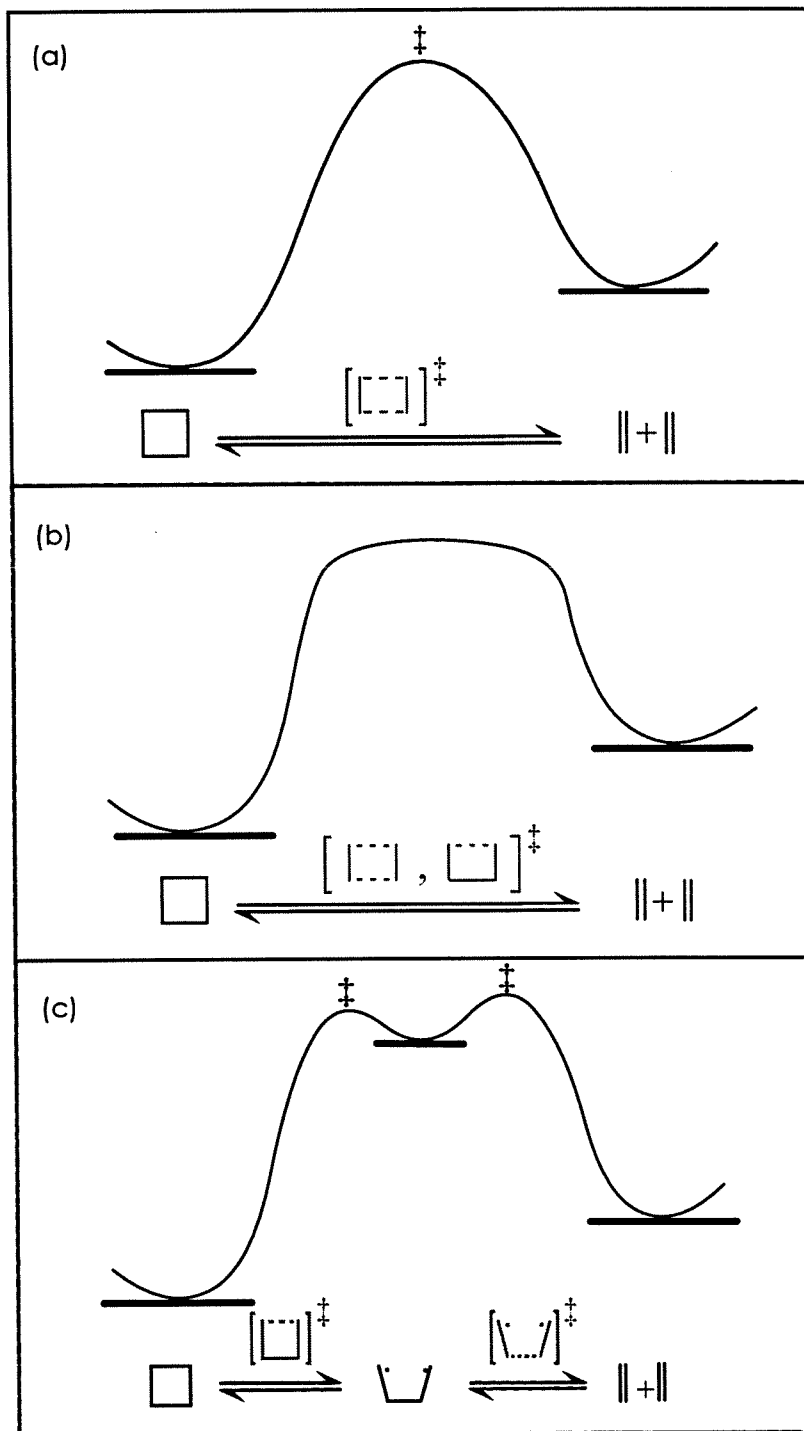
Figure 4.2 Model potential energy curves for describing dynamics of cyclobutanone/ethylene reaction. (a) Transition-state mechanism. (b) Twixtyl formation. (c) Diradical intermediate.

In the experiments presented here, singlet tetramethylene is observed directly for the first time. We use precursors (cyclopentanone and its derivatives) to generate the diradicals in a controlled manner. The subsequent dynamics of the tetramethylene decay to via closure and cleavage channels are studied via lifetime measurements and substitution experiments. To avoid collisional deactivation and other perturbations, the reaction is carried out in a skimmed molecular beam.

II.   Experimental

To observe the formation and evolution of the diradical species, we employed the combined techniques of femtosecond pump-probe spectroscopy and TOF mass spectrometry. The general methodology is described in Chapter 2, while specific features relevant to this experiment are detailed below.

Precursor Molecules

(i)   *(ii)*   *(iii)*   *(iv)*   *(v)*   *(vi)*
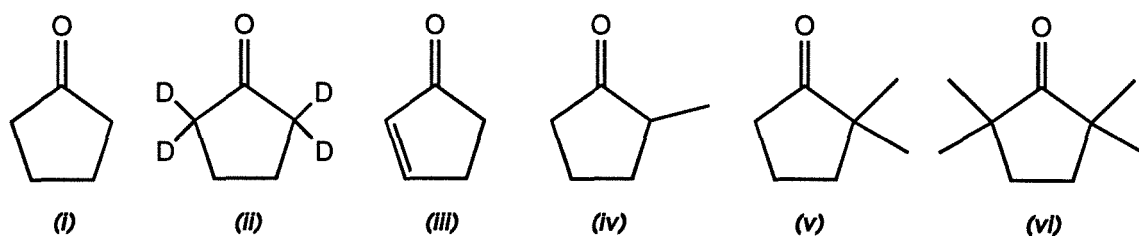
The 1,4-diradicals were produced via decarbonylation of the corresponding cyclic ketones (*vide infra*). Commercially obtained (Aldrich, 99.9%) cyclopentanone **(i)** was used without further purification. 2,2,5,5-d$_4$-cyclopentanone **(ii)** was prepared[18] from this material by repeated exchange with D$_2$O (acidic) and was

shown by NMR spectroscopy to be better than 92% exchanged in the 2 and 5 positions.

Other precursors employed, including 2-cyclopenten-1-one **(iii)**, 2-methyl-cyclopentanone **(iv)**, and 2,2-dimethyl-cylcopentanone **(v)** were also purchased (Aldrich) and used without further purification, as the mass selection in the TOF spectrometer allowed for discrimination against any impurities. Synthesis of 2,2,5,5-tetramethyl-cyclopentanone **(vi)** was performed by K. Anderson (Caltech).[18] Purities of all synthesized compounds were confirmed by NMR and IR spectroscopy.

Helium carrier gas flowing over the sample surface transported the precursors through the pulsed nozzle (orifice diameter = 0.3 mm) and to the interaction region. The backing pressure was maintained at approximately 20 psi and the background pressure in the TOF chamber was maintained at 1×10^{-6} torr when the nozzle was open.

III. Results

Figure 4.3 (bottom) presents TOF mass spectra of the cyclopentanone system. Here, the pump wavelength was tuned to 310 nm and the probe laser (620 nm) was set at a delay of ~100 fs. Fragmentation species at masses lower than the precursors indicate dissociation dynamics which may be further probed as a function of time delay. In particular, the mass peak appearing at the flight time corresponding to the precursor species (m/e = 84) minus the carbonyl fragment is the expected diradical signal (m/e = 56).
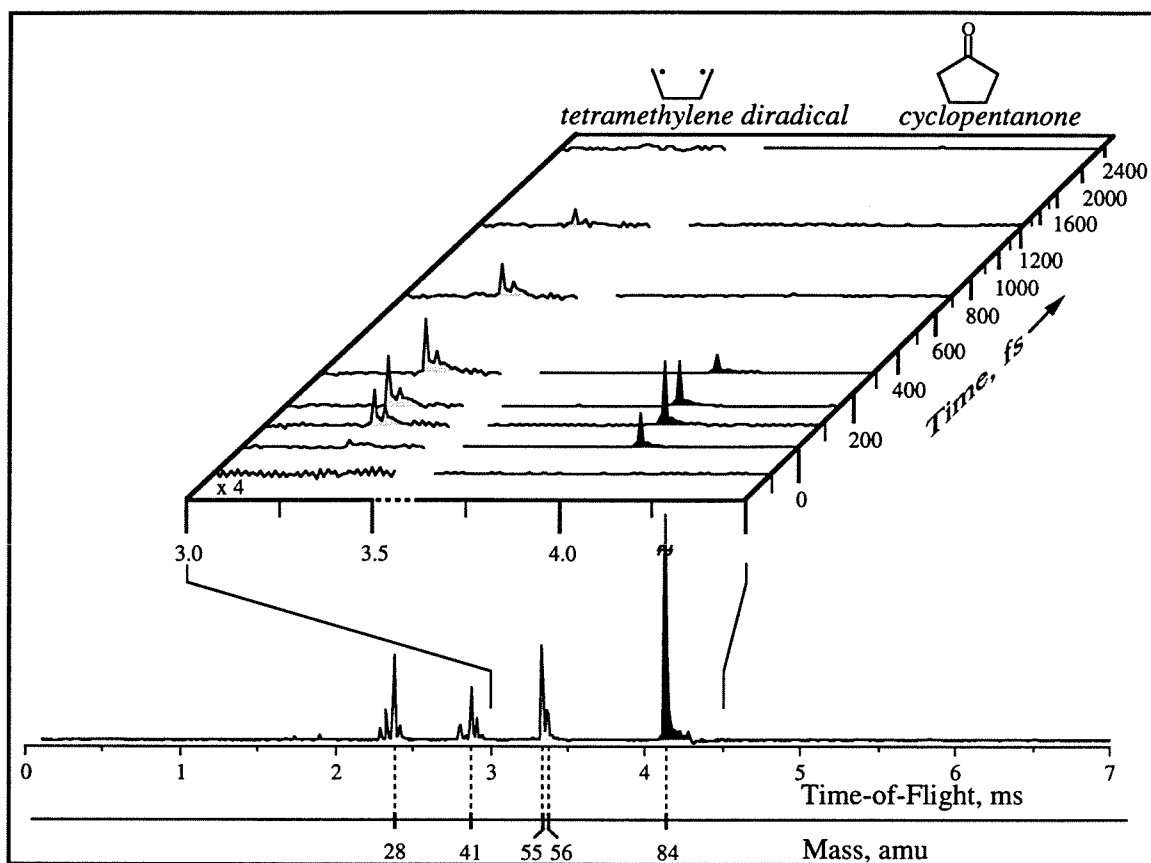
Figure 4.3 Mass spectra obtained for different femtosecond time delays between the pump and probe laser pulses. The cyclopentanone precursor (84 amu) signal appears at zero time delay and subsequently decays. In contrast, the tetramethylene diradical intermediate (56 amu) appears later, growing in and peaking at ~300 fs, then decaying with a time constant of ~700 fs (see text). The masses at 28 and 41 are due to ionic fragmentation channels in the precursor decay (see text).

The panel at the top of Fig. 4.3 shows the cyclopentanone mass spectra recorded at different time delays, in which the evolution of the fragment species with time begins to be apparent. At negative times, *i.e.* when the probe pulse arrives before the pump, there is no signal. At time zero, the precursor signal at 84 amu is observed, while signal at the fragment mass corresponding to the

decarbonylated precursor (m/e = 56) is not yet present. As the time delay increases,

we observe the prompt decrease in the precursor signal and the rise of the fragment

signal at mass 56 (or 55, corresponding to the species of interest minus one

hydrogen). This signal peaks at about 300 fs, then decreases back to the baseline.

Other cyclic ketone systems were studied similarly, including deuterium- and

methyl-substituted cyclopentanone and 2-cyclopenten-1-one.
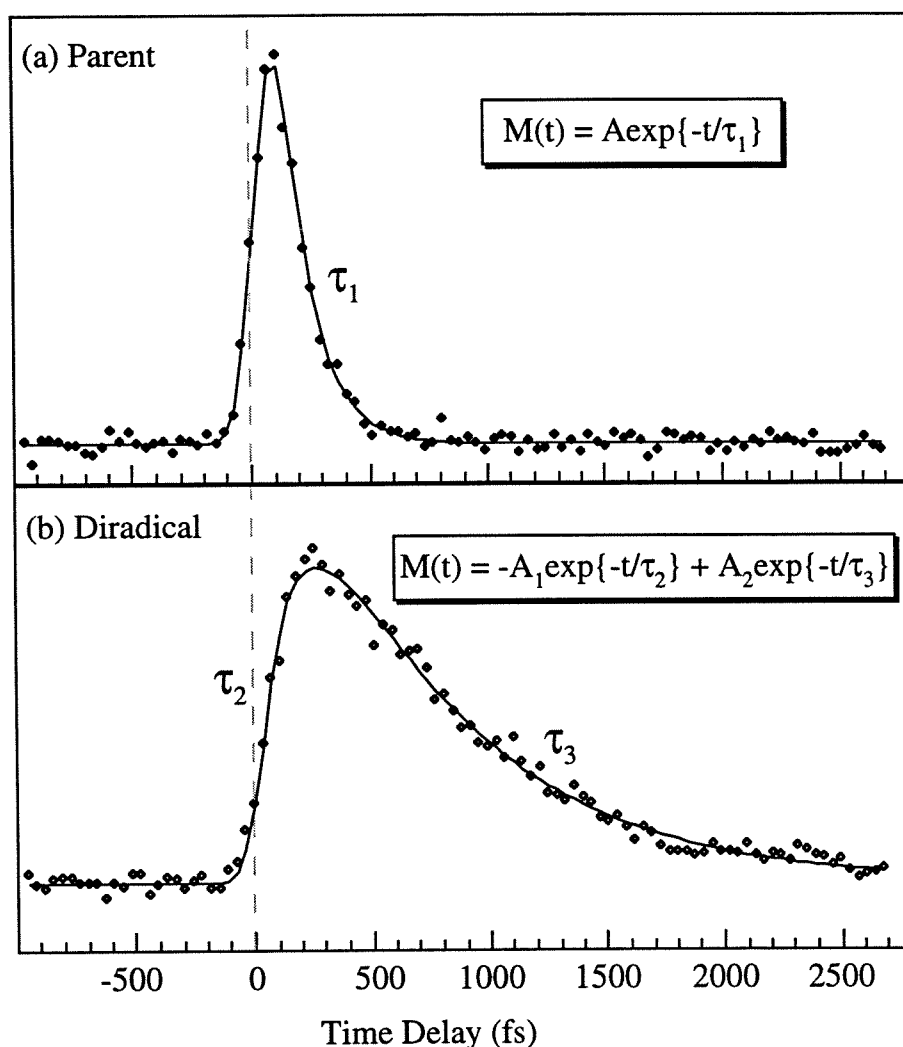

Figure 4.4 Femtosecond transients showing the detected ion signal as a function of pump-probe delay. The cyclopentanone precursor signal (84 amu) simply decreases with an exponential decay time τ_1 of 120 ± 20 fs. The diradical exhibits a biexponential behavior, building up to a maximum (τ_2 = 150 ± 30 fs) followed by a relatively slow decay (τ_3 = 700 ± 40 fs).

Femtosecond transients on the precursor and fragment species reveal the dynamics of the dissociation; see Fig. 4.4. First, the precursor signal is observed to grow in according to the instrument response function (Gaussian cross-correlation of the pump and probe pulses, fwhm = 120–200 fs). The signal decay is fitted by a single exponential function convoluted with a Gaussian to obtain the time constant τ_1 for the precursor decay, see Fig. 4.4a. Power dependence studies on the pump laser intensity indicate that the initial excitation occurs via absorption of two UV photons by way of a resonant intermediate level. The measured power dependence was ~1.4 for all precursors studied.

To monitor the diradical dynamics, the delay of the boxcar gate was set to the mass peak corresponding to the precursor species minus the carbon monoxide fragment. The signal here (56 amu for the cyclopentanone/tetramethylene system) is observed to build up with a time constant τ_2 and subsequently decay with a time constant τ_3; see Fig. 4.4b. The diradical transients were fitted to a biexponential function with one component in the rise and one in the decay. Again, convolution with a Gaussian cross-correlation function was included, this time using the same fwhm and time-zero shift as was extracted from fitting the corresponding parent transient.
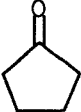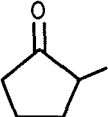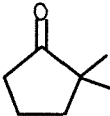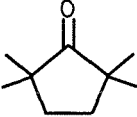
The shape of the femtosecond transient at the mass peak corresponding to the decarbonylated precursor is a clear indication that the species probed is indeed the diradical. While the mass of the diradical could also correspond to a final product (*i.e.* $mass_{tetramethylene} = mass_{cyclobutane} = 56$ amu), the observed dynamics are not consistent with detection of such a species. The signal is shown to grow exponentially, the onset being essentially the same as that of the parent decay. The ion signal then peaks at a time delay of approximately 200 fs for tetramethylene before descending exponentially back down to zero. Following this decay, no further signal is observed for time scales of up to 30 ps (the maximum pump/probe delay in

these experiments). In contrast, the ion signal of a final product is expected to persist at long times. The observed signal is thus assigned to originate from the diradical intermediate formed upon decarbonylation of the excited precursor.
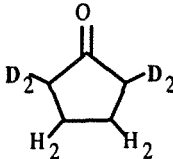
It should be noted that such behavior was observed only with sufficient attenuation of the probe laser. With an intense probe, multiphoton absorption could induce fragmentation of the parent ion, creating an additional time-dependent signal in the fragment transient that was identical (both in shape and temporal delay) to that of the parent. The additive effect of the this parent-ion component with the diradical signal obscured the rising edge unless careful measures were taken to attenuate the probe. In some cases, it was not possible to fully remove this contrib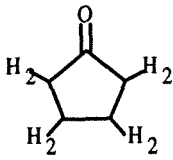ution from the diradical signal, requiring us to modify our fitting procedure to include addition of a signal component given by the fit of the parent transient (with variable amplitude only).

Furthermore, transients recorded for all other fragment masses lighter than the diradical were observed to be identical to that of the parent, with no delayed component(s) seen on our time scale ($t_{delay} < 30$ ps). Such behavior suggests that the parent ion (generated by a 2 + 1 REMPI process) undergoes direct dissociation by absorption of additional probe photons to produce these low-mass species. They are not, therefore, intermediate or product species formed along the same or parallel dissociation channels on which the diradical evolves (*vide infra*).
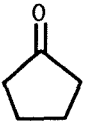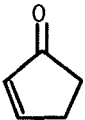
The simplest 1,4-diradical, tetramethylene, is produced by decarbonylation of cyclopentanone. As shown in Fig. 4.4, the signal evolves with time constants $\tau_2 = 150 \pm 30$ fs and $\tau_3 = 700 \pm 40$ fs upon excitation at $\lambda_{pump} = 310$ nm. The effects of excitation energy, deuterium isotope exchange, methyl substitution, and bond strength are illustrated by comparison with this prototype system.

Table 4.1 Substitution Effect

	τ_1, fs	τ_2, fs	τ_3, fs
(cyclopentanone)	120 ± 20	150 ± 30	700 ± 40
(2-methylcyclopentanone)	200 ± 20	90 ± 30	700 ± 100
(2,2-dimethylcyclopentanone)	305 ± 30	125 ± 30	740 ± 100
(2,2,5,5-tetramethylcyclopentanone)	470 ± 100	900 ± 200	1400 ± 200

Methyl Substitution. The effect of methylating the α-positions of cyclopentanone was studied in a series of four compounds; see Table 4.1. The time constant for formation of the diradical (τ_2) is observed to depend strongly on the extent of methylation: from 150 ± 30 fs for unsubstituted tetramethylene to 0.9 ± 0.2 ps for the tetramethyl derivative (1,1,4,4-tetramethyl-tetramethylene). In contrast, the decay of the transient signal for the diradical (τ_3), is not significantly affected until both terminal carbon positions are methylated. The time constant is approximately 700 fs for unsubstituted tetramethylene, 1-methyl- tetramethylene, and 1,1-dimethyl- tetramethylene; for 1,1,4,4-tetramethyl- tetramethylene, however, the lifetime increases by a factor of two to 1.4 ± 0.2 ps.

Table 4.2 Deuterium Isotope Effect			
	τ_1, fs	τ_2, fs	τ_3, fs
(structure: 2,2,5,5-H4 cyclopentanone)	120 ± 20	150 ± 30	700 ± 40
(structure: 2,2,5,5-D4 cyclopentanone)	220 ± 30	230 ± 70	1100 ± 200

Deuterium Isotope Effect. Replacing the hydrogen atoms located on the α-carbons of the cyclopentanone precursor with deuterium yielded 2,2,5,5-d_4-cyclopentanone. This species was well-separated from the unsubstituted cyclopentanone in the TOF spectrometer, allowing unambiguous detection of the precursor or diradical species. The measured time constants are summarized in Table 4.2, where each of the three time constants is shown to be approximately 1.6 times greater for deuterated cyclopentanone than for the hydrogenated isotope.

Table 4.3 Bond Strength Effect			
	τ_1, fs	τ_2, fs	τ_3, fs
(structure: cyclopentanone)	120 ± 20	150 ± 30	700 ± 40
(structure: cyclopentenone)	120 ± 20	150 ± 40	200 ± 100

Bond Strength Effect. If we compare the dynamics associated with the saturated ring compound cyclopentanone with those for 2-cyclopenten-1-one, we see a substantial reduction in τ_3. As presented in Table 4.3, the time constants τ_1 and τ_2 for the decay of the precursor and the formation of the diradical, respectively, are identical. The decay of the intermediate signal, however, is nearly four times faster for the diradical species originating from the double-bonded ring compound than for tetramethylene.

Table 4.4 Pump Energy Dependence.

Pump Wavelength (nm)	τ_1, fs	τ_2, fs	τ_3, fs
280	120 ± 20	100 ± 30	340 ± 30
310	120 ± 20	150 ± 30	700 ± 40
320	120 ± 20	240 ± 30	840 ± 50

Excitation Energy. Finally, the effect of excitation energy on the diradical dynamics was explored by variation of the pump laser wavelength. The pump wavelength was tuned from 320 to 280 nm, corresponding to 2-photon excitation energies of 180 to 205 kcal/mol. The results are reported in Table 4.4 for the cyclopentanone/tetramethylene system.

In the following section, these observations will be correlated to aspects of the mechanism and potential energy surfaces on which the dynamics occur.

IV. Discussion

Potential Energy Surface

The dynamics of the diradical intermediate are governed by the nature of the potential energy surface along the reaction coordinate. Despite the substantial excess energy partitioned to the tetramethylene intermediate (*vide infra*), subtle details of the potential shape (*i.e.* barriers, avoided crossings, etc.) can significantly affect the course of the reaction. The shape of the potential energy surface has been the subject of a lengthy debate drawn over various experimental and theoretical findings.

The potential energy surface for tetramethylene can be described by both thermodynamic and quantum mechanical approaches. The pyrolysis of cyclobutane follows first order kinetics with an activation energy of 62.5 kcal/mol (Ref. 19). From a simple thermodynamics cycle (see Scheme 1), tetramethylene can be shown to be a stable species.

Scheme 1:
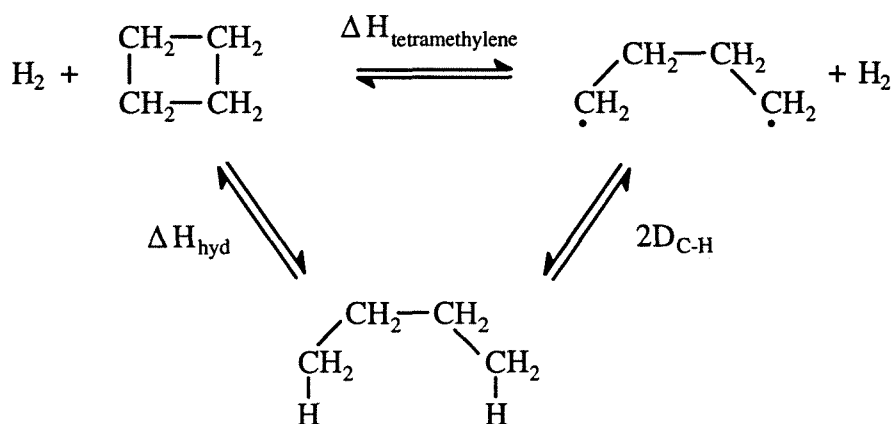
The energy to form tetramethylene via ring opening, $\Delta H_{tetramethylene}$, must be equal to the energy required to first hydrogenate cyclobutane to butane (ΔH_{hyd}) and then remove two hydrogen atoms from the terminal carbons of butane:

$$\Delta H_{tetramethylene} = \Delta H_{hyd} + 2D_{C\square H} - D(H_2)$$
$$= (\Delta H_{butane} - \Delta H_{cyclobutane}) + 2D_{C\square H} - D(H_2)$$

Assuming that the terminal C–H bond strengths in butane and the butyl monoradical are identical, Benson calculated $\Delta H_{tetramethylene} = 56$ kcal/mol (Ref. 20,21), *i.e.* the barrier to ring closure is 6.5 kcal/mol. A similar cycle involving the cleavage of tetramethylene to two ethylenes predicts a barrier of approximately 4 kcal/mol. Recent revisions to the heats of formation of relevant species has lowered these barriers somewhat,[13] nonetheless a stable intermediate is predicted according to simple thermodynamics. The validity of the critical assumption in this analysis, namely that the two internal methylene groups provide sufficient insulation from cooperative effects between the terminal (radical) carbons, is difficult to ascertain. A difference in bond strength of only 5 % in D_{C-H} for the terminal bonds in butane and butyl could effectively eliminate any thermodynamic stability.

The first potential energy surface for the pyrolysis of cyclobutane was determined by Hoffmann and coworkers using extended Hückel theory.[22] Their calculations suggest that between the reactant and product wells of reaction **1**, there exists a large flat region of the potential energy surface upon which the molecules could spend relatively long times ($>10^{-12}$ s) exploring. Operationally, this region, termed "twixtyl" is thought to be indistinguishable from a true minimum. Further consideration of trajectory behavior on such a potential surface is necessary (*vide infra*).

The stability absent in the extended Hückel calculations was again borne out in the initial *ab initio* quantum mechanical calculations by Segal.[23] This seminal work, considering 30 vibrational degrees of freedom, found local minima for both gauche and trans conformers on the singlet tetramethylene potential energy surface. The barrier heights for both species were in the range of 2–4 kcal/mol for closure and cleavage reactions.

Subsequent quantum mechanical calculations by Doubleday[16] and Bernardi *et al.*[24] have found that the minima are lost when corrections for zero-point energy and basis set errors are considered. Hence, the most recent theoretical description of the reaction surface does not contain a potential energy minimum. How, then, can we understand the experimentally observed loss of stereochemistry, or, more relevant to this work, the dynamic behavior observed in direct studies?

The answers may lie in the free energy surface. Employing canonical variational theory[25] to calculate the free energy surface for the tetramethylene system, Doubleday has found that both *gauche* and *trans* tetramethylene conformers exist due to entropy effects.[16] The diradical is protected from cyclization and fragmentation by a rapid decrease in entropy upon product formation corresponding to tightening of the loose modes (in particular, the terminal methylene wagging and internal rotation). As ΔS decreases, a temperature dependent free-energy barrier may be formed ($\Delta G = \Delta H - T\Delta S$).

Reactivity and Mechanism

The fact that the time constants for the decay of the precursor and the formation of the diradical are *not the same* suggests that the decarbonylation occurs in a stepwise process. That is, the excited precursor (**1**) undergoes rapid a-cleavage to form the acyl-alkyl diradical (**2**) which subsequently fragments to release the carbon monoxide and produce the 1,4-diradical (**3**). The associated time constants
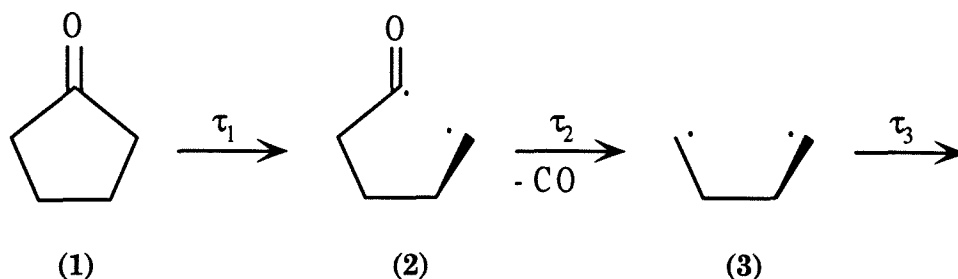
are: τ_1, primary (Norrish-type) α-cleavage; τ_2, secondary cleavage to generate the diradical; and τ_3, the diradical lifetime. The dynamics and mechanism related to each of these processes is discussed in detail below.

Primary C–C Cleavage

The cyclopentanone precursor dissociates on a femtosecond time scale upon excitation to the Rydberg region, orders of magnitude faster than decay from S_1 (n,π^*).[26] This prompt dissociation is mediated by efficient coupling to dissociative valence states (σ_{C-C}^*) in the same energy region. According to the observed power dependence, two pump photons are absorbed by the precursor. For $\lambda_{pump} = 310$ nm, this equals 184 kcal/mol, corresponding to Rydberg-level excitation (see Fig. 4.5). The absorption spectra in the VUV region around 160-140 nm show a series of Rydberg states as well as a broad background feature.[27] The broad spectral width of the Rydberg states at around 150 nm (*i.e.* near our excitation energy) indicates a strong coupling of those Rydberg states to a dissociative valence state. The spectroscopic assignment of the valence state is uncertain. From consideration of the molecular orbital state correlation diagram, however, the valence state should have an antibonding character along the C–C bond to allow for prompt cleavage.[28,29]
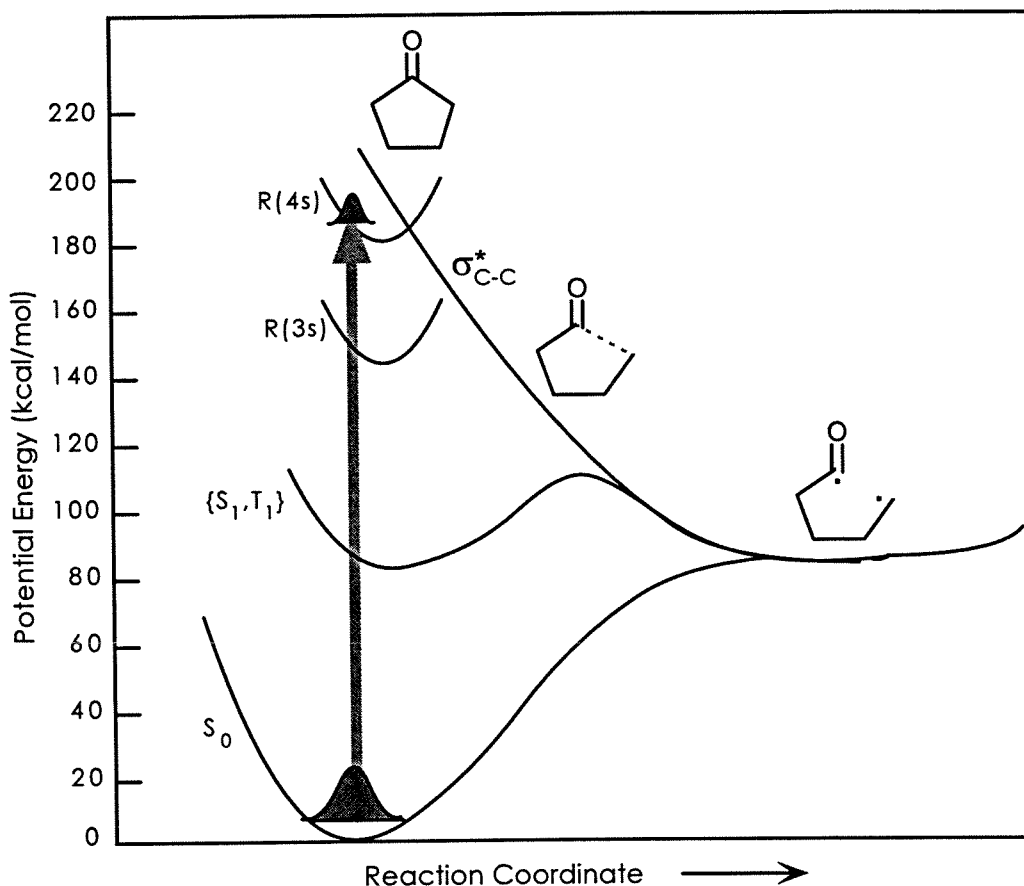
Figure 4.5 A cut of the potential energy surface along the reaction coordinate for the Norrish type-I α-cleavage of cyclopentanone following excitation by the femtosecond pump pulse. States are labeled with R denoting Rydberg, S singlet and T triplet, and S_0 the ground state. Energies are taken from Refs. 27,30-32.

Cyclopentanone dissociates with a time constant of $\tau_1 \sim 120$ fs. Methyl substitution on the ring slows down the bond dissociation dynamics, giving an interesting trend in the time constant with increasing number of methyl substitutions. This trend is consistent with predictions from statistical reaction rate theory; the higher the density of reactant states, the smaller the rate constant.

The rate constant can be expressed by the Ramsperger-Rice-Kassel (RRK) theory,

$$k(E) = \nu\left[\frac{E - E_0}{E}\right]^{(s-1)}$$ (2)

where ν is the vibrational frequency along the reaction coordinate, E is the total energy, E_0 is the reaction barrier, and s is the number of vibrational degrees of freedom. Taking the logarithm of both sides of Eq. (2), the expression becomes

$$\log k = \log \nu + (s-1)\log\left[\frac{E - E_0}{E}\right],$$ (3)

indicating that log k is linearly proportional to (s-1) when ν, E, and E_0 remain constant. For the methylated cyclopentanone series, the C–C frequency and energetics involved in the a-cleavage are expected to be approximately the same. The only significant difference here is the increase of the number density of the precursor with the increasing number of methyl groups. In Fig. 4.6, log k *vs.* (s-1) is plotted for the methylated cyclopentanone series, starting from bare cyclopentanone and continuing up through 2,2,5,5-tetramethyl-cyclopentanone. The data fit well to straight line. The least-squares fit yields an intercept of log ν = 13.5, corresponding to $\nu \sim$ 34 fs. The slope log $[(E - E_0)/E]$ = –0.017, suggesting that the reaction barrier E_0 is approximately 4% of the available energy E. This indicates that the primary cleavage occurs on a potential energy surface which is almost purely repulsive in nature. The measured dissociation time constant (120 – 500 fs) is likely too short for *complete* IVR to occur. Thus the statistical behavior observed here likely does not result from fundamental tenets of statistical reaction rate theory. Rather, it may originate from the dynamical motion of a wave packet on the PES, analogous to previous observations in the Rydberg-state dissociation of methyl iodide.[33,34]
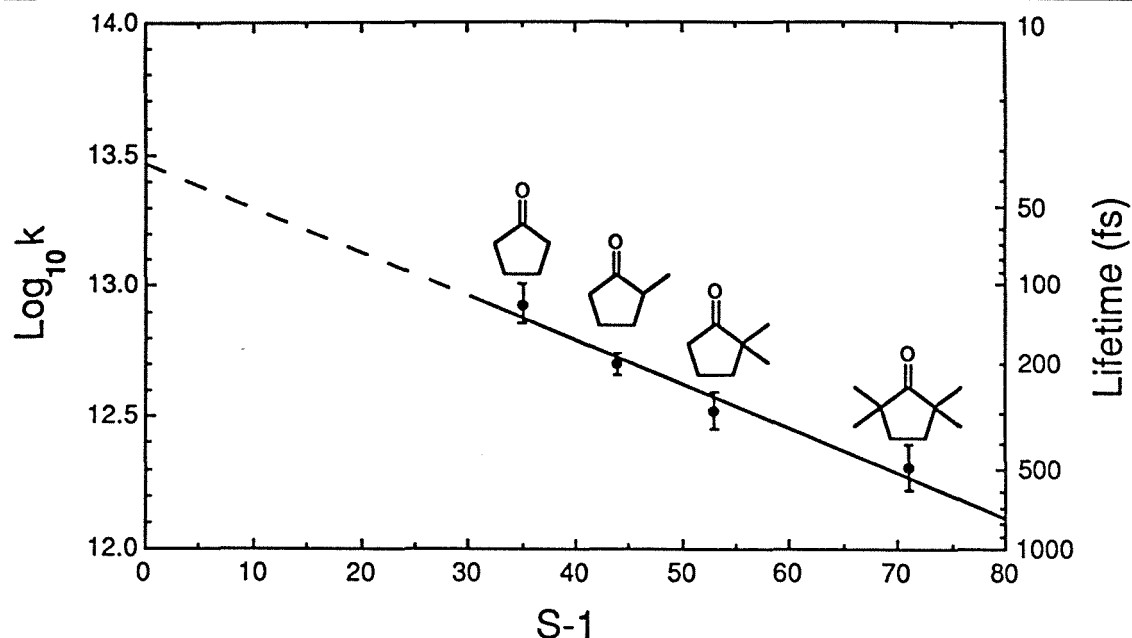
Figure 4.6 Primary cleavage time constants τ_1 *vs.* vibrational degrees of freedom (minus one). The linear fit yields a slope of -0.017 and intercept of 13.5 (see text for interpretation).

Secondary Cleavage: Stepwise or Concerted Formation of Diradical

The observation of two different time constants for the decay of the precursor and the subsequent build-up of the tetramethylene diradical is significant. In general, two channels may be described for tetramethylene formation. A concerted mechanism, in which both C–C bonds adjacent to the carbonyl moiety are stretched simultaneously to the breaking point, is represented by the diagonal in Fig. 4.7. This process involves coherent nuclear motion and launches a wave packet onto the tetramethylene potential energy surface. In contrast, a step-wise mechanism will involve little correlation between the two C–C bonds. The primary bond cleavage will produce an acyl-alkyl diradical which will subsequently decay be releasing the CO to yield tetramethylene.

In cyclopentanone, the primary cleavage occurs in ~120 fs and the diradical formation in ~150 fs, consistent with a step-wise dissociation mechanism. This trend is reproduced in the deuterated system as well as the unsaturated precursor species.
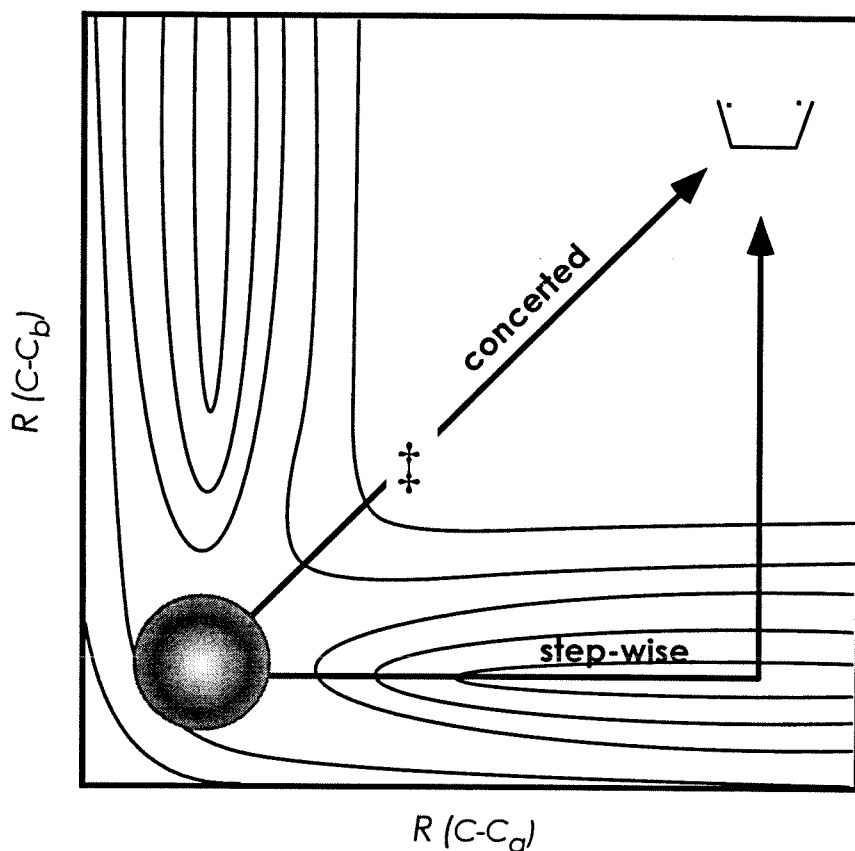
Figure 4.7 Concerted and stepwise dissociation pathways, shown on schematic 2-*d* cut of potential energy surface for cyclopentanone precursor.

From the measured product distributions for the photolysis of cyclobutanone[35] and of 3-cyclopentenone,[36] the amount of energy that will be partitioned to the tetramethylene can be estimated. Two pump photons at 310 nm correspond to a total excitation energy of 184 kcal/mol. The available energy is hence equal to this amount minus the two bond energies involved in the decarbonylation, yielding approximately 99 kcal/mol. The total translational energy plus the internal energy in the ejected CO accounts for ~17 kcal/mol,[35,36] leaving E ~ 82 kcal/mol to internal energy in the diradical. For λ_{pump} = 320 nm, E ~ 77 kcal/mol; for λ_{pump} = 280 nm, E ~ 100 kcal/mol.

Diradical Lifetime

The intrinsic lifetimes of the tetramethylene diradicals correspond to the measured time constants τ_3. From the data reported above, the tetramethylene and methyl-substituted tetramethylene diradicals are observed to be substantially different. Moreover, in tetramethylene, as the total energy is increased from 77 to 82 to 100 kcal/mol, τ_3 decreased from 840 to 700 and then to 340 fs, respectively. Considering the dynamics of the nuclei at the top of a barrier, it is impossible at these energies to obtain such time scales if a wave packet is moving translationally on a flat surface. For example, over a distance of 0.5 A, the time in the transition-state region will be ~40 fs. To explain the observed (sub)picosecond times, other nuclear degrees of freedom must be involved.

The diradical in a "basin" defines a multidimensional PES with the involvement of many degrees of freedom. At the energies of interest, the total energy E available to the diradical is significantly greater than the barrier height (E_0). Using the measured energy dependent rate constants ($1/\tau_3$), the barrier height can be calculated by another application of RRK theory [Eq. (2)]. Taking the frequency of the reaction coordinate[16] to be 150 cm^{-1} (1/220 fs), the barrier height is found to be ~4 kcal/mol.

Recently, Doubleday employed variational RRKM to predict the lifetime of tetramethylene in the same energy range.[37] The calculated lifetimes included contributions from fragmentation channels for both the *gauche* and *trans* conformers, and cyclization from the *gauche* tetramethylene only. Overall, the predicted values are within or slightly below the range reported here, see Table 5. The observed trend in lifetime as a function of excess energy, however, was not reproduced,[37] suggesting a strong non-RRKM behavior. The initial nonstatistical distribution of vibrational energy associated with the femtosecond pulses may

isolate some regions of the overall phase space from the reaction coordinate. Further studies considering restricted IVR in this system are necessary.

Table 4.5 Experimental vs. calculated values for τ_3.

Energy kcal/mol	τ_3, exp fs	τ_3, calc[a] fs
77	840 ± 50	475
82	700 ± 40	468
100	340 ± 30	444

[a]Based on the assumption that *gauche* and *trans* conformers are initially populated statistically. In a separate calculation, the *gauche* and *trans* conformers are treated independently (see Ref. 37).

Additional support for the intermediacy of the tetramethylene diradical comes from the observed substitution effect on the overall dynamics. When methyl substituents are added to the α-carbons on the cyclopentanone precursor, the lifetime of the diradical increases from the subpicosecond to the picosecond regime. The extra stability of the diradical is the result of delocalization of the electron density and possible steric repulsion due to the nearby alkyl groups. Studies of such effects in these systems goes back to the 1961 work by Gerberich and Walters on the thermal decomposition of methyl-substituted cyclobutanes.[14] Finally, the results have a direct impact on product-channel distributions. With methyl substitution, the internal rotation slows down with respect to fragmentation,[1,38,39] thus altering the stereospecificity.

V. Conclusions

A new level of understanding has been reached in diradical chemistry, in which mechanistic hypotheses may be validated by direct observation of fleeting

intermediate and transition-state species. This chapter presents femtosecond studies of tetramethylene and related 1,4-diradicals formed by decarbonylation of cyclic ketones via Rydberg-level excitation. Time-of-flight mass spectrometry detection isolated the reactive intermediate species, and femtosecond pump-probe spectroscopy provided the lifetime. The observations establish the diradical as a distinct molecular species along the reaction coordinate joining cyclobutane and ethylene. The lifetime of tetramethylene is strongly affected by changes in excess energy and substituents. The observations are correlated to a description of tetramethylene in a multi-dimensional basin.

Future studies of tetramethylene and related 1,4-diradicals will be important to discerning subtle features of the PES. Preparation via other precursors will sample other regions of the tetramethylene well, and may provide direct evidence for the "common diradical" hypothesis. Femtosecond polarization spectroscopy (see Ref. 40) will allow detection of the internal rotation rates of tetramethylene, bridging the gap between direct measurements and stereomutation studies.

References

[1] P. B. Dervan and D. A. Dougherty, in *Diradicals*, edited by W. T. Borden (Wiley, New York, 1982), p. 107.

[2] S. Pedersen, J. L. Herek, and A. H. Zewail, Science **266,** 1359 (1994).

[3] R. B. Woodward and R. Hoffmann, *The Conservation of Orbital Symmetry* (Verlag Chemie, Deerfield Beach, 1970).

[4] P. B. Dervan and D. S. Santilli, J. Am. Chem. Soc. **102,** 3863 (1980).

[5] D. S. Santilli and P. B. Dervan, J. Am. Chem. Soc. **101,** 3663 (1979).

[6] P. Dervan and T. Uyehara, J. Am. Chem. Soc. **98,** 1262 (1976).

[7] P. B. Dervan, T. Uyehara, and D. S. Santilli, J. Am. Chem. Soc. **101,** 2069 (1979).

[8] P. Dervan and T. Uyehara, J. Am. Chem. Soc. **101,** 2076 (1979).

[9] P. Schultz and P. Dervan, J. Am. Chem. Soc. **104,** 6660 (1982).

[10] M. Goldstein, M. Cannarsa, T. Kinoshita, and R. Koniz, Stud. Org. Chem. (Amsterdam) **31,** 121 (1987).

[11] D. Lewis, D. Glenar, B. Kalra, J. Baldwin, and S. Cianciosi, J. Am. Chem. Soc. **109,** 7225 (1987).

[12] J. Chickos, A. Annamalai, and T. Keiderling, J. Am. Chem. Soc. **108,** 4398 (1986).

[13] W. von E. Doering, Proc. Natl. Acad. Sci. U.S.A. **78,** 5279 (1981).

[14] H. Gerberich and W. Walters, J. Am. Chem. Soc. **83,** 3935,4884 (1961).

[15] G. Scacchi, C. Richard, and M. Back, Int. J. Chem. Kinetics **9,** 513 (1977).

[16] C. Doubleday, J. Am. Chem. Soc. **115,** 11968 (1993).

[17] R. A. Marcus, J. Am. Chem. Soc. **117,** 4683 (1995).

[18] Synthesis performed by K. K. Anderson, California Institute of Technology.

[19] F. Kern and W. D. Walters, J. Am. Chem. Soc. **75,** 6196 (1953).

[20] S. W. Benson, J. Chem. Phys. **34,** 521 (1961).

[21] S. W. Benson, J. Chem. Phys. **46,** 4920 (1967).

[22] R. Hoffmann, S. Swaminathan, B. G. Odell, and R. Gleiter, J. Am. Chem. Soc. **92,** 7091 (1970).

[23] G. A. Segal, J. Am. Chem. Soc. **96,** 7892 (1974).

[24] F. Bernardi, A. Bottoni, P. Celani, M. Olivucci, M. A. Robb, and A. Venturini, Chem. Phys. Lett. **192,** 229 (1992).

[25] D. Truhlar, A. Isaacson, and B. Garrett, in *Theory of Chemical Reaction Dynamics*, Vol. IV, edited by M. Baer (CRC Press, Boca Raton, 1985), p. 65.

[26] R. G. Shortridge, C. R. Rusbult, and E. K. C. Lee, J. Am. Chem. Soc. **93,** 1863 (1971).

[27] L. O'Toole, P. Brint, C. Kosmidis, G. Boulakis, and P. Tsekeris, J. Chem. Soc. Faraday Trans. **87,** 3343 (1991).

[28] N. J. Turro, *Modern Molecular Photochemistry* (University Science Books, Mill Valley, 1991).

[29] J. Michl and V. Bonacic-Koutecky, *Electronic Aspects of Organic Photochemistry* (Wiley, New York, 1990).

[30] T. J. Cornish and T. Baer, J. Am. Chem. Soc. **109,** 6915 (1987).

[31] J. Zhang, W. Y. Chiang, P. Sagaer, and J. Laane, Chem. Phys. Lett. **196,** 573 (1992).

[32] M. Baba and I. Hanazaki, J. Chem. Phys. **81,** 5426 (1984).

[33] M. H. M. Janssen, M. Dantus, H. Guo, and A. H. Zewail, Chem. Phys. Lett. **214,** 281 (1993).

[34] H. Guo and A. H. Zewail, Can. J. Chem. **72,** 947 (1994).

[35] K. A. Trentelman, D. B. Moss, S. H. Kable, and P. L. Houston, J. Phys. Chem. **94,** 3031 (1990).

[36] R. Jimenez, S. H. Kable, J. C. Loison, C. J. S. M. Simpson, and P. L. Houston, J. Phys. Chem. **96,** 4188 (1992).

[37] C. Doubleday, Chem. Phys. Lett. **233,** 509 (1995).

[38] J. A. Berson, L. D. Pederson, and B. K. Carpenter, J. Am. Chem. Soc. **98**, 122 (1976).

[39] J. A. Berson, in *Rearrangements in Ground and Excited States*, Vol. 1, edited by P. de Mayo (Academic Press, New York, 1980), p. 311.

[40] A. H. Zewail, *Femtochemistry: Ultrafast Dynamics of the Chemical Bond* (World Scientific, Singapore, 1994), Vol. 1 & 2.

5. Methyl Salicylate*

The real-time dynamics of hydrogen atom-transfer processes under *collisionless* conditions are studied using femtosecond depletion techniques. The experiments focus on the methyl salicylate system, which exhibits ultrafast hydrogen motion between two oxygen atoms due to molecular tautomerization, loosely referred to as intramolecular "proton" transfer. To test for tunneling and mass effects on the excited potential surface, we also studied deuterium and methyl-group substitutions. The motion of the hydrogen, under collisionless conditions, takes place within 60 fs. At longer times, on the picosecond time scale, the hydrogen-transferred form decays with a threshold of 15.5 kJ/mol; this decay behavior was observed up to a total vibrational energy of ~7200 cm^{-1}. The observed dynamics provide the global nature of the motion, which takes into account bonding before and after the motion, and the evolution of the wave packet from the initial nonequilibrium state to the transferred form along the O–H···O reaction coordinate. The vibrational periods ($2\pi/\omega$) of the relevant modes range from 13 fs (the OH stretch) to 190 fs (the low-frequency distortion), and the motion involves (in part) these coordinates. The IVR dynamics at longer times are important to the hydrogen-bond dissociation and to the nonradiative decay of the hydrogen-transferred form.

I. Introduction

Usually, bond-breaking and bond-forming dynamics involve the redistribution of electrons between "old" and "new" bonds or the transfer of an electron (harpooning reaction) when the nuclei are in an appropriate configuration. In a whole class of reactions, loosely called proton-transfer reactions, the key to the breaking or making of bonds is hydrogen atom (H) motion or proton (H^+) transfer dynamics, which also occur on the picosecond to femtosecond time scale.

The generic description of these "proton transfer" reactions normally involves a reaction coordinate of the type

$$O_a\text{–}H \cdots O_b \, , \tag{1}$$

where the light hydrogen nucleus is between two heavy oxygen atoms. With H moving (or transferring) between O_a and O_b, the O_a–H bond is broken and a new one (H–O_b) is formed. This elementary description, which may involve neutral H motion or zwitterion (H^+O^-) formation, is abundant in organic photochemistry and proton-transfer spectroscopy.[1]

Even under collisionless conditions, however, the motion may not be that simple. The motion of hydrogen on the pico- or femtosecond time scale may be localized [as in Eq. (1)], or may involve nuclear motions with a simultaneous redistribution of electrons in many bonds. The nature of bonding and electronic charge distribution, as dictated by symmetry rules,[2] frontier orbitals,[3] or the nodal pattern of the wave function,[4] determines the reaction pathway, while intramolecular vibrational-energy redistribution (IVR) plays a role if the nuclei have enough time to change their positions in the course of the reaction.

Femtosecond time resolution techniques are ideally suited for probing the dynamics in such reactions and for initiating the reaction from a localized (nuclear) wave packet. In the gas phase and under collisionless conditions, studies of the initial, intermediate, and final states associated with the H motion could reveal the dynamics in real time. The packet may directly find its way, or may search through other modes for the reaction coordinate, analogous with direct and complex mode reactions.[5]

A prototype large molecular system exhibiting hydrogen transfer is methyl salicylate (MS) where the structure is either ketonic (before the transfer) or enolic (after the transfer). Based on the dual emission spectrum of MS in solutions, which was first investigated in 1924,[6] the idea of proton transfer to form a zwitterionic species (*vide infra*) was proposed by Weller almost forty years ago.[7] Subsequently, a voluminous literature has discussed MS and similar systems (see, *e.g.*, Refs. 8-25).

A double-well potential (see Fig. 5.1) along a reaction coordinate corresponding to the two forms and responsible for the dual fluorescence is an attractive description, because it simplifies the problem considerably. However, in MS, the validity of the double-well model has received considerable attention (see, *e.g.*, Refs. 4,14,22). For example, if a double-well potential description is correct, the tunneling time in the isolated molecule is expected to be ~10^{-7} s.[14] Goodman and Brus[14] have shown that in neon matrices at 4.2 K, the spectroscopy is not consistent with such a double well behavior. Picosecond time-resolved studies of isolated MS in a molecular beam by Felker *et al.*,[19] and in solution by Smith and Kaufmann[13] have failed to resolve the dynamics of the transfer, indicating that such a H motion occurs on a time scale less than 10 ps. The time scale of the dynamics and the mechanism of the reaction depends on the pathway of the motion, and, as discussed (*vide infra*) recently by Catalán and coworkers[22] and by Nagaoka and Nagashima,[4] the shape of the potential along the reaction coordinate could be highly asymmetric.

The present work focuses on the femtosecond to picosecond dynamics in

isolated MS, building on the earlier studies in the picosecond time domain.[19] The

goal is to resolve the elementary reaction dynamics and to examine the associated
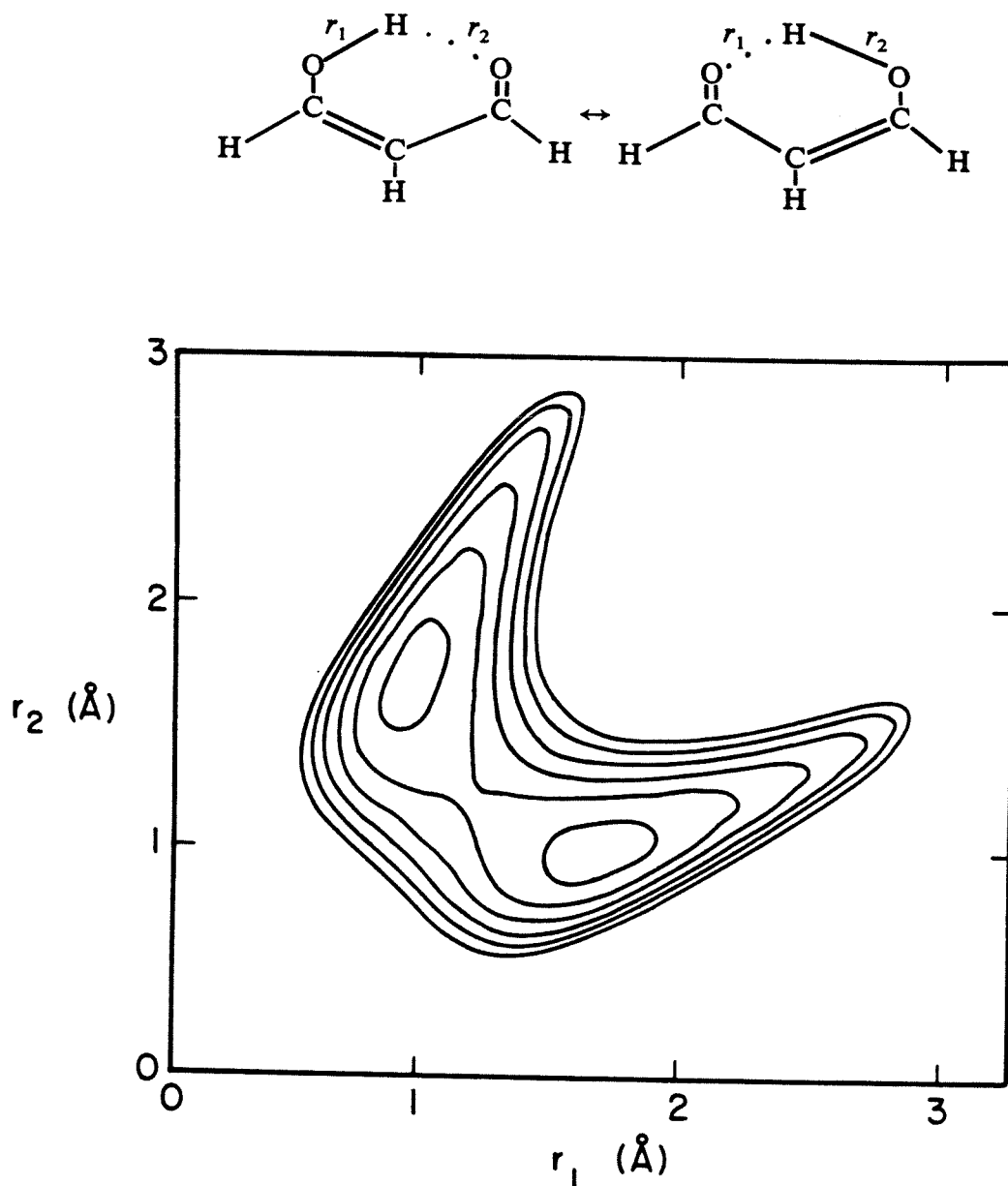

Figure 5.1 Two-dimensional potential energy-surface representing a double minimum for malonaldehyde (from Ref. 26). The importance of the two coordinates r_1, r_2 for bond breaking and bond forming processes is analogous to the description of A + BC reactions (see text).

mechanism of the hydrogen atom transfer. In addition, the coherent nature of the wave packet in a double well or asymmetric potential is of interest as it should reveal the nature of the reaction coordinate and the possible role of IVR. In solutions[27] and clusters,[28] which are not the focus here, there are other interesting questions regarding the role of the solvent and possible intermolecular hydrogen bonding and proton transfer; for examples, the reader is referred to the articles in Refs. 27 and 28.

The ground state (A) of MS has a ketonic structure, and in the first $^1\pi\pi^*$ state $(A^*),$[14] the molecule undergoes a transition to a tautomer (T^*) involving a change of the type:

(2)
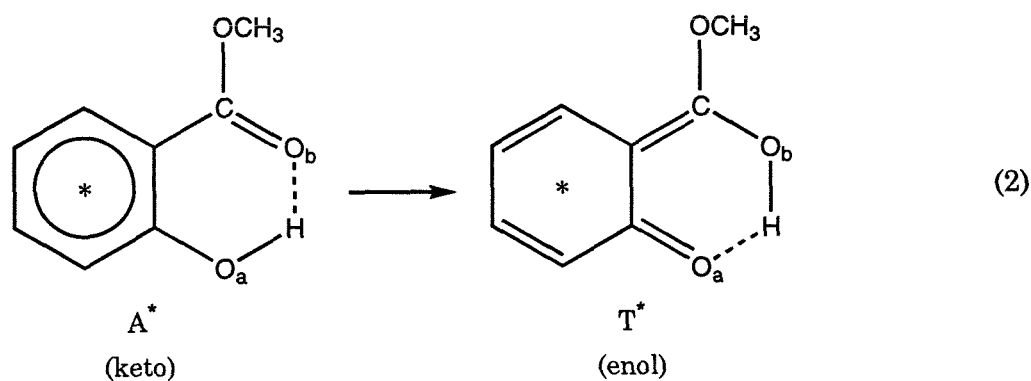
The excited state (A^*) is similar in structure to A and the ultrafast change from A^* to T^* is responsible for the large Stokes shift observed in the emission spectrum. Originally, Weller attributed the dual fluorescence at 330 nm (so-called uv form) and at 440 nm (blue form) to an equilibrium between the initially excited species and a zwitterion where the carbonyl oxygen receives the proton, giving a positive charge to the carbonyl, and leaving behind a negative charge on the phenolic group.[7] This model, which is used in other contexts, turned out to be inapplicable to MS as the uv and blue emissions were found to have distinct excitation spectra in the solution phase,[10,12] in room-temperature vapor,[17] and in supersonic jets.[18] Thus, there is no equilibrium in the excited state; rather, the origin of the dual

fluorescence is due to the presence of two rotamers in equilibrium in the ground
state, A and B. In rotamer A, the phenolic H is intramolecularly bonded to the
carbonyl oxygen, and in rotamer B, to the oxygen of the methoxy group (see Fig.
5.2). With this in mind, the blue emission is due to an excited state proton-
transferred species T*, originated from rotamer A*. The uv emission is due to the
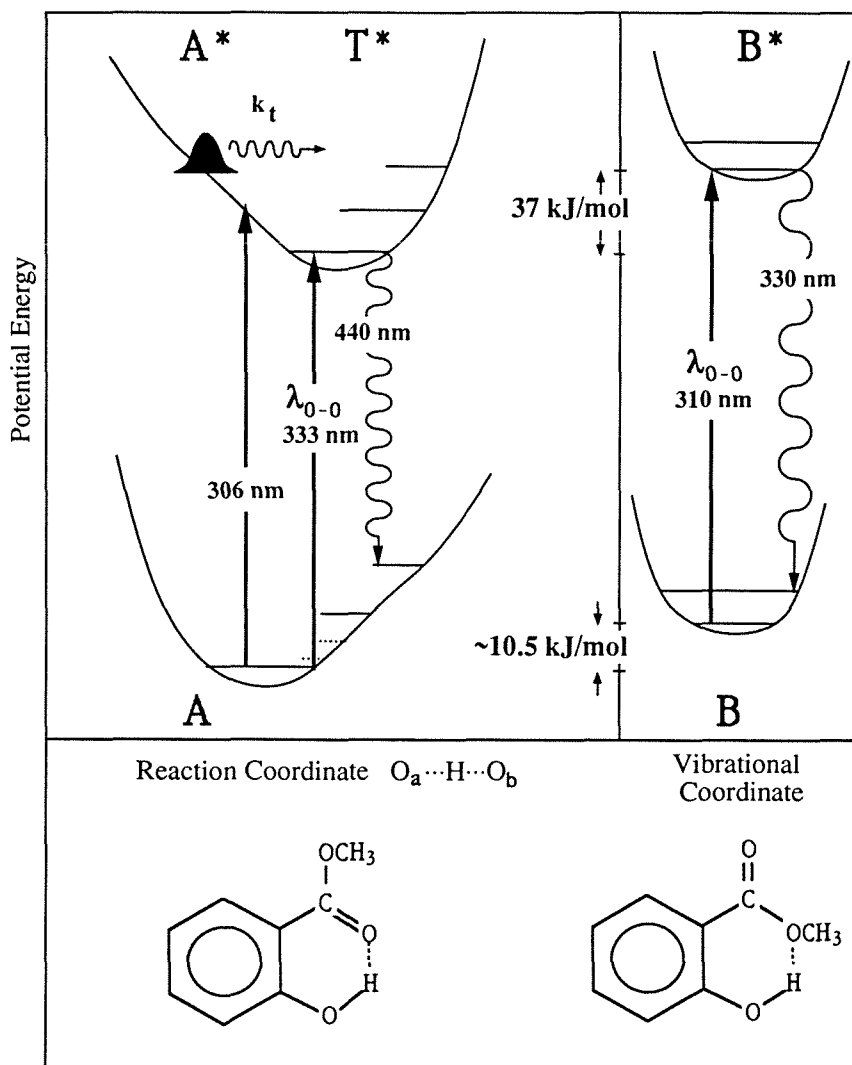excited state B* species.

Figure 5.2 Schematic representation of the MS system for the "blue" and "uv"
rotamers (A and B). In A, the relevant vibrational coordinate of OH stretch (solid
line) and C=O and low-frequency mode (dotted lines) are displayed. The wave
packet is approximately at the total available energy.

A schematic for the potential along the reaction coordinate for A and along the vibrational coordinate for B is displayed in Fig. 5.2. The experiments in supersonic jets by Helmbrook et al.[18] have revealed the high resolution spectra of both forms and provided important spectroscopic information on the vibrational modes and isotope effect. Nishiya et al.[23] have also studied MS and other related compounds and obtained spectroscopic information on the modes and the potentials. The shape of the potential associated with the O-H⋯O mode could not be obtained experimentally, as nonradiative decay of the blue form becomes significant at energies below OH stretch frequencies. Semiempirical and *ab-initio* molecular orbital (MO) calculations indicate either a small barrier to hydrogen transfer,[21,22] or no barrier at all.[4] The picosecond studies[19] of beam-cooled MS explored the fluorescence decay rate as a function of excess vibrational energy and within this time resolution an entrance channel barrier to formation of the blue species could not be observed. However, a marked increase in decay rate beyond a threshold of ~1300 cm^{-1} of excess vibrational energy suggested an exit barrier for the onset of an efficient decay channel. This is consistent with the intensity fall off in the excitation spectrum at the same energy found in the gas phase[16a,17] and in supersonic jets.[18] As discussed below, the experiments reported here on isolated MS address the global nature of the surface and the dynamic motion from the early femtosecond times to the picosecond time regime where the onset of this nonradiative process is observed.

II. Experimental

The femtosecond laser system and data processing methods are been described in detail in Chapter 2. Briefly, the output of a colliding-pulse mode-locked laser (CPM) was amplified in four dye stages pumped by a 20 Hz Nd:YAG laser to

yield ~80 fs pulses of energies up to 0.5 mJ and a central wavelength of 610 nm. The pulses were split into two beams of comparable intensity to provide the pump and probe arms. For wavelengths other than the frequency-doubled fundamental of the CPM, the pump beam was tightly focussed into a cell of D_2O to produce a white-light continuum, from which twice the desired pump wavelength was selected via a 10 nm bandpass interference filter. The transmitted light was further amplified in a flowing dye cell which was end-pumped by residual Nd:YAG 532 nm radiation. The beam was then frequency doubled in a KD*P crystal to produce ultraviolet pump pulses. The pulses generated in this manner had wavelengths in the range of 280 – 330 nm.

The probe beam was used without modification, as only a single probe wavelength of 610 nm was employed in these experiments. The probe beam was propagated through a Michelson interferometer in which its delay relative to the pump beam was controlled by an actuator. The two beams were then colinearly recombined and focussed into the reaction cell. Fluorescence from laser-induced depletion (LID) was collected perpendicular to the propagating beams and dispersed by a 0.33 m monochromator before being detected by a photomultiplier tube. The pump and probe beams were characterized both spectrally and temporally, and the signal linearity was checked throughout the course of this study.

The MS (Aldrich, 99+%) and methyl 2-methoxybenzoate (Aldrich, 99+%) were used as purchased without further purification. A droplet was placed in a static quartz cell, then degassed and the cell evacuated to 10^{-6} Torr; the vapor pressure of MS is approximately 0.2 Torr at room temperature. For experiments involving monodeuterated MS, a stirred solution of MS in a molar excess of D_2O yielded ~60 - 90% of the desired molecule, as confirmed by NMR.
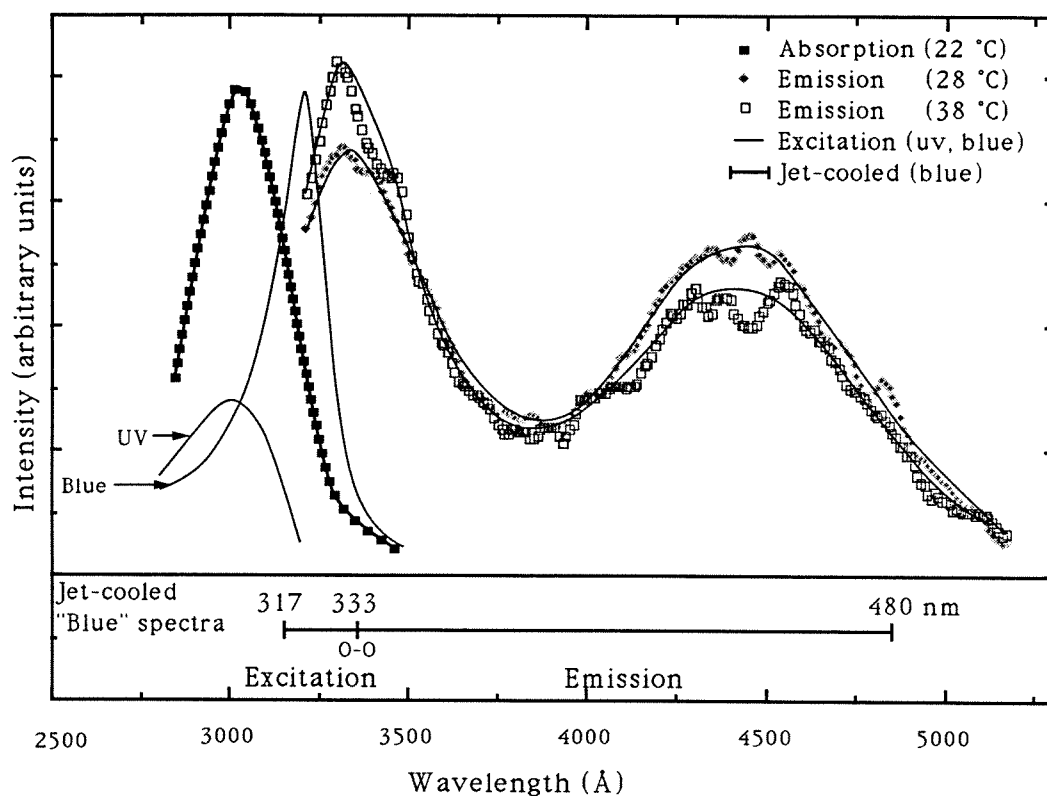
Figure 5.3 Absorption, excitation, and experimentally observed emission spectra of room-temperature MS vapor (P = 0.2 Torr). The ratio of uv/blue emission increases with increasing thermal energy. $\triangle$: T ~28 °C; $\square$: T ~38 °C. Low-resolution (1 nm) absorption and excitation spectra adapted from Ref. 16a. At the bottom, the spectral range of the emission and excitation spectra in jet-cooled MS is shown.

As MS is known to interact strongly with silica,[17] the cell was heated gently to prevent adsorption, especially at the cell windows. Owing to the presence of two MS rotamers in the cell, the relative intensities of the two emission maxima are dependent on the excitation energy, including thermal energy in the ground state, as demonstrated by Klöpffer and Naundorf.[10] This temperature dependence is especially significant in real-time studies, as the measured rates depend on the total energy. Figure 5.3 shows MS fluorescence spectra obtained at 28 and 38 °C, corresponding to a total thermal vibrational energy of 1140 and 1240 cm^{-1}, respectively.[29] The relative ratio of the uv to blue emission observed in the present work is similar in behavior to that of Ref. 16. (Note that this ratio depends on the excitation wavelength and the experimental conditions; the jet result[18] is different

from the cell result.) In Fig. 5.3, the excitation and absorption spectra are shown for comparison.

II.A. Femtosecond Depletion Spectroscopy

Unlike the typical pump-probe experiment in which the pump excites the molecule to an intermediate state and the probe then carries it to a final, fluorescing state, here the emitting state is the intermediate. Thus, following excitation of MS by the pump pulse, the subsequent fluorescence is *depleted* by the probe pulse. Either the blue or the uv form of MS may be probed, depending on factors such as the pump-probe delay and the excited state dynamics. By measuring the dependence of fluorescence intensity on the relative delay between the pump and probe pulses, we directly monitor the dynamics of the molecule in the excited state. This femtosecond depletion methodology is a variant of the picosecond time domain approach[30] of McDonald and coworkers and Felker and coworkers; here we deplete with a different probe wavelength by absorption to a higher excited state, not back to the ground state. Also, the depletion can be made on the initial or final state of the system. With stimulated pumping to the ground state, Chen's group[31] has observed the femtosecond transition-state spectroscopy (FTS) of ozone.

II.B. Analysis and Data Treatment

There are two important time regimes relevant to the dynamics considered here: the short-time femtosecond dynamics and the relatively long-time behavior in the picosecond domain. The analysis of the data in the short-time scale is done considering a molecular response function, $M(t_D)$, the transient shape which would be obtained when the pump and probe pulses are infinitely narrow, which is then convoluted with the instrumental response function of the system (see Herek *et al.*, J. Chem. Phys. **97**, 9046 (1992) for more details). In these experiments, the I_2

transient[32] was used as an internal calibration of the instrumental response function, as its shape is given by the convolution of the pump and probe profiles (instantaneous rise) with a long single-exponential decay function reflecting the very long (microsecond) lifetime of I_2. In addition, the autocorrelation functions of both laser pulses were carefully measured (in the case of the uv pump laser, the residual visible light after the doubling crystal was used) and fit to Gaussian functions.
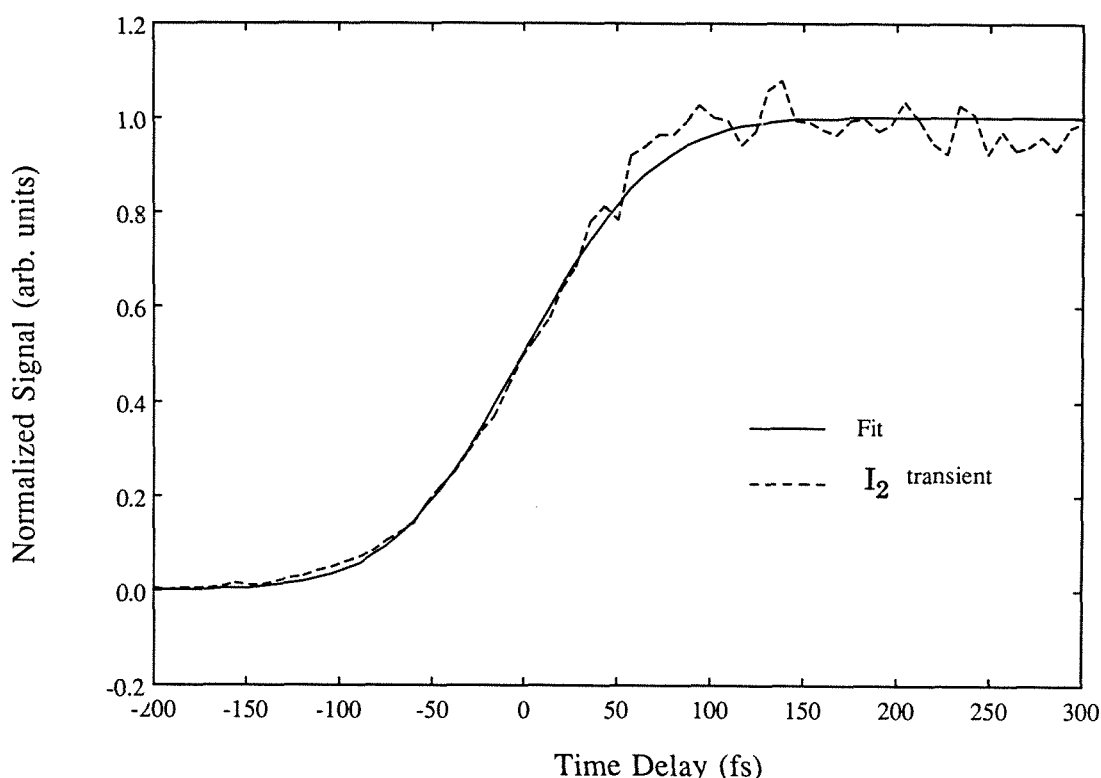
Figure 5.4 I_2, 610/(340)/305, transient (dotted line) in the femtosecond time scale. The solid line is obtained by convoluting a single-exponential (I_2, long time) decay molecular response function with a Gaussian cross-correlation function of 135 fs (FWHM). The measured FWHM of the Gaussian autocorrelation functions for the pump and probe laser pulses are 100 and 90 fs, respectively.

Figure 5.4 shows a typical I_2 transient in the short-time scale. The solid line in the figure is the convolution of a long time single-exponential decay molecular

response function with the Gaussian cross-correlation function whose full width at half maximum (FWHM) is obtained from the measured autocorrelation functions as $F_{xcorr}^2 = F_{pump}^2 + F_{probe}^2$, where F_i is the FWHM of each function.[33] Using this characterization of the instrumental cross-correlation function, the MS experimental data were fit by convoluting an appropriate molecular response function with this cross-correlation function. From simulations, we found that with a Gaussian cross-correlation function of ~130 fs (FWHM), rise times in the transients as short as ~40 fs can be resolved.

III. Results

The femtosecond dynamics in the excited state of MS were obtained by monitoring fluorescence as a function of time using the depletion method described above. Both short and long (up to 120 ps) transient signals were obtained, detecting fluorescence at both emission maxima: 330 and 440 nm. Typical data in the long time scale are presented in Fig. 5.5, where the *depletion* of fluorescence resulting from absorption of the probe pulse is clearly demonstrated. The zero of time, in which the pump and probe pulses are temporally overlapped, has been (arbitrarily) set at the onset of depletion. In the case of the 330 nm emission, the lifetime of the corresponding state (~1.1 ns) [Ref. 16b] is very long on our time scale, leaving the excited state population relatively constant following excitation by the pump pulse. Hence, the depletion by the probe varies little with time delay (on a picosecond time scale). In contrast, the 440 nm emission displays a measurable decay on the picosecond time scale. The decay is represented by a single exponential.

In Fig. 5.5, the fluorescence signal is decreased when the pump precedes the probe, as expected for a depletion experiment. However, in all following transients, the data are inverted to allow for discussion of the rise and decay components of the

depletion in a more conventional manner. Throughout, we shall use a shorthand notation to indicate the pump, fluorescence-detection, and probe wavelengths, *i.e.* $\lambda_{pu}/(\lambda_{det})/\lambda_{pr}$. For instance, 305/(440)/610 means that the MS was initially excited with a 305 nm pump laser, and the subsequent fluorescence of the intermediate state at 440 nm was depleted with the 610 nm probe laser.
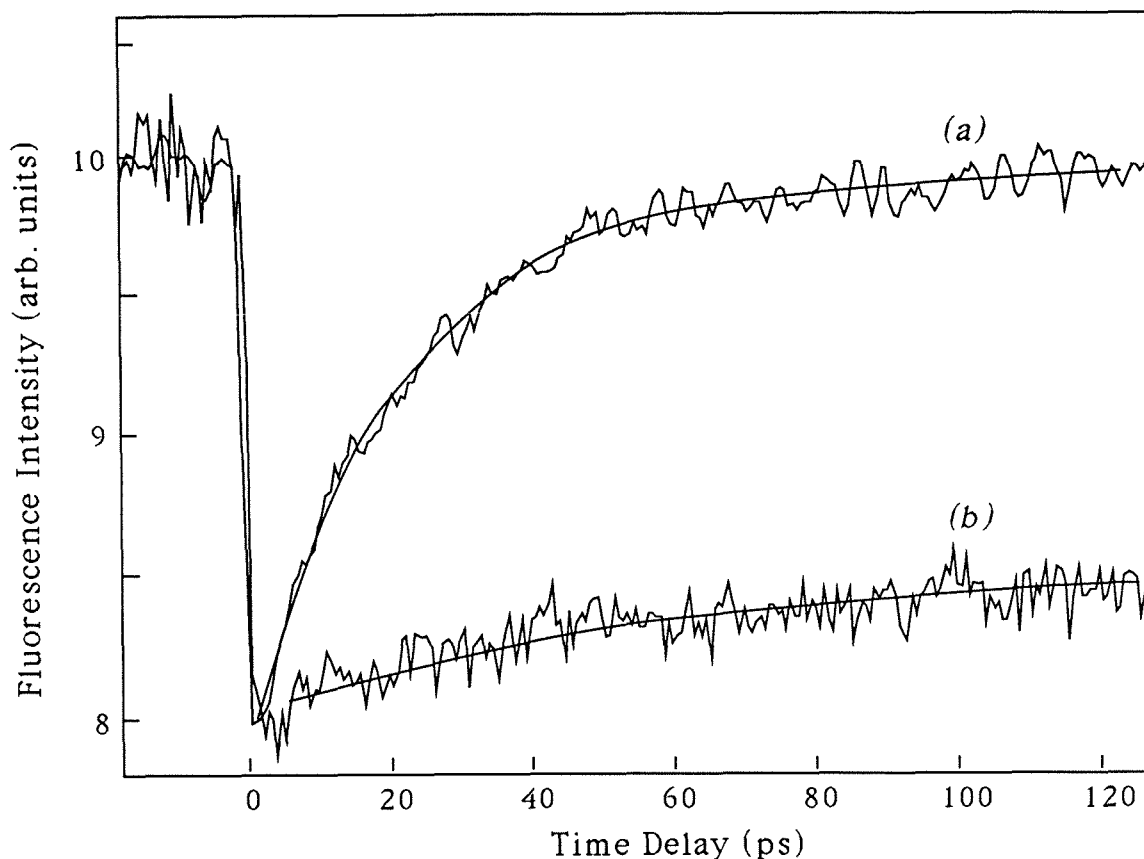
Figure 5.5 Experimental depletion results. In both transients, λ_{pu} = 305 nm, λ_{pr} = 610 nm. *(a)* Detection of 440 nm emission (A form). *(b)* Detection of 330 nm emission (B form).

III.A. Femtosecond Time Scale: Short-Time Behavior

Of particular interest to this work is the detection of any rise component in the 440 nm fluorescence depletion transients; such a rise should correspond to the time required for the motion of the hydrogen. For that reason, the temporal behavior of the fluorescence at 330 and 440 nm has been measured on a

femtosecond time scale. For these experiments, the pump and probe wavelengths were 305 and 610 nm, respectively, and the thermal vibrational energy was varied by changing the temperature.

Figure 5.6 Fluorescence depletion transients (305/610) detecting the emission at *(a)* 440 nm and *(b)* 330 nm, on the femtosecond time scale (solid lines). The I_2 610/(340)/305 transient is also shown for comparison (dotted line). Temperature: 28 °C.

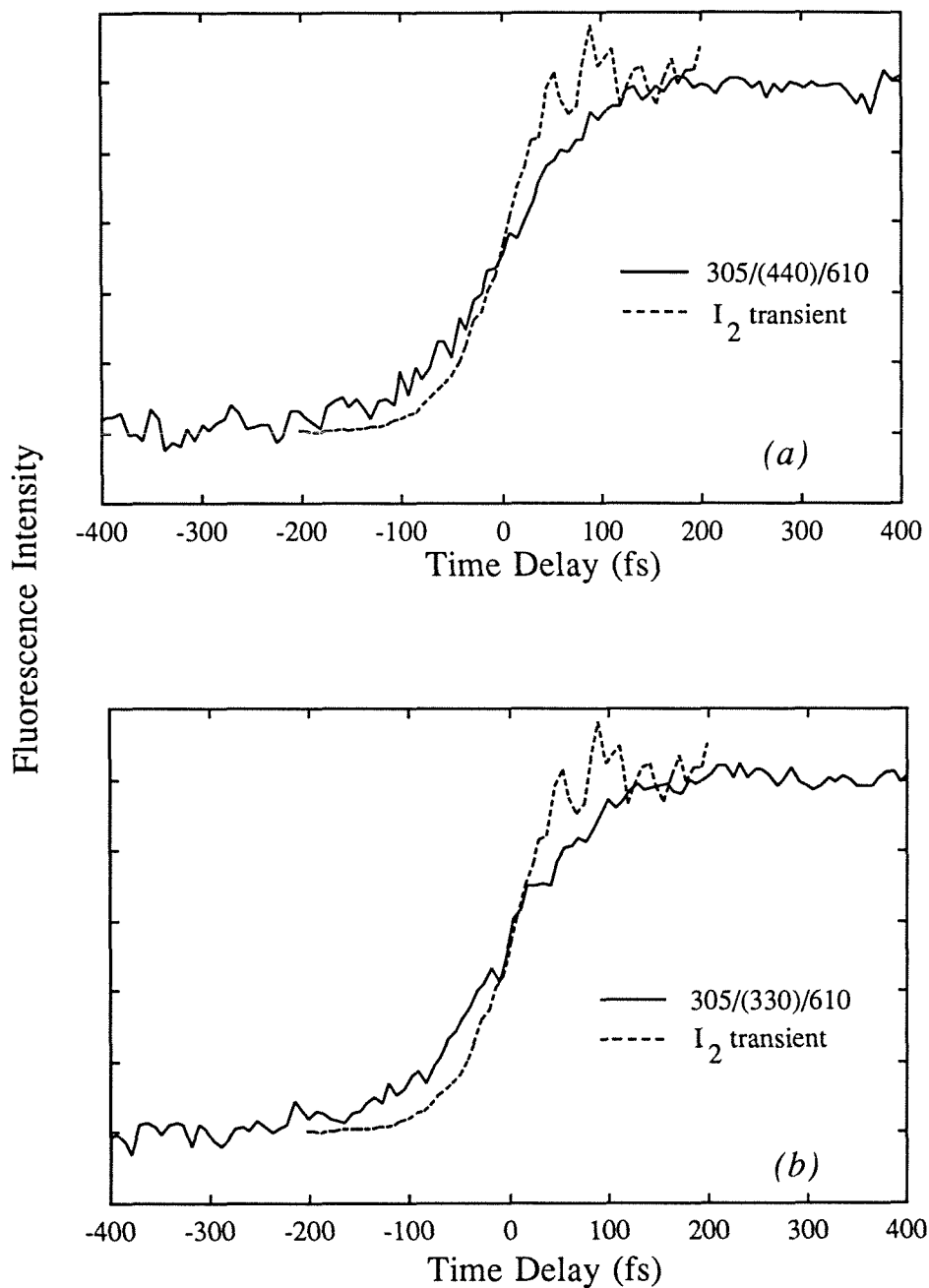Figure 5.6 shows typical fluorescence depletion transients detecting at 330 and 440 nm. The I_2 transient, reflecting the cross-correlation function of the system, is also shown for comparison. Both MS transients (330 and 440 nm detection) are quite similar and show a slower rise than I_2.[34] Note that the 330 and 440 nm transients have been normalized to allow for comparison. Figure 5.7 shows how these transients are not affected by variations in temperature. Although the relative intensities of the two emission signals depend on the thermal energy (as discussed in Sec. II), the rise is unaffected.

III.B. Energy Dependence: Long-Time Behavior

The fluorescence was studied as a function of excitation energy in 10 nm increments from 330 nm to 280 nm. Throughout this range, the transient observed with 330 nm detection (*i.e.* fluorescence originating from the uv species) was unaffected by any pump energy variation. With 440 nm detection of the blue species, however, the decay rate is strongly dependent on the pump energy. Figure 5.8 presents experimental transients obtained with pump wavelengths of (a) λ_{pu} = 330 nm, (b) λ_{pu} = 310 nm, and (c) λ_{pu} = 290 nm, corresponding to excess vibrational energies of 1460 cm^{-1}, 3650 cm^{-1}, and 5670 cm^{-1}, respectively.[29] For low energies, the decay had been studied previously[19] via picosecond fluorescence spectroscopy in supersonic beams and the subnanosecond time constants could be measured quite accurately. Here, given the constraint of 120 ps for these femtosecond experimental scans, only the very rapid decays at higher energies could be fitted with reasonable accuracy.

Figure 5.9 shows the effect of the initial thermal energy on the observed decay and Table I lists the time- and rate constants corresponding to excitation energies used both in the current work and in previous experiments,[19] where supersonic-cooled MS was studied only up to E_v = 1850 cm^{-1}.
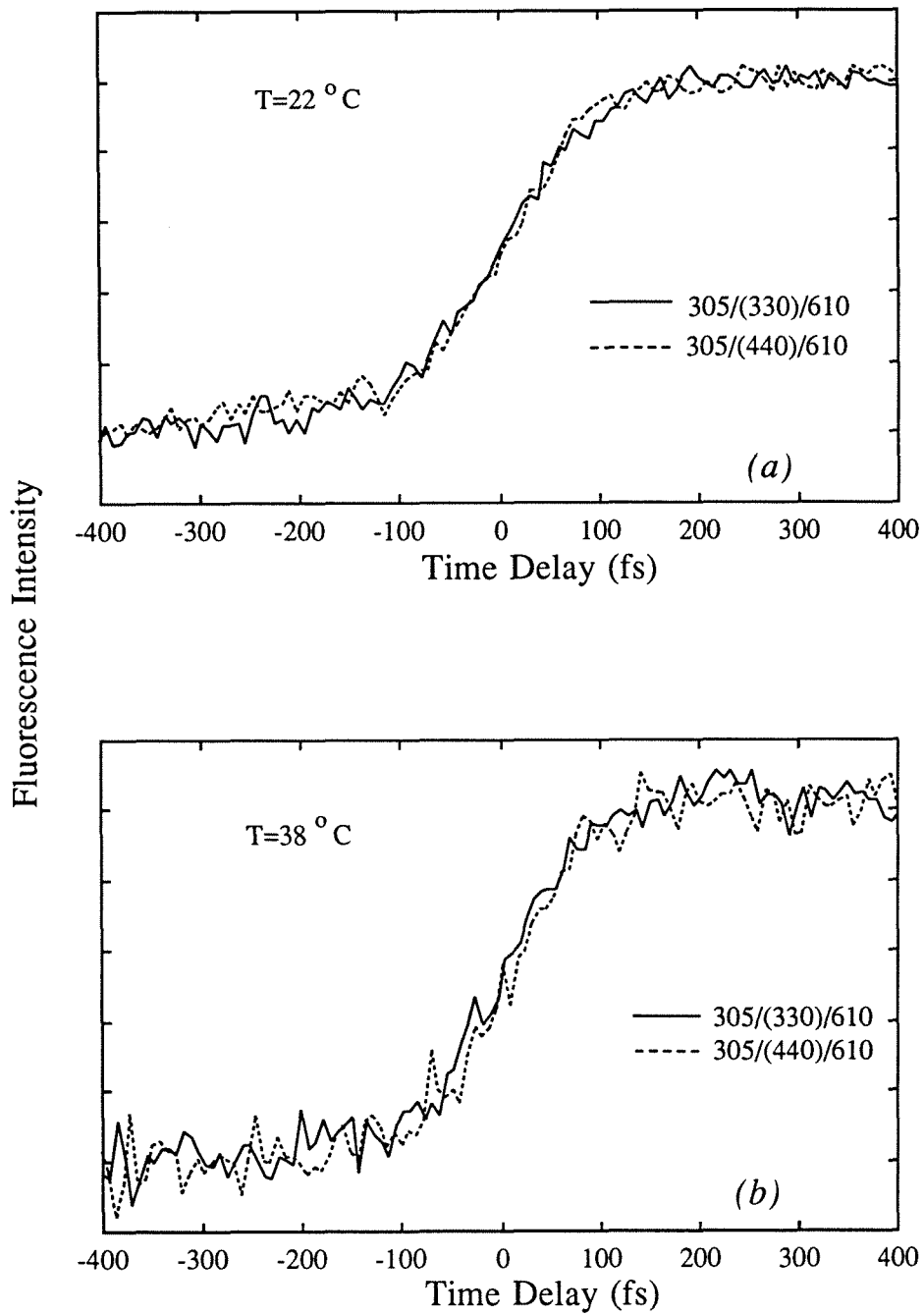
Figure 5.7 Effect of the temperature on the transients. The 305/(440)/610 and (330) fluorescence depletion transients in the femtosecond time scale are shown for two different temperatures: *(a)* 22 °C, and *(b)* 38 °C.

	λ	τ
	330 nm	730 ps
	310 nm	31.5 ps
	290 nm	13.5 ps

$E_v = 1459 \text{ cm}^{-1}$

$E_v = 3653 \text{ cm}^{-1}$

$E_v = 5669 \text{ cm}^{-1}$
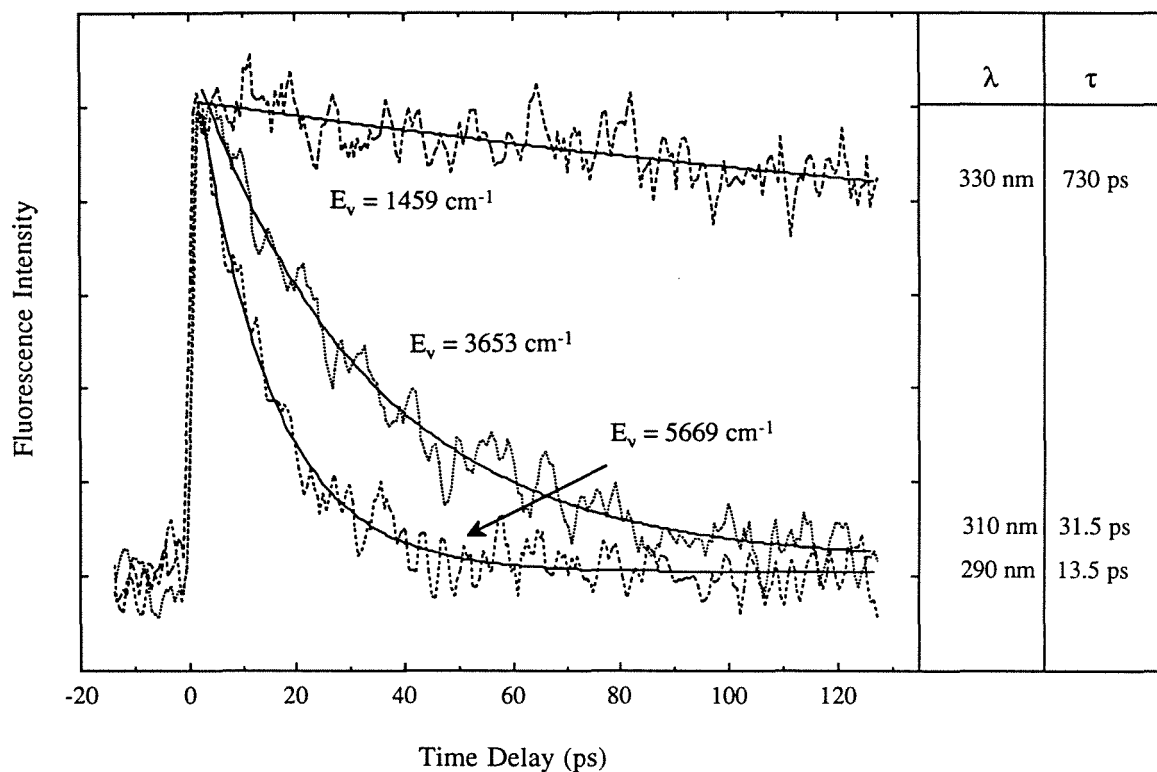
Figure 5.8 Transients observed for the 440 nm emission as a function of excitation energy. The solid lines are least-squares single exponential fits to the data, yielding the time constants as shown.

Table 1. Measured decay time constants and their corresponding rates as a function of excess vibrational energy (E_v).

E_v (cm^{-1}) Ref. 30	τ	k (10^9 s^{-1})	Reference
0	12.0 ns	0.083	Ref. 20[b]
300	10.0	0.100	Ref. 20
911	6.5	0.153	Ref. 20
1043	5.2	0.191	Ref. 20
1225	2.0	0.493	Ref. 20
1312	1.1	0.893	Ref. 20
1459	730 ps[a]	1.4	This work
1573	349	2.86	Ref. 20
1850	160	6.29	Ref. 20
2544	73 ± 20	13.7 ± 2	This work
3653	31.5 ± 4	31 ± 3	This work
4519	21.7 ± 2	46 ± 4	This work
5669	13.5 ± 1.5	73 ± 8	This work
7157	8.5 ± 0.9	119 ± 12	This work

[a]On our picosecond time scale, the transient decay for this experiment was nanosecond in nature. Therefore, the estimated error is large (approximately 50%).
[b]Earlier beam results from this laboratory.
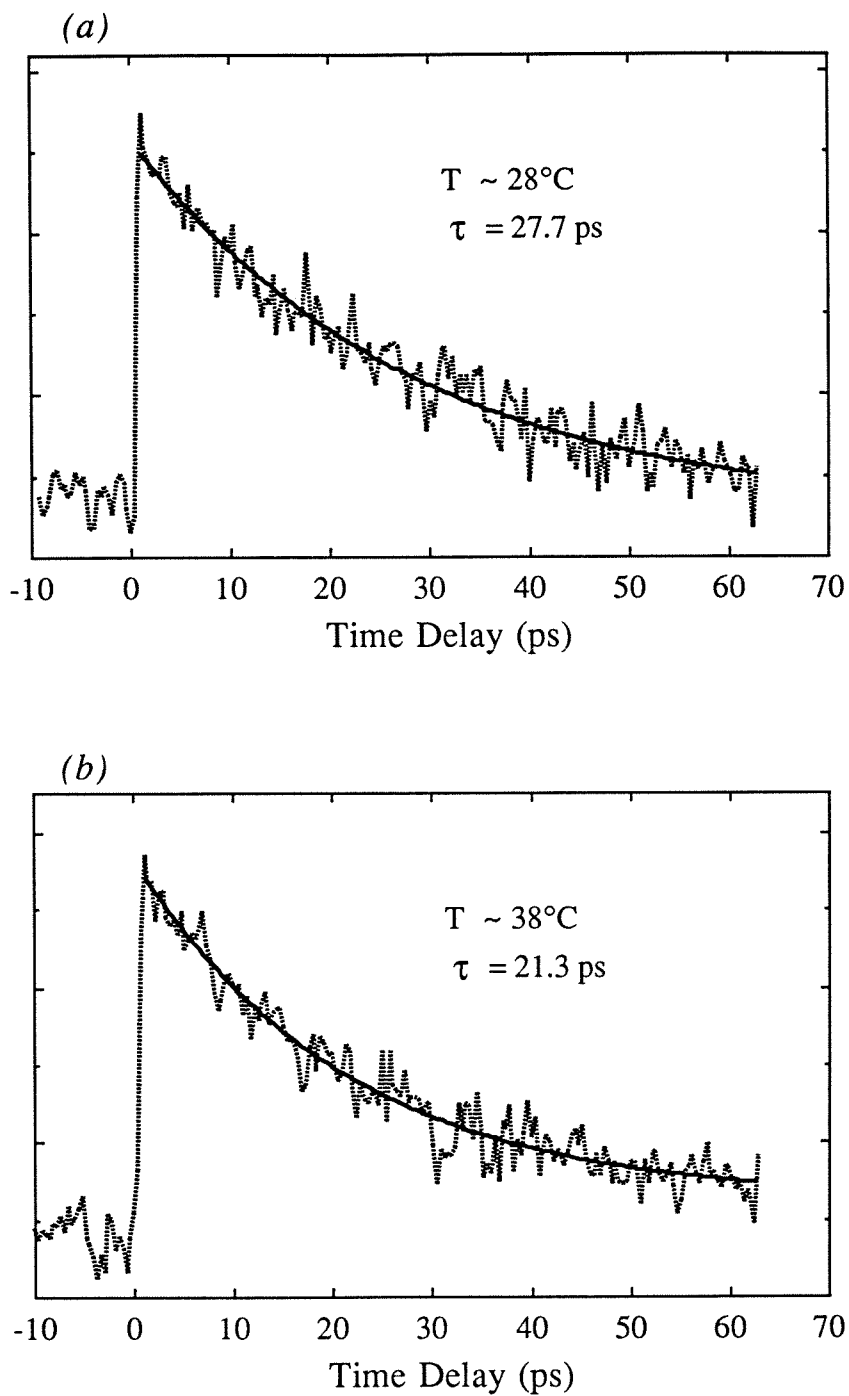
Figure 5.9 Effect of temperature on the picosecond transients. Detection of 440 nm emission at *(a)* T ~28 °C, and *(b)* T ~38 °C. The decay rate increases with increasing temperature, as reflected by the time constants τ (see text).
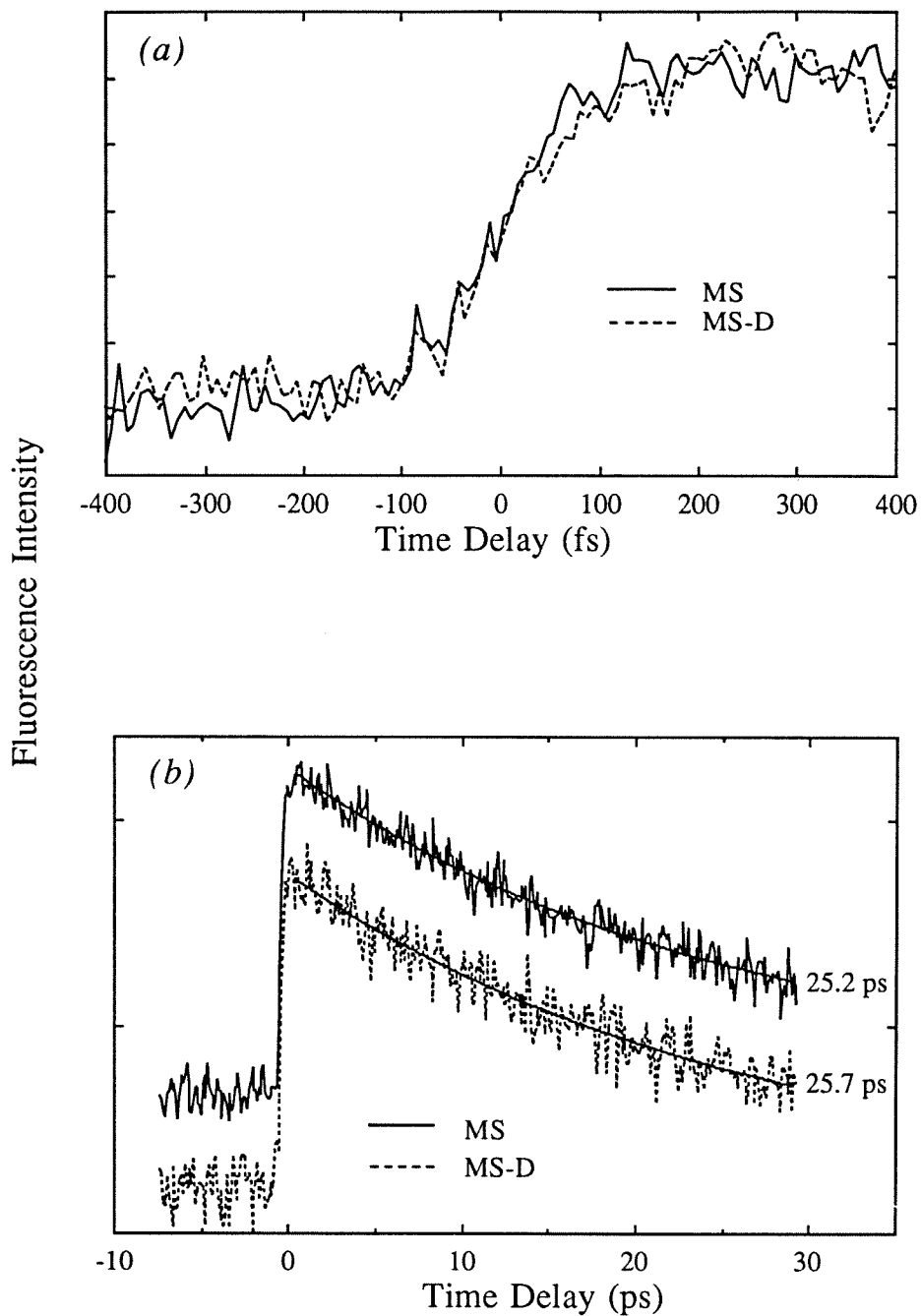
Figure 5.10 305/(440)/610 fluorescence depletion transients for MS and MS-D (isotope effect): *(a)* short time scale, *(b)* long times scale. Solid line: MS signal; dotted line: MS-D signal.

III.C. Deuterium and CH₃ Substitution Effect

Similar experiments (short and long time scales) were performed on two variations of MS: the monodeuterated (MS–D) species, in which the hydrogen of interest is replaced by a deuterium atom, and methyl 2-methoxybenzoate (MS–CH₃), in which the hydrogen is replaced by a methyl group. The MS–D behaved the same as MS. Figure 5.10 shows transients in both the femto- and picosecond time scales, detecting at 440 nm (rotamer A). No apparent differences in the rise are observed and the decay rates are identical. As has been previously observed,[7] the MS-CH₃ showed a very different fluorescence spectrum from that of MS: a large peak at 350 nm was followed by a long tail to the red with no second peak at ~440 nm (*i.e.* no hydrogen dynamics). Depletion of the 350 nm fluorescence emission was analogous to that of the corresponding 330 nm signal of MS, though considerably smaller.

IV. Discussion

The results presented in the previous section illustrate two dynamical processes in MS, one of which is responsible for the Stokes shifted emission, and the other, for the nonradiative decay in the hydrogen-transferred form. In this section, the origins of these processes are examined with particular focus on the time scale of the elementary step of the reaction and its associated mechanism.

IV.A. Reaction Dynamics

IV.A.1. Preliminaries

Unique excitation spectra of the two rotamers were first recorded by Klöpffer and Naundorf, who also showed that the relative intensity of the two fluorescence bands depends on the excitation wavelength.[10] The structures of the two rotamers A and B have been studied by Catalán *et al.*,[16] and Pimentel and coworkers.[25] High-

resolution emission spectra have been obtained in supersonic beams[19] and in durene crystals (4.2 K).[23] The 0–0 transitions for the uv- and blue-emitting species in the gas phase are at 309.6 nm and 332.7 nm, respectively. In the ground state, the two species differ in enthalpy by 10.5 kJ/mol;[18] in the excited state, by 37 kJ/mol according to the difference in 0–0 transition energies. Under the assumption that the ratio of the fluorescence reflects the ratio of the population after correcting for the relative transition strengths, it was concluded that the uv form is about 1/70 of the blue in the ground state[18] (note that the blue quantum yield decreases with energy).

The two species exhibit markedly different fluorescence lifetimes. Upon excitation at their respective 0–0 transition energies, $\tau_A = 12.0 \pm 0.5$ ns[14,19] and $\tau_B = 1.1 \pm 0.2$ ns.[16] For rotamer B, this value is independent of excitation energy, however for species A, the observed decay time depends on the excitation energy, as will be discussed in Sec. IV.B. The state of the blue form has been assigned to a $\pi\pi^*$ transition, based on the oscillator strength, isotope shift, and the mode structure (for discussion, see Refs. 4,14,18). The uv form has been attributed (most likely) as due to $n\pi^*$, again based on spectroscopic and theroretical studies.[4,18] For the blue form, the isotope shift of the transition is -99 cm^{-1} and the prominent vibrational modes relevant here are: $v_{OH}^{ground} = 3258$ cm^{-1}, $v_{OH}^{excited} = 2582$ cm^{-1}, $v_{C=O}^{ground} = 1690$ cm^{-1}, $v_{C=O}^{excited} = 1094$ cm^{-1}, and low-frequency modes, *e.g.*, 180 cm^{-1} in the ground state and 176 cm^{-1} in the excited state.[18,19]

The relevant potential energy curves along the O–H⋯O "reaction coordinate" have been discussed qualitatively and semi-quantitatively by various groups.[4,14,17,18,21,22] On the basis of the correlation between the change in OH stretch frequency and the change in bond length, Helmbrook *et al.*, estimated the distance of hydrogen transfer to be 0.1 – 0.2 Å.[18] The excited state O–H stretch frequency mentioned above (and not observed due to nonradiative decay) was

estimated to be 2582 cm^{-1} based on the deuterium-induced shift of the 0–0 transition (99 cm^{-1}).

Semiempirical molecular orbital (MO) methods were used by Orttung *et al.*,[21] and by Catalán *et al.*[11,22] in investigations of various ground- and excited-state properties of MS and related molecules. It was found that the shape of the excited state potential energy curves strongly depends on the relative distance between the phenolic and carbonyl oxygen atoms (O_p and O_c, respectively).[11,22] Recently, Nagaoka and Nagashima reported "*ab-initio*" MO calculations in an analog of MS: *o*-hydroxybenzaldehyde (OHBA).[4a] Their results suggest that a tautomerization from the closed conformer A* to the tautomer T* is more likely than an actual proton-transfer process. These results will be discussed in Sec. IV.A.3.

Further observations relevant to our study of the hydrogen-transfer dynamics in isolated MS are found in previous time-resolved work. In the picosecond time domain, no rise component of the fluorescence signal in a supersonic beam was measured, setting a lower limit on the rate of hydrogen transfer as 10^{11} s^{-1}, the instrumental response function.[19] These beam experiments are also consistent with the limit deduced in the solution phase.[13]

A culmination of the above observations together with the measurements presented here gives a reaction coordinate of the type shown in Fig. 5.2 for the femtosecond dynamics. The vertical transitions represent the 0–0 transition energies of the two species and their associated fluorescence maxima. The elusive hydrogen-transfer rate in rotamer A is shown as k_t. The relative energies of the two species are displaced according to the measured enthalpy differences. These data will be used in conjunction with the present results to formulate an understanding of the dynamics discussed in the following sections.

IV.A.2. Femtosecond Dynamics

Given the previous upper limit of 10 ps for the time scale of hydrogen transfer, the present femtosecond experiments focussed on the early-time behavior of the fluorescence depletion signal. The observations at early times bring two issues into the dynamics: the nature of the initial coherent packet on the potential and the evolution of the packet with time along the O–H···O (and other) coordinates. Before considering these aspects of the motion, it is useful to obtain the rates (the incoherent trajectories) of the level structure representing the MS system.

A simple kinetic model is used to illustrate the different processes involved in the hydrogen-transfer reaction. In the depletion of the blue signal, two rate constants are involved: the hydrogen-transfer rate, k_t, and the nonradiative rate, k_{nr}. If the cross-section for the hydrogen-transferred state at the probe wavelength λ_{pr} is nonzero but that of the untransferred state A* is negligible, and if the hydrogen-transfer rate is much faster than the nonradiative rate, $k_t \gg k_{nr}$, then the depletion of the blue signal at 440 nm will rise with k_t and decay with k_{nr}.

The model also explains why, if $k_t \gg k_{nr}$, the "resonance" fluorescence (which is in the uv, similar to that from B*) signal from A* will be several orders of magnitude less than the blue signal. In the experiment, however, the amount of uv fluorescence signal observed is on the same order of magnitude as the blue signal, hence the total uv signal must be due almost entirely to the emission from B*. Accordingly, the depletion of the total uv signal should decay with the fluorescence lifetime of B*. If this fluorescence comes directly from the initially excited state of rotamer B and if fluorescence is the only decay channel, then there will be no additional rise time for the uv depletion other than that due to the finite widths of the laser pulses and the dynamics of the packet from the initial non-equilibrium state prepared by the pump pulse.
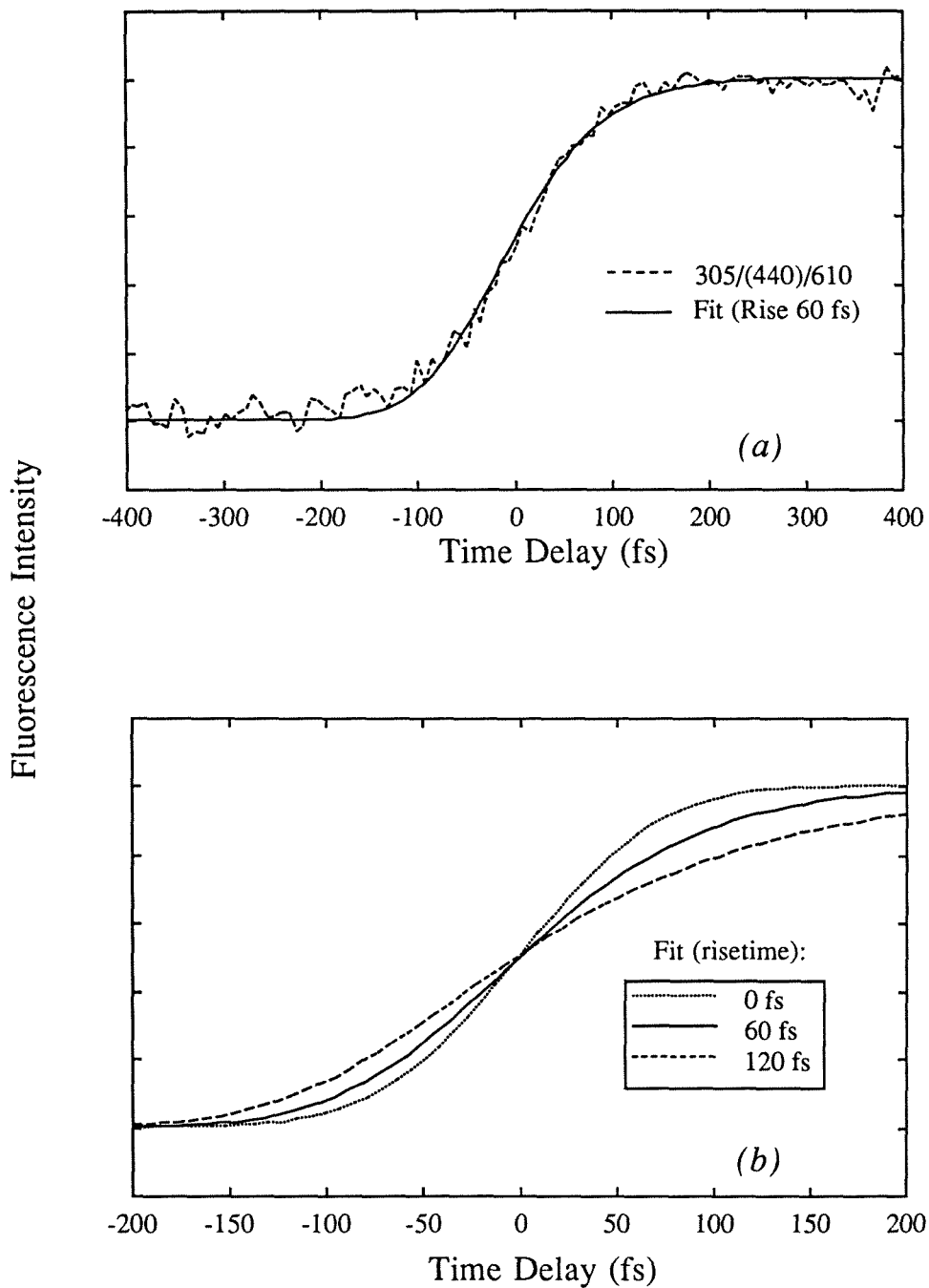
Figure 5.11 *(a)* Typical 305/(440)/610 depletion transient in the femtosecond time scale (dotted line). The solid line is obtained by convoluting a bi-exponential molecular response function (one component in the rise) with the characterized Gaussian cross-correlation function of the system. FWHM (cross-correlation function) = 138.5 fs; τ_{rise} = 60 ± 10 fs; τ_{decay} =30 ps. *(b)* Several fits are shown corresponding to different rise times: 0, 60 and 120 fs. The other parameters remain the same.

Figure 5.11a shows a typical depletion transient for a 305/(440)/610 experiment on the femtosecond time scale. To fit this data, the convolution of a bi-exponential molecular response function (where one of the exponential components is in the rise) with the characterized cross-correlation function of the system was needed (see Sec. II.B). The solid line in the plot was obtained including an additional rise time of 60 ± 10 fs. This result, in view of the kinetic model described above, would suggest that the 60 fs corresponds to the rate of the hydrogen-transfer process described by k_t.

In the transient of 305/(330)/610, *i.e.* exactly the same experiment except detecting the fluorescence at 330 nm (non-hydrogen-transferred species B*), similar rise times and time-zero positions were obtained (to within our resolution). As with rotamer A, when rotamer B is initially pumped from the ground to the excited state by a 305 nm femtosecond photon, a coherent wave packet is produced. This packet requires some time to spread out in the multidimensional potential energy surface before reaching an appropriate equilibrium region from which the fluorescence is emitted, taking into account the role of Franck-Condon factors. This dispersion of the packet arises as it experiences a large change in the force (–dV/dR) at the vertical excitation. Such dispersions have been observed in elementary systems.[35]

For rotamer A, the evolution of the packet as it moves from the initial non-equilibrium position is similarly explained. The OH stretch period is 13 fs, taking an O–H stretch frequency of 2582 cm⁻¹.[18] Therefore, if the hydrogen movement is less than the vibrational amplitude, then within 60 fs of wave packet evolution, the "movement" of the hydrogen atom of interest along the reaction coordinate is complete. To better understand the time scale of the motion we have considered three simple representations of the hydrogen-transfer potential.

If the system is moving from the initial nonequilibrium configuration (keto structure) to the hydrogen-transferred configuration (enol structure) as a free

particle, then given the available energy of ~3900 cm^{-1}, the time for motion is extremely short: a few femtoseconds. If, instead, we take the "repulsive wall" of the asymmetric potential to be exponential, one can calculate the propagation time including the acceleration due to the potential;[35-37] in this case, it is ~3 fs for a distance span of ~0.2 Å.

A more realistic potential is to consider a double well formed from two Morse potentials[38] (or others[39]), but now introduce an asymmetry to the potential. Doing so and integrating the equation of motion resulted in τ ~ 4 fs for a distance of ~0.2 Å. In the above calculations we have assumed that all available energy is in the reaction coordinate. If all modes (for MS, 51) are accepting modes in the packet preparation, then if even one tenth of the energy ends up in the reaction coordinate, τ will be approximately ten femtoseconds (note that for free motion, $\tau \propto E^{-1/2}$).

The above picture considers the problem as one-dimensional, with the H between two oxygens. Considering the O–H⋯O as a normal mode actually makes the time shorter,[40] but considering the second (and higher) dimensions of the potential is a more realistic step as out-of-plane low frequency modes are strongly coupled[41] to the stretch motion. The coupling is due to the large anharmonicity caused by the disparity in masses between hydrogen and oxygen atoms. In a dynamical description, this means that at t=0, the packet is coherently prepared in the initial mode(s), but with time it reaches the reaction coordinate by motion in (at least) two dimensions. Such behavior has been observed (as resonance) in elementary[35] and even complex reactions.[42]

For MS in the blue form, the 176 cm^{-1} mode, for example, gives a half period of 90 fs and this is the time scale of interest here. Consistent with experiments, deuterium substitution will not have an effect on this motion (Fig. 5.10), nor will the excess energy (Fig. 5.7) as the time scale of the reaction is ultrashort. This description is also supported by the vibronic activity in the hydrogen-transferred

form. Felker *et al.*[19] resolved in the emission three types of modes: the low frequency 180 cm^{-1} progression (built on the 0–0, C=O and OH stretches, and tentatively assigned as out-of-plane bending motion of the "ring" that includes the intramolecular hydrogen bond); 1690 cm^{-1}, the ground state carbonyl stretch; and 3220 cm^{-1}, the OH stretch. In the excited state, presumably the 180 cm^{-1} becomes the 176 cm^{-1} and the C=O and O–H undergo reduction to 1094 cm^{-1} and 2582 cm^{-1}, respectively, consistent with a hydrogen-transferred form with change in the CO and OH bond order. The excitation spectrum is quite congested at higher energies and certainly at our available energy they must reflect a broadening of at least 60 fs duration.[43] Also, the maximum of the emission is displaced by ~2 quanta of OH stretch[19] from the 0–0 transition, and the absorption by ~1 quantum of OH stretch from the 0–0, giving rise to a net Stokes shift of ~10,000 cm^{-1}.[23]

The division of the surface into a 2-dimensional potential, involving two OH bond lengths (the bond being broken and the bond being formed), from the remaining harmonic motions is consistent with the theoretical work by Miller's group on malonaldehyde.[26] In the malonaldehyde case the transfer is coherent in a double well and the estimated splitting is ~20 cm^{-1} giving a half period of ~1 ps.

The asymmetric potential discussed here for MS is more generic to most systems (than a double-well potential) and one must consider the effect of exoergicity on the redistribution of energy. In the preparation process, IVR will feed energy to the reaction coordinate. In the transfer process, the system is left "hot," and by "exit channel" IVR, the T* will cool along the reaction coordinate. In other words, the other modes take energy away leaving the reaction coordinate with less energy. The potential in this case must take into account the adiabatic changes of the nuclei and we cannot speak of two coordinates anymore. It would be very interesting to apply Miller's approach to such asymmetric potentials, perhaps dividing the phase space into reactive and nonreactive modes.

The aforementioned result also suggests the absence of any significant barrier in the excited-state potential energy surface of rotamer A as this barrier would result in a coherent trapping and oscillation, or to a delay in the appearance of the H-transferred form. As the spreading of the packet in these large systems is also determined by the multidimensionality of the potential, experiments with shorter pulses may lead to faster spreading (and rise) if a coherent state is prepared. As discussed in Sec. IV B, although a barrier is not present for the initial hydrogen transfer, there is a barrier in the exit channel of ~15.5 kJ/mol. Rauh[8] has calculated (MO) the keto-enol transformation assuming smooth adjustments as the hydrogen moves and found the minimum to be in the middle of the reaction coordinate. The degree of asymmetry and its position requires more accurate calculations.

IV.A.3. Proton Transfer and Tautomerization

Usually, two reaction pathways are used to account for the Stokes shifted emission in systems of this type. The first involves formation of a *zwitterionic* species via a fast, "localized" proton-transfer process, and the second involves distortion of the entire molecular skeleton due to a tautomerization process.

Formation of a *zwitterionic* structure was proposed by Weller[7] and also by Smith and Kaufmann following studies of MS in solution.[13] They suggested that the change in pKa in the excited state of MS induced a complete charge transfer of the phenolic proton to the carbonyl oxygen, accompanied by fluorescence at 440 nm. However, Nagaoka *et al.* showed that the fluorescence decay rate constant is practically independent of the dielectric constant of the solvent.[20] In addition, such a *zwitterionic* structure is likely to be unstable due to Coulombic attraction between the separated charges, unless stabilized by the solvent. The distance between the two oxygen atoms (O_a and O_b) is on the order of 2.5 Å, according to geometry

optimization of the excited state.[4a,21,22] The calculated atomic charges on the two oxygen atoms were found to be similar, suggesting that the excited state molecule is not ionic.[4a]
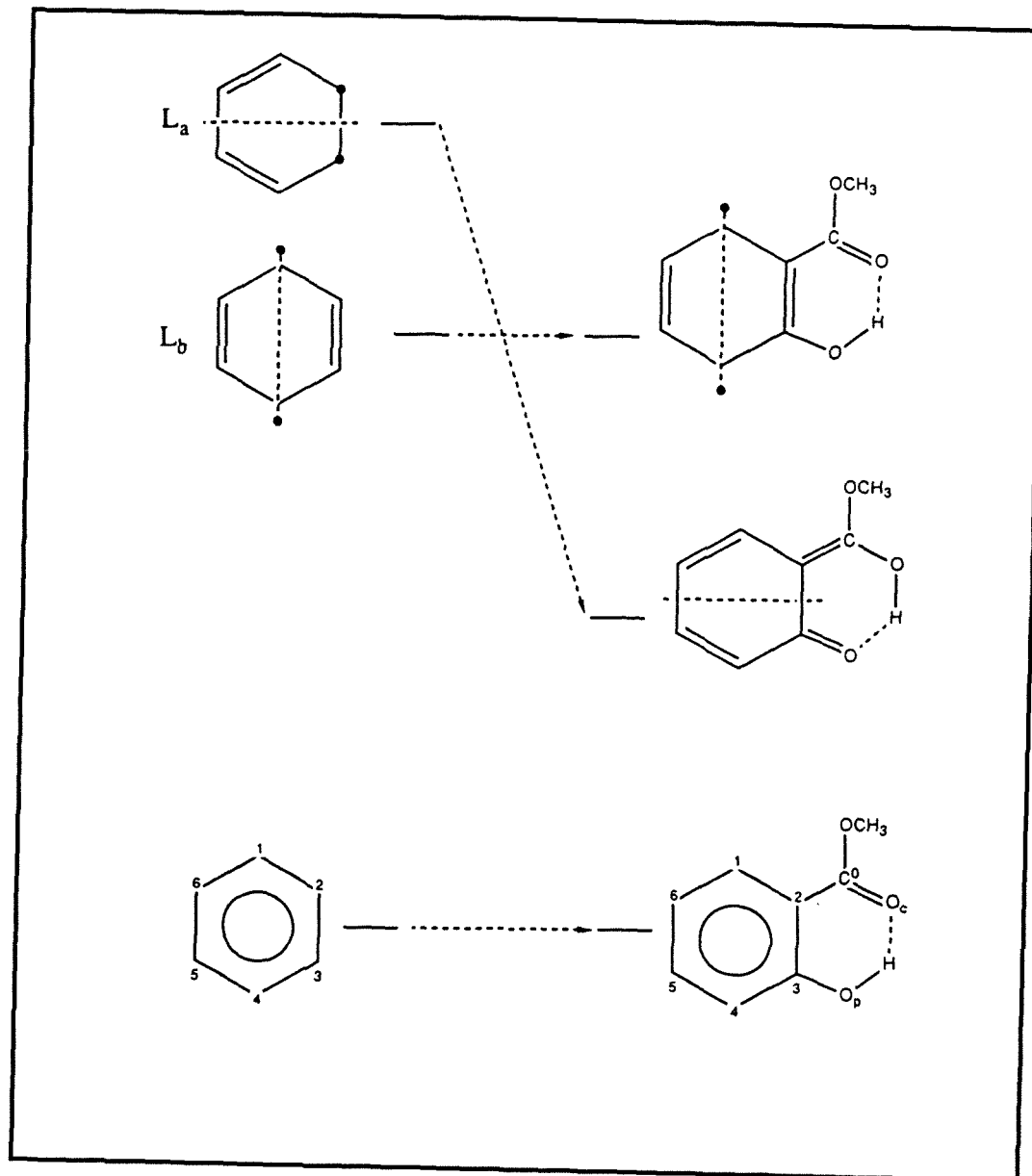

Figure 5.12 Nodal plane representation of the MO-based rationalization for excited-state tautomerization, as derived by Nagaoka et al.[4]

Recently, a new description of the excited state dynamics in MS and other intramolecularly hydrogen-bonded molecules has been proposed by Nagaoka and

Nagashima.[4] They assert that the nature of the mechanism may be inferred through consideration of the π-system molecular orbitals: The molecule is divided into three groups, the hydroxyl group, the carbonyl group, and the benzene ring. Of these, the benzene ring is the most stable. They then consider the wave functions of the ground and excited states of that individual piece (see Fig. 5.12). The two excited states of benzene, L_a and L_b, are formed by excitation of an electron from the HOMO to the LUMO, producing the biradicals as shown. The dashed lines represent the nodal planes running perpendicular to the molecular plane.

We now consider the complete MS molecule, the wave function of which largely resembles that of the benzene moiety. In state L_b, the lone electrons localized at C1 and C4 do not contribute to the C2–C0 and C3–O_p bonds, suggesting a keto configuration which is similar in energy to that of the corresponding benzene wave function. In state L_a, however, the lone electrons at C2 and C3 stabilize the substituents, facilitating the rearrangement of bonds to produce an enol structure with the hydrogen now shifted toward the carbonyl oxygen (though still intramolecularly bonded). This stabilization significantly lowers the energy of the biradical benzyl wave function, thus in the excited state of MS, the tautomer T* is preferred due to the favorable nodal pattern.

The concept is simple, and is supported by "*ab initio*" MO calculations including geometry optimizations of the ground and first excited states in an analog of MS: *o*-hydroxybenzaldehyde. The optimized geometry of the excited state is consistent with the enol configuration in which the intramolecularly bonded hydrogen is slightly displaced toward the carbonyl oxygen. In these calculations, the hydrogen atom is shown to move toward the carbonyl oxygen by ~0.02 Å upon excitation,[4a] an order of magnitude less than previous estimates.[18] In addition, the O_p–H bond distance increases by only ~0.001 Å, whereas other bond distances and angles are changed significantly. These results are consistent with a molecular

tautomerization in which the structural reorganization is not localized, but rather encompasses other degrees of freedom.

A tautomerization would be temporally "instantaneous", as there is an electronic resonance in the aromatic system; thus, there is no large displacement of the hydrogen atom toward the carbonyl oxygen atom upon excitation. This intramolecular bond-electron redistribution is reminiscent of the A + BC chemical dynamics for which simultaneous bond breaking and formation take place. Only if there is an intermediate at a certain nuclear displacement would the system live for longer times than picoseconds. IVR and the nuclear motions "slow down" the dynamics as the system finds (or adjusts during) the reaction coordinate.
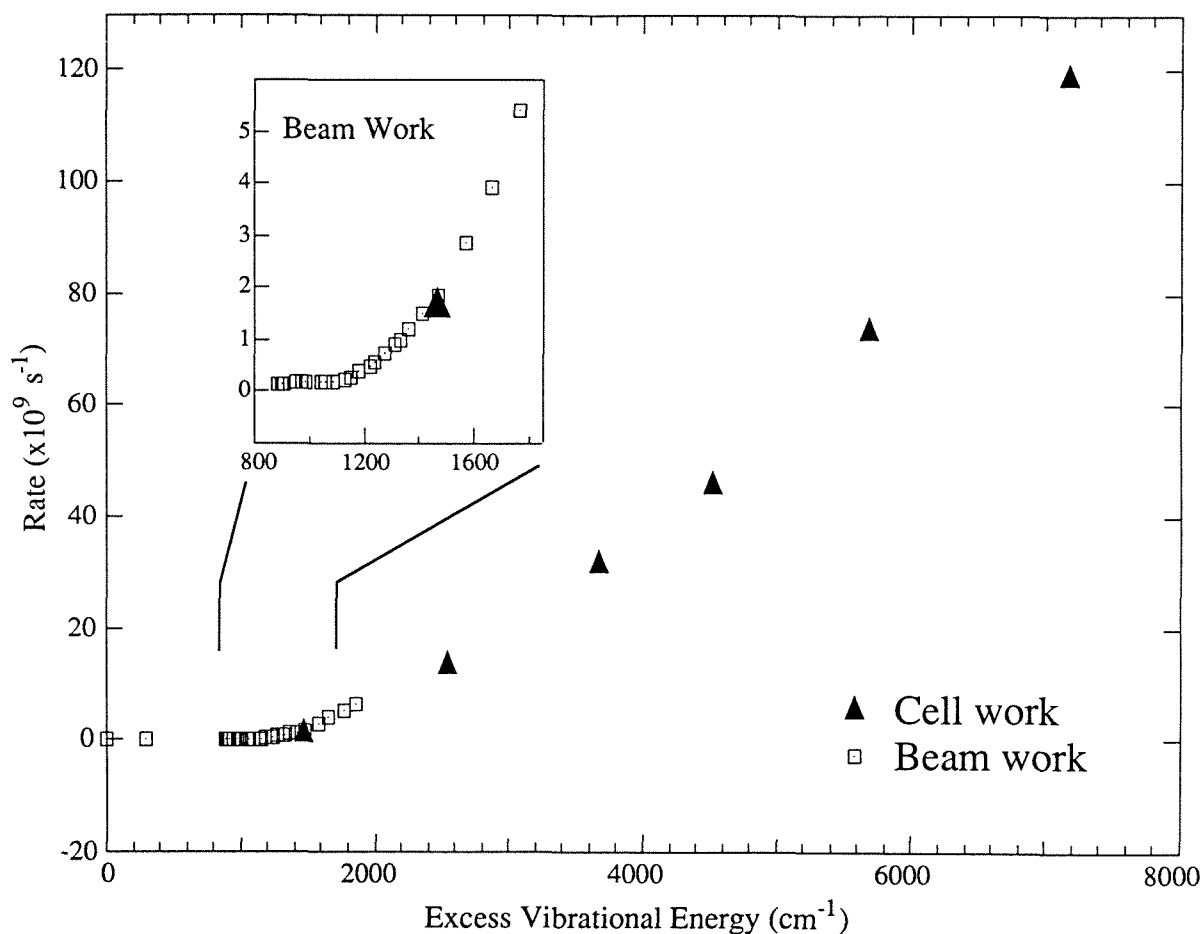

Figure 5.13 Decay rate *vs.* excess energy; monitoring the 440 nm emission. The open squares were obtained by Felker *et al.*[19] while the solid triangles represent current work. (Inset): Expanded region from 800–1800 cm^{-1}.

IV.B. *Nonradiative Decay of Hydrogen-transferred Species*

The marked increase of the observed blue decay rate at high excess energies indicates the existence of an efficient intramolecular nonradiative decay process. The picosecond time-resolved studies characterized this behavior in a molecular beam in the range of 0–1850 cm^{-1} of excess vibrational energy;[19] the current work extends this range to ~7160 cm^{-1} beyond the 0–0 transition, as shown in Fig. 5.13. A threshold energy of ~1300 cm^{-1} marks the onset of the nonradiative channel, in excellent agreement with the activation energy of this channel (15.5 kJ/mol) derived from temperature studies of MS in solution,[13] as well as the decrease in fluorescence quantum yield observed at about this energy.[18]

Dispersed fluorescence spectra of beam-cooled MS revealed a progression of a 180 cm^{-1} mode built on 0, 1690, and 3220 cm^{-1} shifts from the origin,[19] as mentioned above. Based on the phenomenological description of a localized hydrogen transfer between the phenolic and carbonyl groups (which are necessarily coplanar with the aromatic ring), Lopez-Delgado and Lazare inferred that the nonradiative decay results from a molecular motion which destroys the coplanarity.[17] An oscillation of the carbonyl group, for example, might couple the excited electronic state to a highly vibrationally excited ground state level, inducing an internal conversion and/or intersystem crossing.

Based on a similar barrier (~1200 cm^{-1}) found in the isomerization of stilbene,[44] Felker *et al.*[19] proposed that the onset may be due to the low frequency out-of-plane modes that are often present in "floppy" molecules like stilbene. High-resolution spectroscopic studies by Helmbrook *et al.*,[18] identified this low-frequency mode as belonging to the bridged "ring" containing the intramolecular hydrogen bond, however, they could not associate large-amplitude out-of-plane vibrations with the nonradiative decay (for discussion, see Ref. 18). In addition, they found that the

nonradiative rate depends solely on the excess vibrational energy, not on the excitation of the low-frequency mode.[18]

More recently, Nishiya et al., reported that when the methoxy group on the carbonyl is replaced by other ligands (such as H, CH_3, and NH_2), the low-frequency mode does not appear in the fluorescence spectrum, precluding its association with an out-of-plane bending motion,[23] although matrix effects may be a perturbation here. They suggested that the 180 cm^{-1} mode may be due to internal rotation of the methyl group. Independent of the assignment, if these low frequency modes are the promoting modes of nonradiative processes, then the decay is a reflection of inter-electronic state coupling involving the proximity[45] to nearby states (possibly $n\pi^*$ or ground state) or rovibronic couplings as in the channel-3 case of benzene.[46] However, there is another intriguing idea.

In the hydrogen-transferred form of MS, the nascent product is vibrationally hot and the intramolecular hydrogen bond is the weakest. If the effective temperature exceeds a threshold, the intramolecular hydrogen bond will break, leaving the entire moiety (including the methoxy group) "free" to move. Such a process requires a threshold of energy comparable to a typical hydrogen bond strength and because of the "rotation," a large density of states is accessible and helpful to IVR, which enhances the decay. The energy threshold (1300 cm^{-1}) is consistent with previous work[47] in which the minimum energy required for the dissociation of phenol-benzene hydrogen-bonded complex was found to be 1400 cm^{-1}, and is certainly typical of H-bond energies.[39c-e] For the isoquinoline-water hydrogen bond, the threshold was found to be at ~1000 cm^{-1}.[28a] The accelerated decay can then be understood by considering the increased effective density of states of free or hindered rotation and with methyl group effect on the spectra[48] and on the dynamics of IVR.[49] There is no significant isotope effect (MS–D), consistent with

motion above the barrier for this type of motion. IVR-induced decay is known in

other systems such as isoquinoline (IQ) and hydrogen bonded IQ–H_2O.[28a,50]
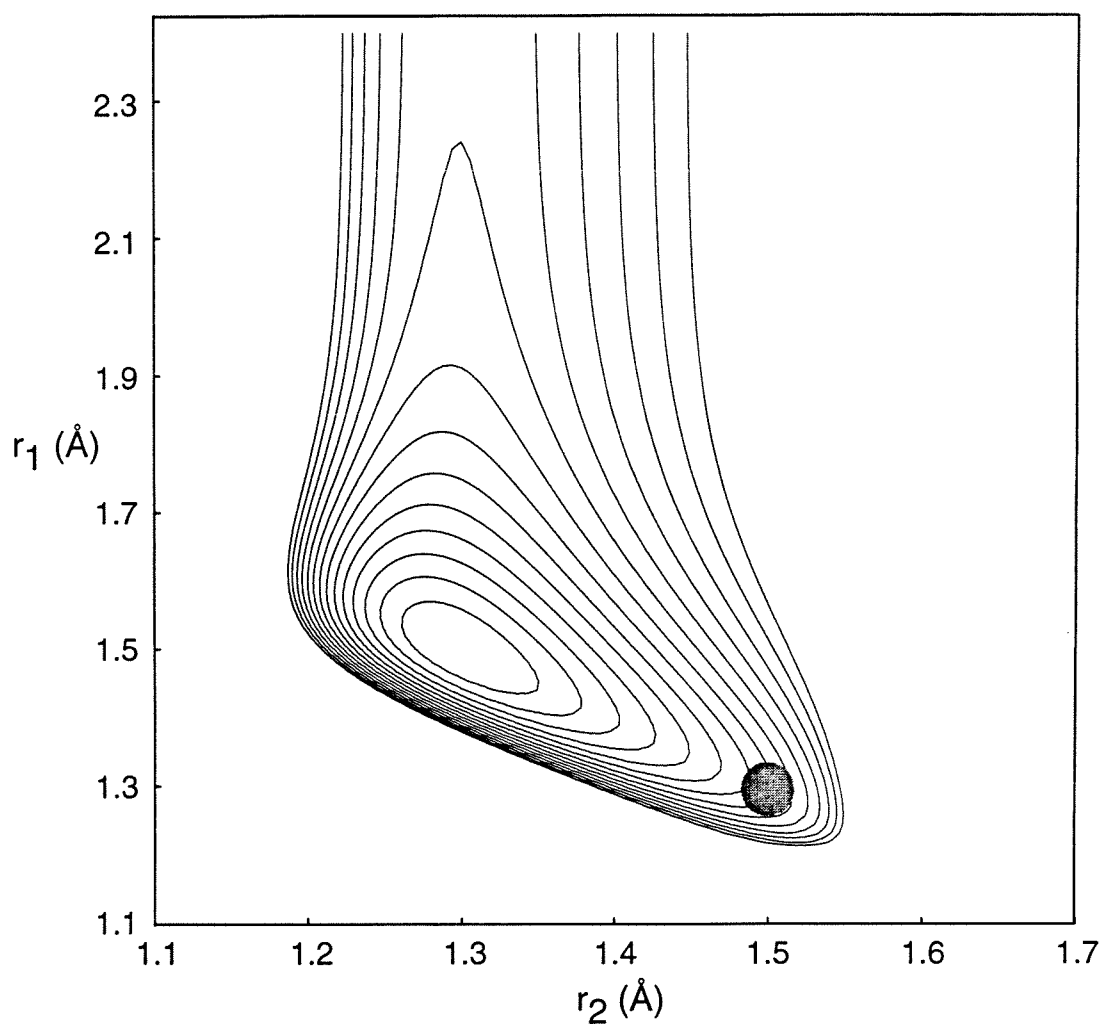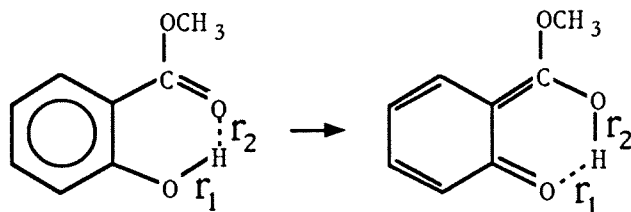

Figure 5.14 Schematic two-dimensional potential energy surface showing both the asymmetry in the potential and the exit barrier to the nonradiative channel. Depending on the total energy, a propagating wave packet (see circle) can either be trapped in the well or exit as the molecule "loses" the hydrogen-bond coordinate (see text).

The potential describing both the hydrogen transfer and the breakage (or rotation) of the intramolecular hydrogen bond is depicted in Fig. 5.14. In a frozen $O_a \cdots O_b$ configuration, the H motion is between the two oxygen atoms, and the potential is similar to that of Fig. 5.1, with the exception of the asymmetry established from the dynamics. In order to allow for other motions, we must relax this rigidity (away from r_1 and r_2) and let the oxygen (and other) nuclei change position adiabatically. In this case, it is possible to gain a new degree of freedom, *e.g.*, rotation of the OH, or a change in $O_a \cdots O_b$ position, hence leading to new channels. In Fig. 5.14, we represent the dynamics with a localized exit channel "dissociation" to globally describe the motion of the packet at different vibrational energies. At low energies, the packet moves exoergically toward the well and is trapped. At higher energies, the packet encounters an exit channel barrier, describing the nonradiative decay with the above stretch/rotation H–bond dissociation mechanism.

V. Conclusion

The dynamics of hydrogen atom transfer in the gas phase under collisionless conditions are studied using femtosecond depletion spectroscopy. We explore the dynamics from the early femtosecond times to the picosecond time scale, where the hydrogen-transferred species undergoes nonradiative decay. Within 60 fs, the wave packet in MS evolves to cover all configuration space along the reaction coordinate. We observe no deuterium isotope effect, consistent with ultrafast hydrogen movement.

The femtosecond dynamics indicate that intramolecular bond-electron rearrangement involves the molecular framework (nuclear motion and IVR); this process is similar to the case of A + BC reactions where bond breakage and bond

formation occur simultaneously. The potential of the motion is highly asymmetric along the O–H⋯O reaction coordinate. This potential asymmetry, generic to many of these hydrogen- atom transfer reactions, leads to wave packet motion on a time scale only comparable to the half period of the low frequency modes, but an order of magnitude slower than the OH reaction coordinate period.

The hydrogen-transferred configuration is observed to undergo a nonradiative decay which depends on the total vibrational energy with a barrier of 1300 cm^{-1}; decay rates were measured up to 7160 cm^{-1}. These observations are related to IVR and to the dissociation (decay) channel linked to the intramolecular-hydrogen bonding. From the dynamics on the femtosecond and picosecond time scales, we deduce the changes in bonding and the associated potential. It would be useful to extend these studies to other interesting system[51] in a molecular beam.

References

1 M. Kasha, J. Chem. Soc. Faraday Trans. 2 **82,** 2379 (1986).

2 R. Hoffmann and R. B. Woodward, J. Am. Chem. Soc. **87,** 2046 (1965); *The Conservation of Orbital Symmetry* (Academic, New York, 1970).

3 H. Fujimoto and K. Fukui, *Advances in Quantum Chemistry,* Vol. 6, edited by P. O. Löwdin (Academic, New York, 1972); K. Fukui, Angew. Chem. Int. Ed. Engl. **21,** 801 (1982); R. G. Pearson, Acc. Chem. Res. **4,** 152 (1971).

4 (a) S. Nagaoka, U. Nagashima, N. Ohta, and S. Katsumata, Chem. Phys. **136,** 153 (1989); (b) S. Nagaoka, U. Nagashima, N. Ohta, and T. Takemura, J. Phys. Chem. **92,** 166 (1988); (c) S. Nagaoka and U. Nagashima, *ibid.* **94,** 1425 (1990); (d) U. Nagashima, S. Nagaoka, and S. Katsumata, *ibid.* **95,** 3532 (1991); (e) S. Nagaoka and U. Nagashima, *ibid.* **95,** 4006 (1991).

5 D. R. Herschbach, Angew. Chem. Int. Ed. Engl. **26,** 1221 (1987).

6 J. K. M. Marsch, J. Chem. Soc. **125,** 418 (1924).

7 A. Weller, Z. Elektrochem. **60,** 1144 (1956); Prog. React. Kinet. **1,** 188 (1961).

8 R. D. Rauh, Ph.D. thesis, Princeton University, 1972.

9 P. J. Kovi, C. L. Miller, and S. G. Schulman, Anal. Chim. Acta **61,** 7 (1972).

10 W. Klöpffer and G. Naundorf, J. Lumin. **8,** 457 (1974); W. Klöpffer and G. Kaufmanm, J. Lumin. **20,** 283 (1979).

11 J. Catalán and J. I. Fernandez-Alonso, J. Mol. Struct. **27,** 59 (1975); J. Catalán and F. Tomas, Adv. Mol. Relaxation Processes **8,** 87 (1976).

12 K. Sandros, Acta Chem. Scand., Ser. A **30,** 761 (1976).

13 K. K. Smith and K. J. Kaufmann, J. Phys. Chem. **82,** 2286 (1978).

14 J. Goodman and L. E. Brus, J. Am. Chem. Soc. **100,** 7472 (1978).

15 D. Ford, P. J.Thistlewaite, and G. J. Woolfe, Chem. Phys. Lett. **69,** 246 (1980).

16 (a) A. U. Acuña, F. Amat-Guerri, J. Catalán, and F. González-Tablas, J. Phys. Chem. **84,** 629 (1980). (b) A. U. Acuña, J. Catalán, and F. Toribio, *ibid.* **85,** 241 (1981). (c) J. Catalán, F. Toribio, and A. U. Acuña, *ibid,* **86,** 303

(1982). (d) F. Toribio, J. Catalán, F. Amat-Guerri, and A. U. Acuña, *ibid.* **87,** 817 (1983). (e) A. U. Acuña, F. Amat-Guerri, F. Toribio, and J. Catalán, J. Photochem. **30,** 330 (1985).

[17] R. Lopez-Delgado and S. Lazare, J. Phys. Chem **85,** 763 (1981).

[18] L. Helmbrook, J. E. Kenny, B. E. Kohler, and G. W. Scott, J. Chem. Phys. **75,** 5201 (1981); J. Phys. Chem. **87,** 280 (1983).

[19] P. M. Felker, W. R. Lambert, and A. H. Zewail, J. Chem. Phys. **77,** 1603 (1982).

[20] S. Nagaoka, N. Hirota, M. Sumitani, K. Yoshihara, E. Lipczynska-Kochany, and H. Iwanura, J. Am. Chem. Soc. **106,** 6913 (1984).

[21] W. H. Orttung, G. W. Scott, and D. Vosooghi, J. Mol. Struct. **109,** 161 (1984).

[22] M. Sánchez-Cabezudo, J. L. G. D. Paz, J. Catalán, and F. Amat-Guerri, J. Mol. Struct. **131,** 277 (1985).

[23] T. Nishiya, S. Yamauchi, N. Hirota, M. Baba, and I. Hanazaki, J. Phys. Chem. **90,** 5730 (1986).

[24] M. M. Radhi and M. F. El-Bermani, Spectrochemica Acta **46A,** 33 (1990).

[25] E. Orton, M. A. Morgan, and G. C. Pimentel, J. Phys. Chem. **94,** 7936 (1990).

[26] T. Carrington and W. H. Miller, J. Chem. Phys. **84,** 4364 (1986).

[27] See, *e.g.*, P. F. Barbara and H. P. Trommsdorf, Chem. Phys. **136,** 2 (1989); P. F. Barbara, P. K. Walsh, and L. E. Brus, J. Phys. Chem. **93,** 29 (1989); P. F. Barbara, G. C. Walker, and T. P. Smith, Science **256,** 975 (1992); P. F. Barbara, P. M. Rentzepis, and L. E. Brus, J. Am. Chem. Soc. **102,** 2786 (1980); T. Elsaesser, W. Kaiser, and W. Lüttke, J. Phys. Chem. **90,** 2901 (1986).

[28] See, *e.g.*, (a) P. M. Felker and A. H. Zewail, J. Chem. Phys. **78,** 5266 (1983); (b) O. Cheshnovsky and S. Leutweiler, *ibid.* **88,** 4127 (1988); (c) R. Knochenmuss, O. Chesnovsky, and S. Leutwyler, Chem. Phys. Lett. **144,** 317 (1988); (d) T. Droz, R. Knochenmuss, and S. Leutwyler, J. Chem. Phys. **93,** 4520 (1990); (e) J. J. Breen, L. W. Peng, D. M. Willberg, A. Heikel, P. Cong, and A. H. Zewail, *ibid.* **92,** 805 (1990). (f) T. C. Swinney and D. F. Kelley, J. Phys. Chem. **95,** 2430 (1991); (g) J. A. Syage and J. Steadman, J. Chem. Phys. **95,** 2497 (1991); (h) S. K. Kim, S. Li, and E. R. Bernstein, *ibid.* **95,** 3119 (1991).

[29] Note that the actual excess energy does not simply correspond to $E_{pu} - E_{00}$ (where $\lambda_{00} = 332.7$ nm),[18] but rather must include the thermal vibrational

energy of the ground state MS. The frequencies of the fifty one vibrational modes were compiled from various sources[24,25] and the average vibrational energy as a function of temperature was calculated according to

$$E_{vib} = \Sigma_{i=1}^{3n-6} h\nu_i / \left[\exp(h\nu_i / kT) - 1 \right]$$

At 38°C, for example, the average thermal vibrational energy is ~1250 cm^{-1}.

[30] M. J. Cote, J. F. Kauffman, P. G. Smith, and J. D. McDonald, J. Chem. Phys. **90**, 2865 (1989); T. C. Corcoran, L. L. Connell, G. V. Hartland, P. W. Joireman, R. A. Hertz, and P. M. Felker, Chem. Phys. Lett. **170**, 139 (1990).

[31] Y. Chen, L. Hunziker, P. Ludowise, and M. Morgen, J. Chem. Phys. **97**, 2149 (1992).

[32] R. M. Bowman, M. Dantus, and A. H. Zewail, Chem. Phys. Lett. **161**, 297 (1989); R. M. Bowman, M. Dantus, and A. H. Zewail, Chem. Phys. Lett. **174**, 546 (1990).

[33] The I_2 transients show oscillatory behavior due to the probing of molecular vibrations (see Ref. 32 for more details). These oscillations were much less pronounced (pump laser 610 nm) in the present work (at the depletion power used) most likely due to absorption from both turning points. There was no measurable distortion in the transients, especially in the rise, at these powers.

[34] Notice that both MS depletion transients were measured in a sequence using the same cell and same pump and probe lasers; the only change was in the position of the monochromator grating (330 vs. 440 nm detection). The transients did not show any relative shift, *i.e.* both MS transients display time-zero at exactly the same position. The time-zero of the I_2 610/(340)/305 signal could not be compared with that of MS, as it required using a different cell. Therefore, we shifted the I_2 transient such that both (I_2 and MS) coincide, where time-zero has been set at half of the rise.

[35] G. Roberts and A. H. Zewail, J. Phys. Chem. **95**, 7973 (1991).

[36] P. Cong, A. Mokhtari, and A. H. Zewail, Chem. Phys. Lett. **172**, 109 (1990).

[37] R. Bersohn and A. H. Zewail, Ber. Bunsenges Phys. Chem. **92**, 373 (1988).

[38] V. I. Goldanskii, Ann Rev. Phys. Chem. **27**, 85 (1976).

[39] See, *e.g.*, (a) R. Schroeder and E. R. Lippincott, J. Phys. Chem. **61**, 921 (1957); (b) R. L. Somorjai and D. F. Hornig, J. Chem. Phys. **36**, 1980 (1962); (c) Th. Arthen-Engeland, T. Bultmann, N. P. Ernsting, M. A. Rodriguez, and W. Thiel, Chem. Phys. **163**, 43 (1992); (d) G. C. Pimentel, *The Hydrogen Bond*

(Reinhold, New York, 1960); (e) *Hydrogen Bonding*, edited by S. N. Vinogradov and R. H. Linnell (Van Nostrand Reinhold, New York, 1971); (f) *Hydrogen Bonds*, edited by P. Schuster (Springer-Verlag, Berlin, 1984).

[40] Using a normal mode analysis (see p. 72 of *Mechanics, 3rd ed.*, L.D. Landau and E.M. Lifshitz (Pergamon Press, Oxford, 1976) for and O–H⋯O antisymmetrical vibration, the frequency is $\sim\sqrt{2}$ times greater than that of an O–H vibration alone.

[41] F. Laermer, T. Elsaesser, and W. Kaiser, Chem. Phys. Lett. **148**, 119 (1988).

[42] Work in this laboratory on the isomerization of stilbene: S. Pedersen, L. Bañares, and A. H. Zewail, J. Chem. Phys. **97**, 8801 (1992).

[43] Note that the absorption spectrum extends to more energies than the excitation spectrum due to nonradiative decay reflected in the latter (see Fig. 5.3).

[44] J. A. Syage, P. M. Felker, and A. H. Zewail, J. Chem. Phys. **81**, 4706 (1984); L. Bañares, A. A. Heikal, and A. H. Zewail, *ibid.* **96**, 4127 (1992).

[45] E. C. Lim, in *Excited States*, Vol. 3, edited by E. C. Lim (Academic, New York, 1977), p. 305.

[46] U. Schubert, E. Riedle, H. J. Neusser, and E. W. Schlag, J. Chem. Phys. **84**, 6182 (1986).

[47] J. L. Knee, L. R. Khundkar, and A. H. Zewail, J. Chem. Phys. **87**, 115 (1987).

[48] For an excellent review, see, M. Ito, J. Phys. Chem. **91**, 517 (1987).

[49] C. S. Parmenter and B. M. Stone, J. Chem. Phys. **84**, 4710 (1986); **86**, 51 (1987). J. S. Baskin, T. S. Rose, and A. H. Zewail, *ibid.* **88**, 1458 (1988).

[50] J. L. Knee, L. R. Khundkar, and A. H. Zewail, J. Phys. Chem. **89**, 3201 (1985); P. M. Felker and A. H. Zewail, Chem. Phys. Lett. **94**, 454 (1983).

[51] M. Lee, Y. T. Yardley, and R. M. Hochstrasser, J. Phys. Chem. **91**, 4621 (1987), and references therein; B. J. Schwartz, L. A. Peteanu, and C. B. Harris, *ibid.* **96**, 3591 (1992); A. Ito, Y. Fujiwara, and M. Itoh, J. Chem. Phys. **96**, 7474 (1992), and references therein.

Application to Atmospheric Chemistry

Femtosecond spectroscopy has proven its utility in piecing together mechanistic puzzles by directly tracking the evolution of chemical reactions. The extension to studies of atmospheric reactions is not only natural, but timely and appropriate, given the urgency surrounding our need for thorough understanding of mechanisms related to stratospheric ozone depletion.
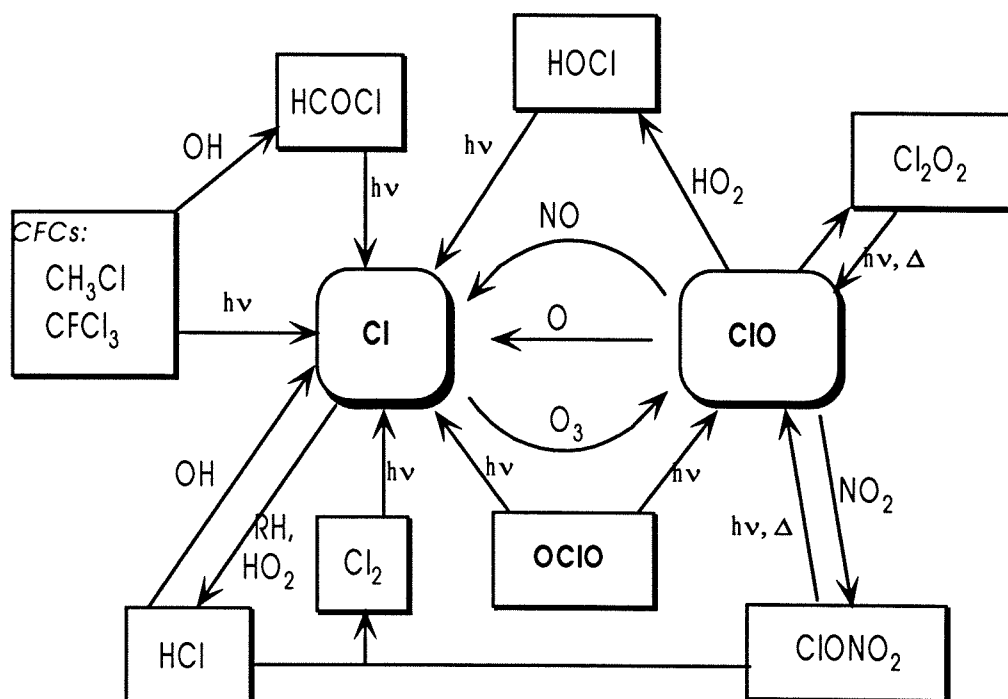

Figure 1 Transformation pathways of chlorine species in the stratosphere. Adapted from Ref. 1.

The release of CFCs and halogen-containing compounds has had a profound impact on stratospheric ozone concentrations,[2] the most dramatic manifestation of which is the appearance of Antarctic ozone "holes" (for review, see Ref. 3). Participation of halogen oxides, especially ClO and BrO, IS central to the underlying chemistry.[1] The atmospheric chemistry of ClO is inextricably linked to related species such as OClO, $ClONO_2$, and the dimer Cl_2O_2 (see Fig. 1). Laboratory studies of these important species can provide insight into the chemical transformations occurring in the stratosphere. Specifically, detailed knowledge of reaction kinetics and dynamics, product channels, and branching ratios for the possible interactions is required for realistic interpretations and modeling of the associated mechanisms.

Until recently,[4,5] OClO was believed to play no role in stratospheric ozone depletion, despite its presence in high concentrations. The photodissociation of OClO was thought to only involve formation of oxygen atoms, which would subsequently react with molecular oxygen to form ozone:

$$OClO + h\nu \rightarrow ClO + O \qquad (1)$$

$$O + O_2 \rightarrow O_3 \qquad (2)$$
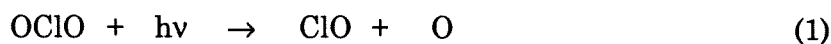
As such, the photodissociation of OClO does not result in any net loss of O_3. However, other photochemical pathways have been identified[4] in which OClO fragments to form reactive Cl atoms which may attack ozone directly:

$$OClO + h\nu \rightarrow Cl + O_2 \qquad (3)$$

$$Cl + O_3 \rightarrow ClO + O_2 \qquad (4)$$
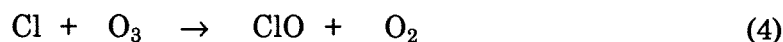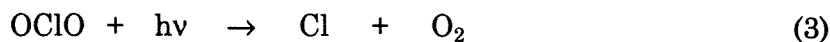
The discovery of a dissociation path to Cl and O_2 therefore links the photochemistry of OClO to ozone depletion.

The overall role of OClO in affecting stratospheric processes leading to ozone depletion is not entirely known. Current efforts are combining the results of photochemical studies, spectroscopy (gas phase, liquid solution, and matrices), and theoretical calculations of the ground and excited-state potential energy surfaces to establish the reactivity and mechanism of OClO (for recent review, see Refs. 1,5,6). Chapter 6 presents femtosecond studies of the photodissociation of OClO.[7] The reaction trajectories are found to involve both ionic and neutral channels, leading to both ClO + O and Cl + O_2 products. The time scales for decay into the two channels are measured, and the results are related to dynamics upon the potential energy surfaces as well as the overall mechanism.

References

1   R. P. Wayne, G. Poulet, P. Biggs, J. P. Burrows, R. A. Cox, P. J. Crutzen, G. D. Hayman, M. E. Jenkin, G. L. Bras, G. K. Moortgat, U. Platt, and R. N. Schindler, Atmos. Environ. **29,** 2677 (1995).

2   M. J. Molina and F. S. Rowland, Nature **249,** 810 (1974).

3   R. S. Stolarski, Scientific American **258,** 30 (1988).

4   V. Vaida, S. Solomon, E. C. Richard, E. Ruehl, and A. Jefferson, Nature **342,** 405 (1989).

5   V. Vaida and J. D. Simon, Science **268,** 1443 (1995).

6   J. W. Waters, Engineering & Science 3 (1993).

7   T. Baumert, J. L. Herek, and A. H. Zewail, J. Chem. Phys. **99,** 4430 (1993).

6. Chlorine Dioxide*

In this chapter, femtosecond studies of the photodissociation of OClO are presented. The observed dynamics of the OClO parent species as well as the reactive intermediates involved in its decay are related to a fragmentation mechanism involving two channels. The dynamics of the fragmentation reveal the nuclear motion and the electronic coupling between potential energy surfaces. The time scale for bond breakage is in the range of 300–500 fs, depending on the excitation energy; surface crossing to form new intermediates is a pathway for the two channels of fragmentation: ClO + O (primary) and Cl + O_2 (secondary). Comparisons with results of *ab initio* calculations are made.

The gas phase photodissociation mechanisms of OClO in the near-UV region have stimulated copious experimental and theoretical studies (for recent references, see 1-13), in part due to its possible role in the depletion of ozone in the Antarctic stratosphere.[14] The absorption spectrum[15,16] of OClO ($A^2A_2 \leftarrow X^2B_1$) spans from 475 nm to 273 nm (Fig. 6.1). At all absorption wavelengths, the major dissociation channel is found to be

$$OClO\ (A^2A_2)\ \rightarrow\ ClO\ (X^2\Pi,\ v'')\ +\ O\ (^3P) \tag{1}$$
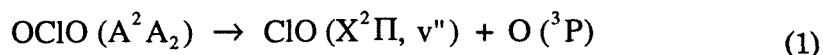
whereas a minor channel is

$$OClO\ (A^2A_2)\ \rightarrow\ Cl\ (^2P)\ +\ O_2\ (^3\Sigma_g^-,\ ^1\Delta_g,\ ^1\Sigma_g^+)\ . \tag{2}$$
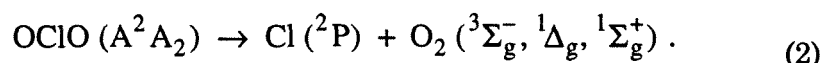
Since the O atom formed in reaction (1) could react with O_2 molecules in the atmosphere to produce O_3, this dissociation pathway would lead to a null cycle in stratospheric ozone depletion. Reaction (2), however, represents a mechanism for halogen-catalyzed conversion of O_3 to O_2. To understand the photodissociation mechanism of OClO, different experimental techniques have been applied.

In describing the elementary nuclear motions of OClO fragmentation, three coordinates must be considered: the symmetric stretch v_1, the bend v_2, and the asymmetric stretch v_3 (see Table I). Generally, for a given bend configuration, a wave packet on a single potential energy surface (PES) will evolve along the reaction coordinate from the bound symmetric stretch region of the PES (Fig. 6.2). Since the pump is not energetically broad enough to span levels of v_1, a localized wave packet is not created along the symmetric stretch coordinate. If a wave packet could be generated, the problem becomes analogous to the case of HgI_2, where coherent nuclear motion (Fig. 6.3) to yield HgI + I was observed and studied.[17-19] For OClO, the problem is more complicated, however, due to the fact that several nearby potentials may be involved.

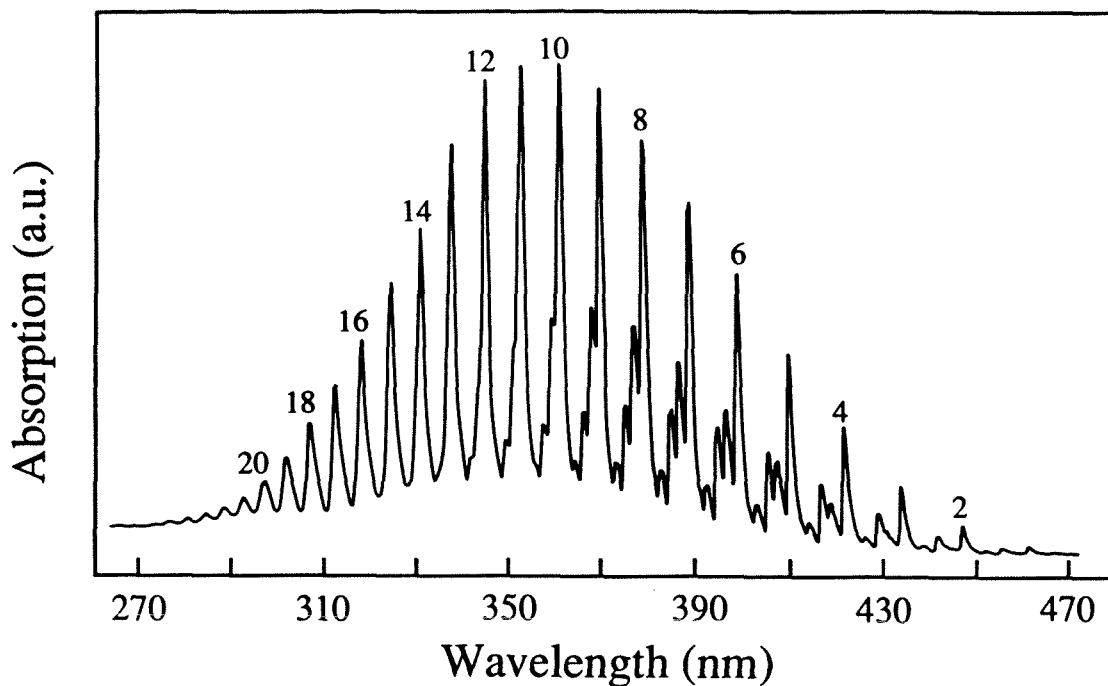**Figure 6.1** The medium-resolution absorption spectrum of OCIO, from Ref. 16. Assignments are taken from Ref. 15.
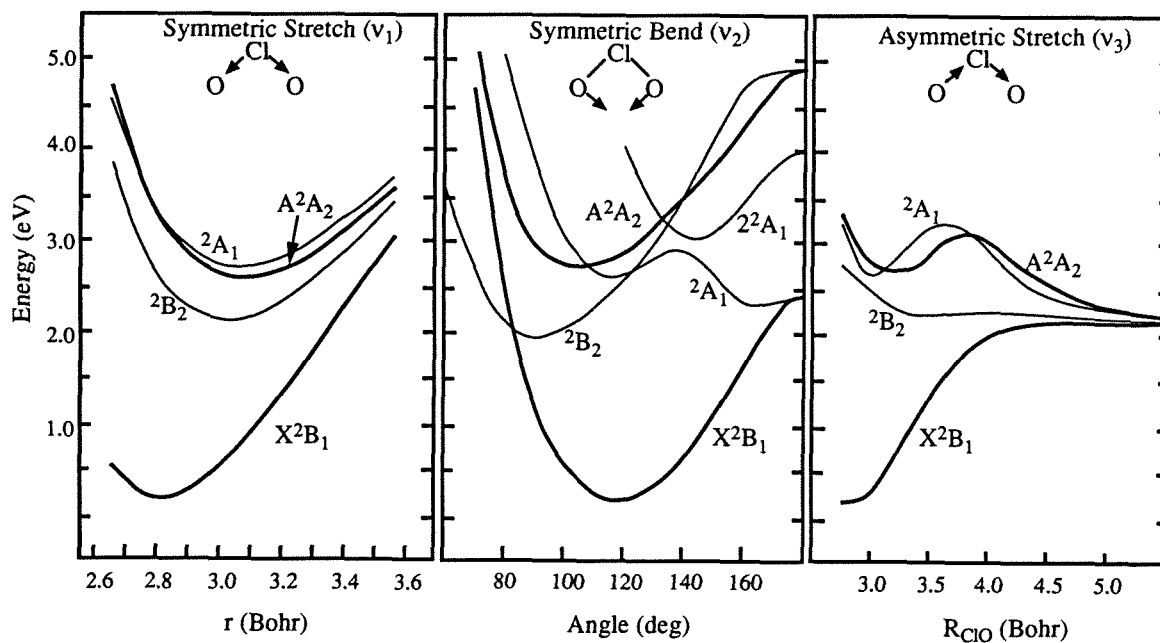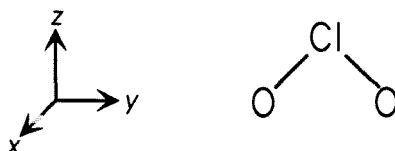

Figure 6.2 Cuts through "ab initio" potential energy surfaces from Ref. 12. All symmetry notations are for C_{2v} geometry. The symmetric stretch potential is shown for a fixed valence angle of 106.4° (calculated A^2A_2 equilibrium angle; experimental value: 106.2°). (1 Bohr = 0.529 Å)

Table 6.1 OClO in C_{2v} geometry.

State	Frequency $\overline{\nu}$ (cm^{-1}): [Period (fs)]:	ν_1	ν_2	ν_3	T_e (eV)	Ref.
X^2B_1		963.5 [35]	451.7 [74]	1123.0 [29]		a
$^2B_2$		815.0 [41]	319.5 [104]	520 [64]	1.98	b
$^2A_1$		696.5 [48]	311.3 [107]	1474 [23]	2.60	b
A^2A_2		713.2 [47]	287.1 [116]	401.5 [83]	2.68	c

Symmetry of Normal Vibrations

Symmetric Stretch (ν_1)	a_1
Bend (ν_2)	a_1
Asymmetric Stretch (ν_3)	b_2

Electric Dipole Selection Rules

$A^2A_2 \leftarrow X^2B_1$	Parallel polarized
$^2A_1 \leftarrow X^2B_1$	Perpendicular polarized
$^2B_2 \leftarrow X^2B_1$	Forbidden

Allowed pairs of electronic states for vibronic coupling

$A_2 - B_1$
$A_1 - B_2$

[a]Taken from Ref. 20.
[b]Taken from Ref. 12.
[c]Vibrational constants were derived from Ref. 9. T_e was derived from Refs. 12 and 20.
[d]For rotations, see Ref. 21.
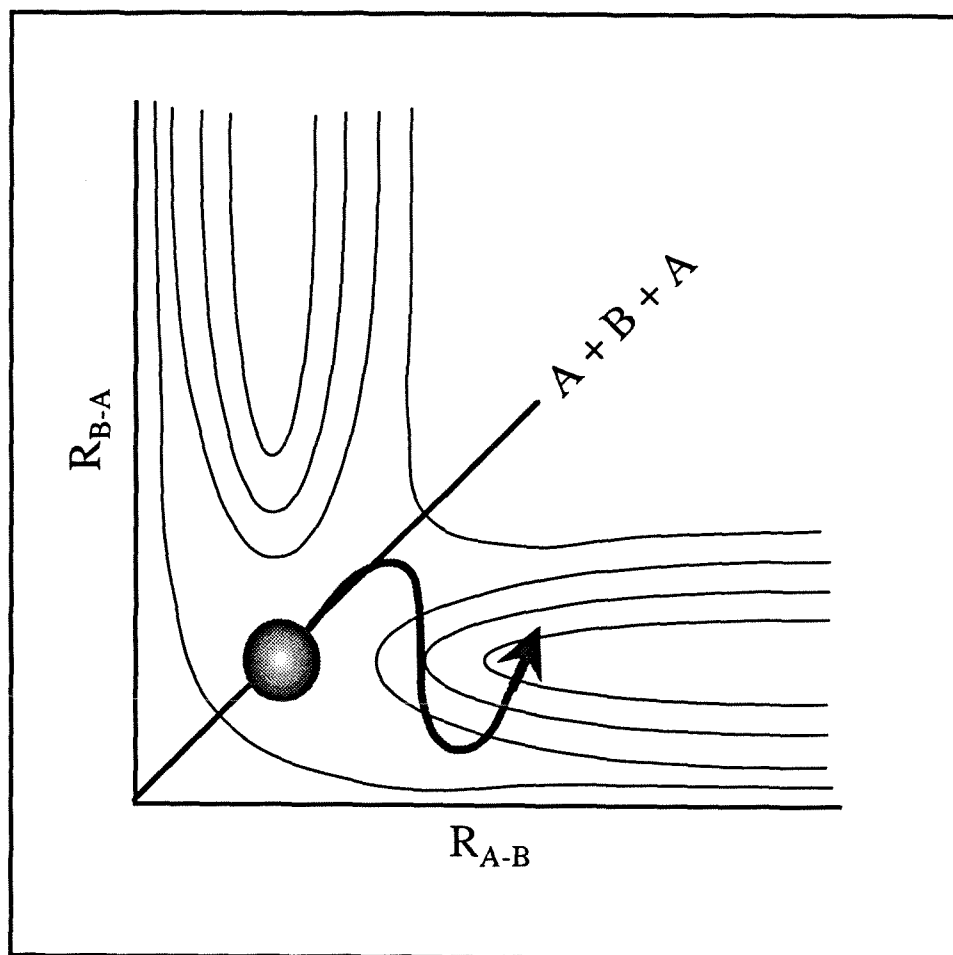
Figure 6.3 Schematic of an ABA potential energy surface. The filled circle represents the localized wave packet that moves with a wide oscillatory motion into the asymmetric stretch dissociation channel to form AB + A (OClO and IHgI cases discussed in text).

In this chapter, studies of the ultrafast dynamics of OClO elementary fragmentation using the techniques of femtosecond transition-state spectroscopy are presented. Of particular relevance is the use of multi-photon ionization and mass spectrometry[22-26] which makes it possible to observe the parent ion of OClO (*i.e.* OClO$^+$), hitherto undetected by all previous nanosecond experiments. We follow the initial nuclear motion and measure the real-time dissociation to different fragments. In the range of $v_1 = 11$ to 17, bond breakage times are typically 300 fs to 500 fs while the initial decay ranges from 30 fs to 120 fs. We relate these

observations to the nature of the dynamics and to recent *ab initio* calculations of the PESs. We also report results on the detection of one of the fragments (ClO) and preliminary studies of OClO when selectively solvated with water.

Background

In the high resolution absorption spectra of OClO by McDonald and Innes[3] and Michielson *et al.*,[2] the rotational structure of the symmetric-stretch progression was investigated for v_1 = 1–5. It was found that the rate of "predissociation" (*vide infra*) depends on the spin state prepared: the rate is greater for the F_1 ($J = N + 1/2$) state than for the F_2 ($J = N - 1/2$) state and is independent of the rotational state of the initially-excited molecule. In addition, it was found that for $v_1 < 3$, the rate of predissociation from the states (v_1 0 0) is independent of v_1, but for $v_1 > 3$, the rate increases with v_1. For example, the lifetime of the F_1 component in the (0 0 0) state is given to be 67 ± 14 ps, while for the (5 0 0) band, 28 ± 1 ps is reported.[2] It is further noted that the bending mode shows faster predissociation rates at comparable energies. According to the two-dimensional cuts through the *"ab initio"* PESs along the symmetric stretch, bend, and asymmetric stretch coordinates calculated by Peterson and Werner[12] (Fig. 6.2), the system is bound along the first two and unbound along the asymmetric stretch.

Direct vibronic coupling of the $^2A_2$ state to the close lying $^2B_2$ and $^2A_1$ states is forbidden for this triatomic in C_{2v} symmetry, while allowed to the $^2B_1$ ground state.[27] McDonald and Innes[3] have argued that it is unlikely that the $^2B_1$ ground state couples with the prepared A^2A_2 state, as the observed vibrational and spin dependence of the rotational line widths could not be reasonably explained by such coupling of the excited manifold. As the bending mode is promoting the predissociation and the $^2B_2$ state is strongly bent (Fig. 6.2), Michielsen *et al.*[2] and McDonald and Innes[3] concluded that the A^2A_2 state mixes with the $^2B_2$ state by

spin-orbit coupling before proceeding to dissociation. Recent calculations by Peterson and Werner[12] of the PES and a closer analysis of the possible excited-state interactions with respect to symmetric stretch, bend, and asymmetric stretch coordinates, prefer the $^2A_1$ state as the state from which the predissociation proceeds.

Vaida and co-workers[10] provided the analysis of rotational line broadening involving $(v_1\ 0\ 0)$, $(v_1\ 1\ 0)$, and $(v_1\ 0\ 2)$ bands of OClO, extending the range from $v_1 =$ 4 - 10. The absorption spectrum was measured directly using jet-cooled Fourier transform ultraviolet spectroscopy.[4,9] They observed an increase in (fitted) rotational line widths, and thus a decrease in the corresponding lifetimes from about 20 ps at (5 0 0), to about 4 ps at (10 0 0) (see Fig. 3 in Ref. 10). In studying modes involving bending excitation, line widths were found to be 4 to 5 times broader than for the symmetric stretch alone at the same energy. It was also found that combinations involving v_1 with $2v_3$ broaden more rapidly than combinations of v_1 with v_2. The experimental observations were explained via interactions of the A^2A_2 state with both the $^2A_1$ and $^2B_2$ states, analogous to the earlier work of McDonald and Innes[3] and Michielsen *et al.*[2] In the excitation region higher than v_1 = 10, it is reported that the line widths appear to reach a limit and become fairly constant with lifetimes. A more detailed analysis of rotational line width broadening is not given in this energy region, as the individual rotational line widths become too broad and thus only the rotational envelopes are discernible (Fig. 6.4). Estimates of the lifetimes, however, are given at 303 nm (v_1 between 18 and 19) to be ~1 ps, and for the $v_3 = 4$ level at 333 nm, line widths of ~100 cm^{-1} (~50 fs) were reported with the note that these bands are disappearing into noise.[14]

Experiments involving ns-laser REMPI techniques have also been reported: Vaida's group recorded spectra in the range from 335 to 370 nm which focused on the ClO^+ and Cl^+ channel,[7] however, the parent $OClO^+$ was not seen.[13] Ionization

and fragmentation are two competing channels and with ns pulses, "channel switching," discussed by Schlag and Neusser[28] and Taylor and Johnson,[29] can lead to ionization of fragments and not of the parent neutral. Such behavior has previously been demonstrated in methyl iodide[30,31] where the CH_3I^+ and fragment I^+ were observed to vary in intensity depending on the delay time between the pump and MPI pulses. Another example comes from the work of Gerber's group[32] on Na_n cluster resonances. When, for example, n > 4, the absorption spectra of the Na_n clusters could not be measured directly by ns-laser REMPI techniques due to the fast fragmentation processes of the excited intermediate states. However, fs-laser REMPI techniques were successful in observing these resonances as well as determining the lifetimes of the intermediate states directly in the time domain via pump-probe experiments. The product analysis in Vaida's group's work[7] indicated that for the O (^3P) + ClO (X $^2\Pi$) fragmentation, the ClO molecules were released vibrationally excited ($v'' = 3 - 6$).
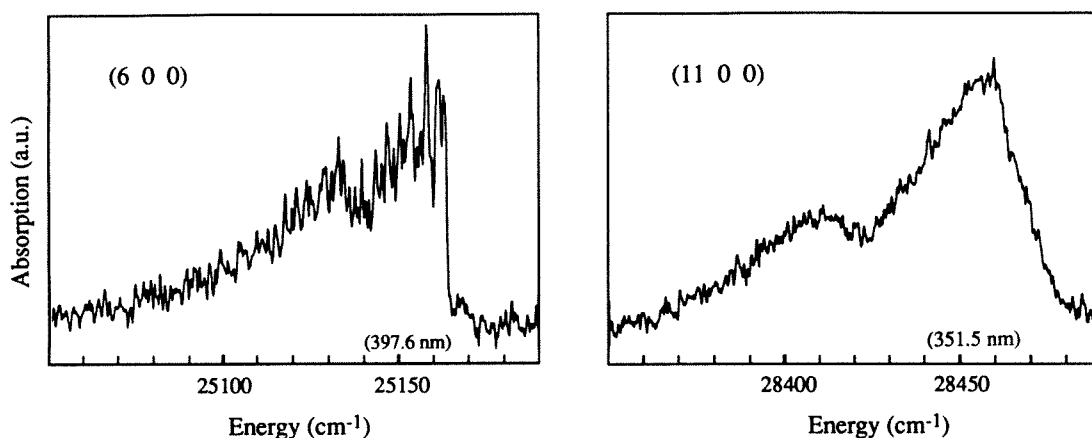
Figure 6.4 High-resolution spectra of (6 0 0) band and (11 0 0) band from Ref. 4. At the (6 0 0) band, there are resolved rotational structures. For these bands, contours were fitted to give estimates of the lifetimes. The two peaks in the (11 0 0), and also (6 0 0), are due to the two Cl isotopes.

They also observed Cl^+ REMPI action spectra in the region 360–363 nm and attributed this observation to an isomerization of OClO to ClOO, which

subsequently dissociates to Cl + O_2. The quantum yield for Cl formation was reported by Lawrence *et al.*[6] to be less than 5×10^{-4} between 359 and 368 nm, an upper limit as they did not actually observe Cl + O_2. A further REMPI experiment was reported by Bishenden *et al.*[8] who used a tunable dye laser to excite OClO in the wavelength range 355 – 370 nm and probed Cl via a (2+1) REMPI process near 235 nm. In contrast to the work of Lawrence *et al.*, the quantum yield near 362 nm for the formation of Cl was given to be 0.15 ± 0.10. The REMPI spectrum of Bishenden *et al.* reproduces the OClO absorption spectrum, suggesting that the Cl^+ signal *does* result from OClO dissociation.

However, recent studies by Davis and Lee,[11] who measured the Cl yield from 350 to 475 nm by photofragment translational energy spectroscopy, found that the total yield of Cl production is only important near 404 nm, where a maximum of 3.9 ± 0.8 % is reached; the yield between 350 nm and 370 nm is below 0.2 %. In order to explain these discrepancies, Davis and Lee suggested that the high yield in Bishenden's REMPI spectrum is due to photodissociation (by the probe laser) of the ClO product followed by REMPI (2+1) detection of Cl atoms within the time duration of the ns-probe laser used in the experiments. A further result of their work is that the yield of Cl + O_2 from symmetric stretch or symmetric stretch plus bend excitation is ~10 times greater than the yield from states at nearly the same energy with asymmetric stretch excitation. To explain this mode-specific behavior, it was proposed that the symmetric stretch and the bending modes favor coupling into the $^2B_2$ state whose equilibrium angle is near 90° (Fig. 6.2). On this state, then, the OClO undergoes a concerted decomposition from a transition state geometry close to C_{2v}, rather than an isomerization process to form ClOO followed by a unimolecular dissociation. This is consistent with the theoretical analysis of Gole[1] who suggested that vibronic coupling to nearby states plays an important role in the Cl + O_2 channel.

Glownia *et al.*[5] have reported on the absorption, in a static gas cell, of OClO in femtosecond pump-probe experiments. The OClO was excited by a pump pulse at 308 nm, while the ClO product was monitored by the absorption of a continuum probe pulse in the wavelength region between 268 and 278 nm. No ClO was detected on a time scale of up to 1 nanosecond! Using a 308 nm nanosecond excimer laser as a pump and the femtosecond continuum laser as a probe, however, ClO absorption built up after several hundred nanoseconds. Vaida *et al.*, who detected the formation of ClO^+ within the nanosecond laser pulse at 308 nm, attributed the unexpected (very long) observed time scale of Glownia *et al.* to the collisional relaxation of the vibrationally excited ClO.[7]

From the above discussion, the time scales for predissociation in the energy range up to $v_1 = 10$ are inferred from line width measurements. The yield of ozone-destroying Cl in this photodissociation process seems to be minor, especially in a wavelength regime below 370 nm. The corresponding predissociation mechanisms for this Cl + O_2 channel are interpreted in terms of various interactions of the initially excited A^2A_2 state with the two lower-lying $^2A_1$ and $^2B_2$ states. In what follows, we consider the femtosecond dynamics in the high-energy excitation regime of $v_1 = 11$ to 17. The observation of the femtosecond decay of the initially excited states gives direct measure of the dissociation. From the shape of the femtosecond transients and the energy dependence, we examine the mechanism and the dynamics of prompt OClO dissociation to ClO + O *vs.* the indirect dissociation, involving nearby potentials, in the ClO + O and Cl + O_2 channels.

Experimental

The femtosecond laser apparatus has been described in detail previously (see Chapter 2) and is discussed only briefly here. Femtosecond pulses were generated from a colliding pulse mode-locked ring dye laser (CPM), and amplified by a

Nd:YAG-pumped pulsed dye amplifier (PDA). The recompressed output pulses had an (unattenuated) energy of 0.2 – 0.3 mJ at a repetition rate of 20 Hz. The pump wavelengths in the range from 308 nm to 312 nm were generated by frequency doubling a part of the PDA output in a 0.2 mm thick KDP crystal; for these wavelengths the CPM was tuned by proper adjustment of the saturable absorber concentration. In order to obtain the wavelength range from 312 nm to 352 nm, we focused part of the PDA output on a D_2O cell to produce a white light continuum. With 10 nm bandwidth interference filters, we selected the desired wavelengths from 624 nm to 704 nm; this light was further amplified in a longitudinally-pumped dye cell before doubled in a KDP crystal. For the MPI probe, we used the remaining output of the PDA at 620 nm.
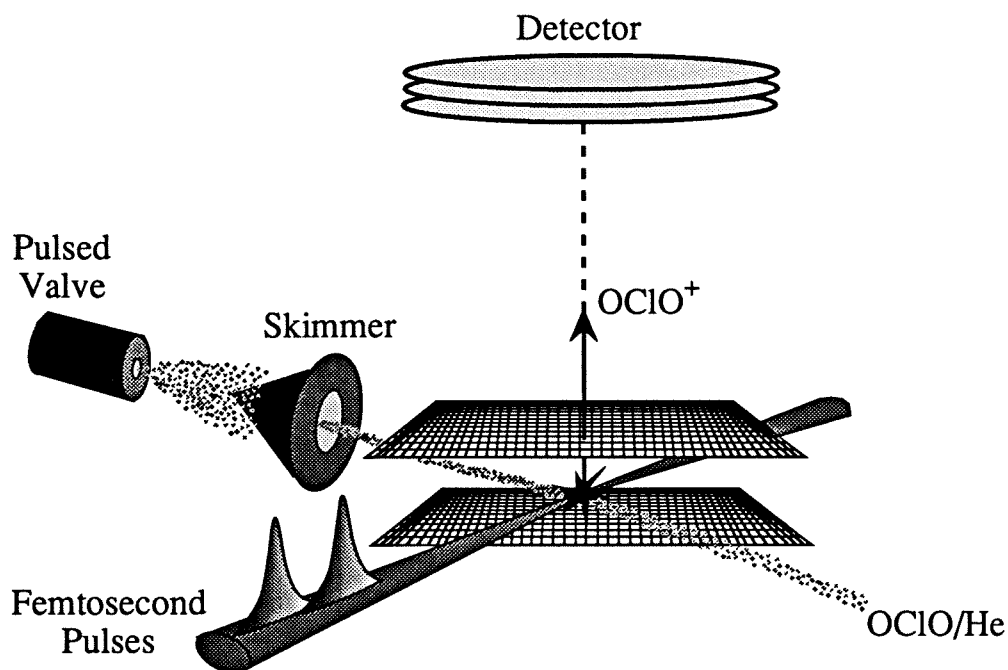

Figure 6.5 Schematic of our experimental set up. The collinear femtosecond lasers, the molecular beam, and the TOF axes are all mutually perpendicular.

The pump and probe beams, with proper attenuation and parallel or perpendicular polarization, were delayed in time relative to one another in a Michelson interferometer and were then recombined collinearly and focused onto the OClO molecular beam. Before entering the molecular beam, we routinely recorded autocorrelations of the probe (~ 80 fs sech^2) and crosscorrelations between pump and probe (~ 190 fs).

The supersonic molecular beam consisted of a pulsed nozzle with an orifice diameter of 0.3 mm. MPI experiments on the skimmed molecular beam were carried out in a differentially-pumped ionization chamber about 12 cm downstream from the nozzle. The time-of-flight (TOF) detector had a field-free drift tube with a mass resolution of $\sim 1{:}150$. The molecular beam, the lasers, and the TOF detection axes were mutually perpendicular. A sketch of the experimental arrangement is shown in Fig. 6.5.

OClO was produced in situ by flowing a 3.5% Cl/He mixture through a U-tube packed with glass beads and $NaClO_2$, following the procedure of Derby and Hutchinson.[33] In order to be below the detonation limit of OClO, a constant total backing pressure of 1.5 atm was maintained for the expansion of OClO. In concentrations in excess of 10% of atmospheric pressure OClO is easily detonated by sources of initiation such as sunlight, heat, or electric discharge.[33]

Results

In Fig. 6.6, a TOF spectrum is shown for an excitation wavelength centered at 329 nm. This corresponds to the absorption peak 14 in Fig. 6.1 which is labeled spectroscopically as the (14 0 0) band. The probe laser (620 nm) was set at a time delay of 170 fs. A prominent feature in this REMPI TOF spectrum is the two OClO isotopes. As mentioned above, OClO$^+$ ions have not been observed previously in ns-

laser resonance-enhanced multi-photon ionization (REMPI) experiments.[13] The products in this spectrum are the two ClO isotopes. Sufficient cooling of our sample is obtained, as evident by the onset of the cluster formation. We also observe $(OClO)_n$ clusters with n = 1 - 3 and $(OClO)_n \cdot (H_2O)_m$ clusters with n, m = 1 - 3. No additional water was used in the heterogeneous OClO-water cluster formation; the inherent moisture of the $NaClO_2$ provided enough water vapor pressure for clustering. All cluster mass channels are split due to the two Cl isotopes. The $(H_2O)_5$ cluster, prominent in the electron impact mass spectrum of Vaida *et al.*,[13] is not seen in this fs pump-probe REMPI spectrum under the above conditions.
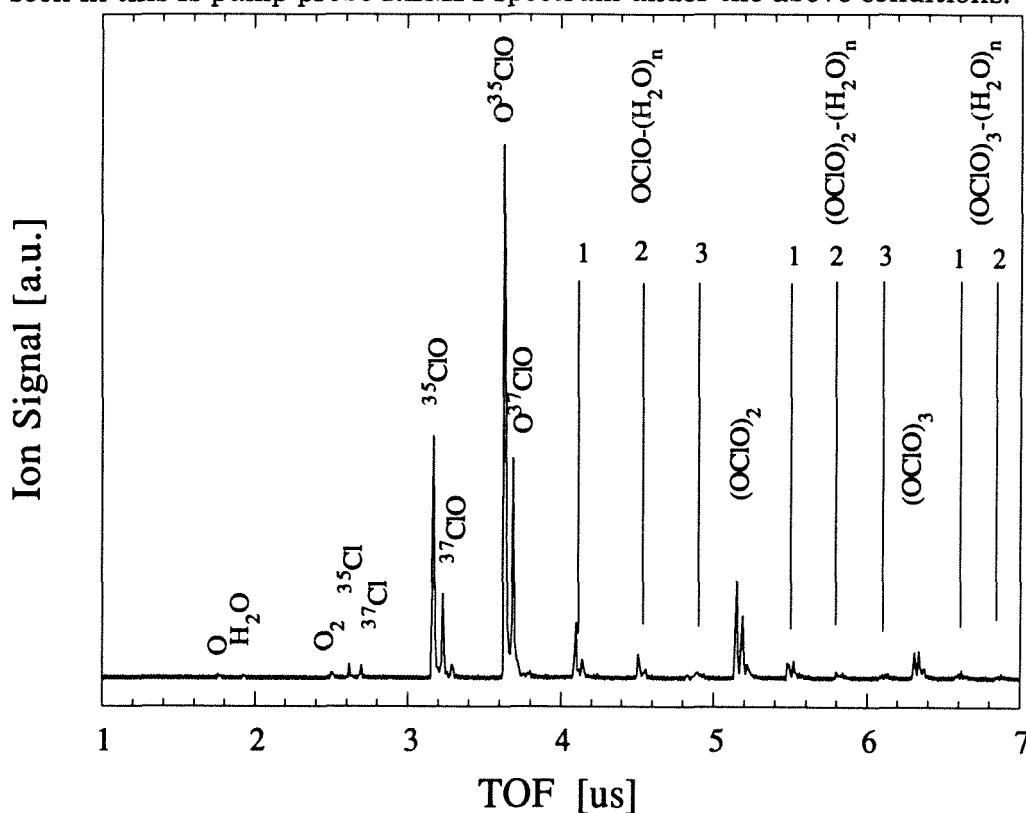

Figure 6.6 TOF spectrum taken in a femtosecond pump-probe arrangement. Note that the prominent masses are the OClO parent and the ClO product.

The femtosecond experiments on the mass-selected parent OClO or fragments involve the following scheme of energy and mode excitations (Fig. 6.7). The initial excitation is from the (0 0 0) state (with relatively low hot-band

excitation) of the X^2B_1 ground state of OClO to the A^2A_2 state (region between 3.5 eV to 4 eV). In the absorption spectra of Fig. 6.1, this excitation corresponds to the bands 11 (351.3 nm) to 17 (311.5 nm). This transition is parallel polarized; the perpendicular polarized transition into the $^2A_1$ state, in principle allowed, has not been observed experimentally.[13] The transition to the $^2B_2$ state is dipole forbidden. In the energy range of 7 eV to 8 eV (two pump photon excitation), only one-photon absorption spectra are reported,[34,35] with very short progressions.[35] As discussed below, two-photon excitations are minimized.
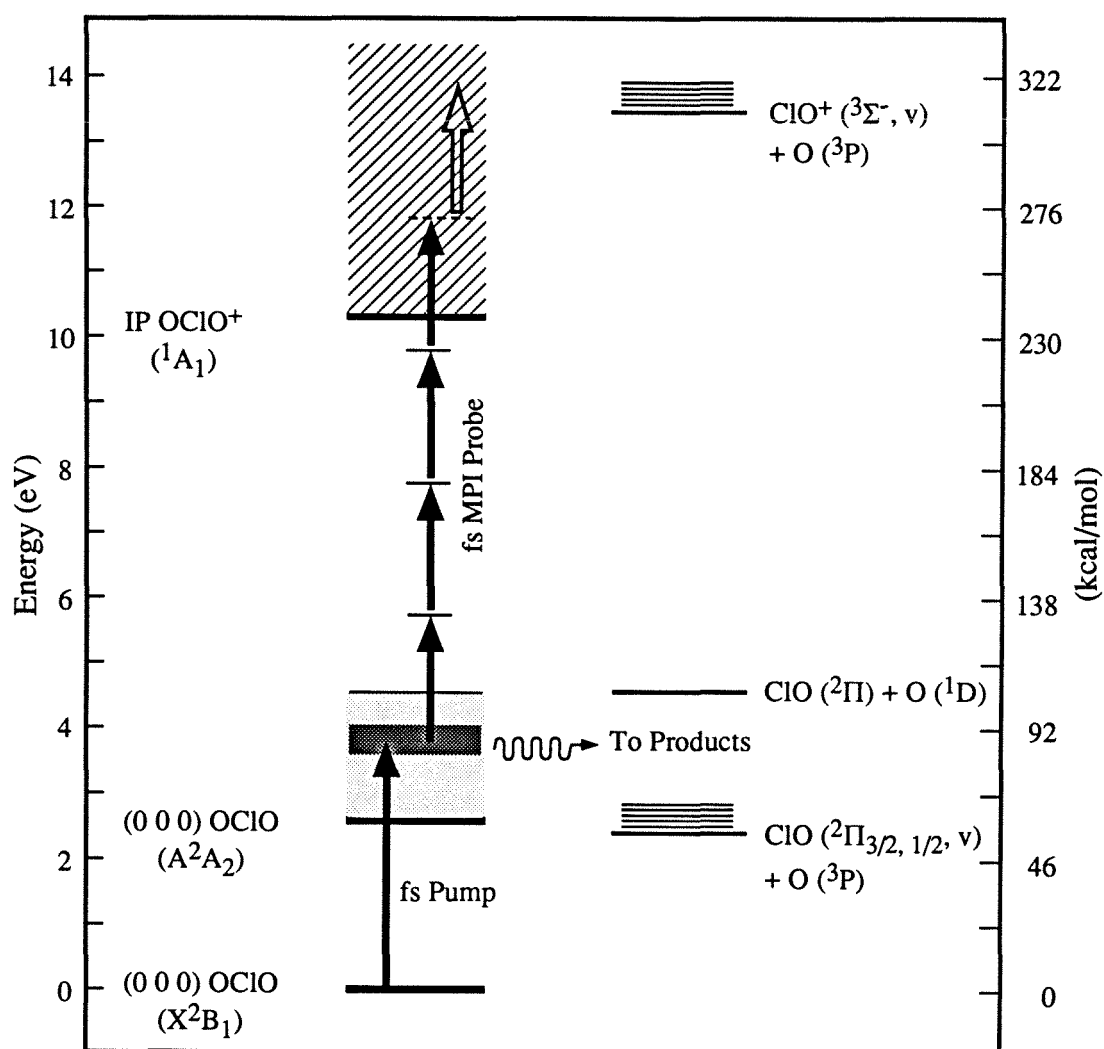

Figure 6.7 Pump-probe excitation scheme for studying OClO fragmentation dynamics.

It takes four probe photons at 620 nm to ionize the system. A continuous increase of the one-photon absorption cross section from 6 eV up to 25 eV was measured by Flesch *et al.*,[34] indicating that the probe laser ionization involves a REMPI process (*vide infra*). The ionization potential of OClO is 10.33 ± 0.02 eV.[34] As shown in Fig 6.7, at least one additional probe photon (making a total of at least 5 probe photons) is required to reach the ionic fragmentation channel. The threshold for ClO^+ ($^3\Sigma^-$) + O (^3P) is measured to be 13.45 ± 0.04 eV.[34] The D_0 value for the neutral ClO ($^2\Pi$) + O (^3P) asymptote is given to be 55.2 ± 2 kcal/mol,[36] corresponding to ~2.4 eV. Taking into account the fact that the ClO fragments are vibrationally excited to the $v'' = 3 - 6$ range[7] and knowing the vibrational frequency of ClO in its ground state (~0.1 eV),[36] our total available energy with respect to ground state fragmentation is ~1 eV. Energetically, the next higher fragmentation channel leading to ClO ($^2\Pi$) + O (^1D) would require a threshold energy of ~4.5 eV. Hence, the fragmentation channels leading to electronically-excited ClO or excited O may be excluded from further consideration.

Typical femtosecond transients taken on $O^{35}ClO$ and ^{35}ClO are shown in Fig. 6.8 and Fig. 6.9. The transients were taken at a pump wavelength of 329 nm, at band 14 in Fig. 6.1. First we consider the $O^{35}ClO$ transient in Fig. 6.8. From the insert, plotted on a logarithmic scale, it is evident that the transient shows a biexponential decay. The crosscorrelation, also shown in the insert, is symmetric and different from the initial decay. The time constants, derived from a molecular response function of the type

$$M(t) = Ae^{-t/\tau_1} + Be^{-t/\tau_2} \quad (A + B = 1), \tag{3}$$

are τ_1 ~ 50 fs, τ_2 ~ 400 fs, and A ~ 0.89 for this transient. These results depend on the initial excitation energy and is not consistent with a simple sum of a decay and

an off-resonance ionization signal (*vide infra*). The values for τ_2 are much larger

than our response function; in order to obtain accurate values of τ_1, we convoluted

the transient form of equation (3) with the measured crosscorrelation taken

carefully before and after the experiments (Fig. 6.8).
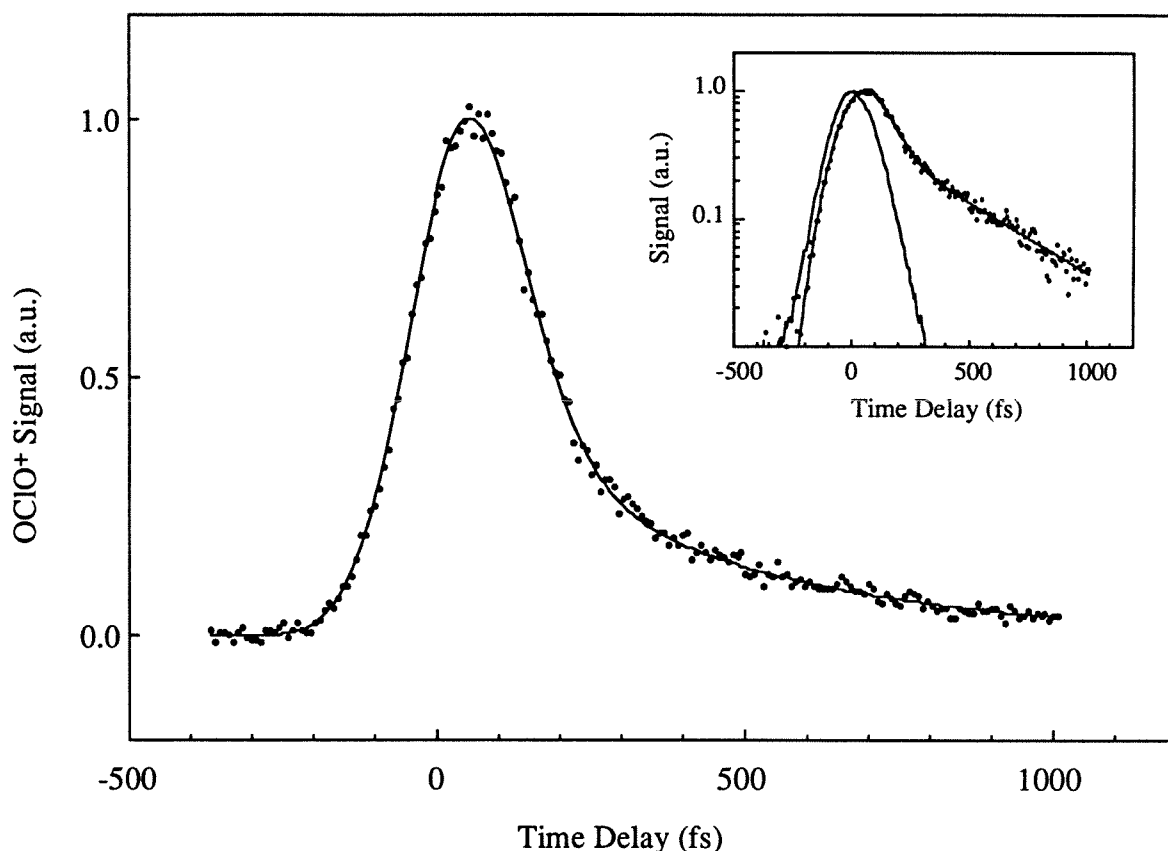
Figure 6.8 Typical femtosecond transient taken on the $O^{35}ClO$ parent mass. The solid line is a double exponential fit to the data including convolution with the cross-correlation. The insert shows the decay on a logarithmic signal axis, in which the bi-exponential character is evident. For comparison, the symmetric cross-correlation is also shown in the insert.

Care was taken in considering several control experiments. First, according

to the energetics of this system (Fig. 6.7), the process requires one pump photon and

four probe photons. The laser intensities were therefore adjusted such that the

pump laser alone did not produce an appreciable MPI signal. Typical values were a

maximum of 10% MPI signal from the pump laser alone relative to the MPI level of the stronger probe laser. The maximum signal enhancement was then typically 2 to 3 times greater than the time-independent background consisting of the sum of pump and probe MPI levels.
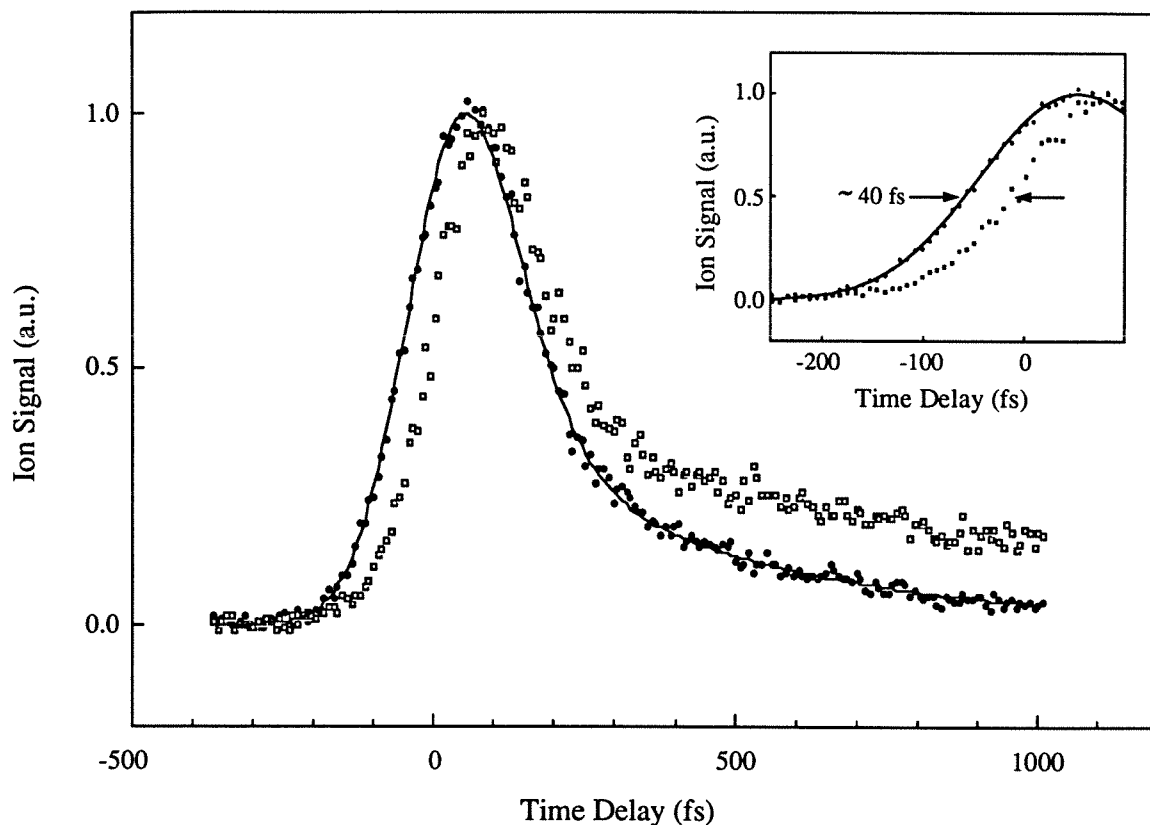
Figure 6.9 $OClO^+$ transient (dots) and ClO^+ transient (squares) taken under the same experimental conditions. Note the similar shape of the transient, but the time shift in the rise, and the final value at longer pump-probe delay times in the ClO^+ transient (see text).

Second, while the pump (alone without the probe) MPI background signal *vs.* intensity showed an approximate quadratic power dependence, the total signal due to pump plus probe *vs.* pump laser intensity showed an approximate linear power dependence. Probe laser intensity studies showed a similar behavior.

Third, the ratio A/B of the amplitudes of the two time constants (equation

(3)) did not change by attenuating the pump laser, as would be expected if one of the

$$M(t) = Ae^{-t/\tau_1} + Be^{-t/\tau_2}$$
$$A + B = 1$$

Figure 6.10 Pump wavelength dependence of the two time constants and the A/B ratio. The peak numbers correspond to the numbers given in Fig. 6.1 for the vibrational stretch quantum number. The points where error bars are shown represent data sets that include enough measurements to give a meaningful standard deviation.

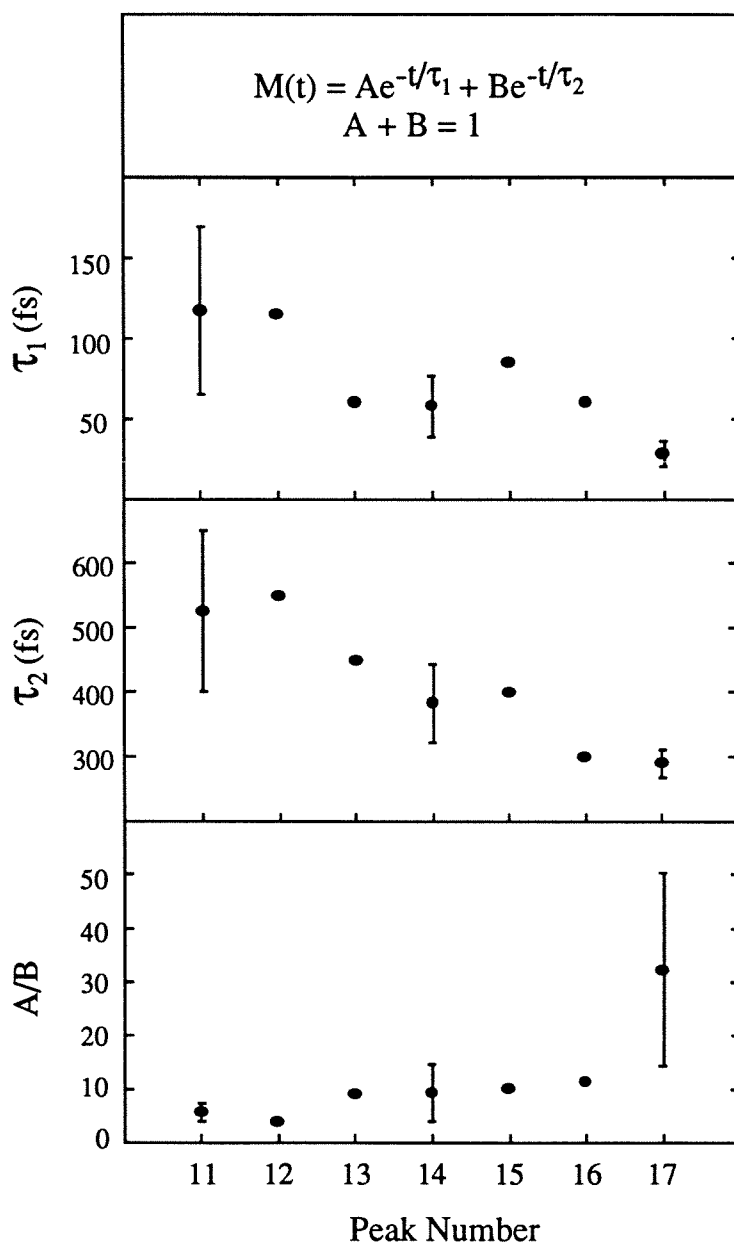time constants were due to a two-photon or off-resonance excitation. It is known from similar work that the pump laser intensity does not affect the time constants in a femtosecond MPI process (where one-photon excitation dynamics and two-photon excitation dynamics contribute to the observed transient ionization signal), yet the *ratio* of these contributions is very sensitive to intensity.[37] A further indication of the approximate linearity of the total signal in these experiments is that the rise of the transients could be fitted nicely to the crosscorrelation (measured in front of the molecular beam apparatus).

Fourth, parallel or perpendicular polarization of our lasers had no significant influence on our transients, neither on the observed time constants nor the A/B ratio. Most of the experiments were performed with perpendicular polarization.

Tuning the laser from v_1 band 17 to band 11 resulted in an increase of τ_1 from about 30 fs to about 120 fs. The second time component also increased from about 300 fs to ~ 500 fs. This increase in the time constants with respect to lower excitation energies is accompanied by a decrease of the A/B ratio of the two time components; the fast component was always found to be the dominant contribution. These trends are summarized in Fig. 6.10.

From the high-resolution work of Vaida *et al.*,[9] it is known, at least for the low excitation regime, that to the blue side of every pure symmetric stretch excitation a (v_1 0 2) band is observed (in addition to other combination bands). The rotational line broadening analysis suggests significant broadening of the (v_1 0 2) band compared to the symmetric stretch alone (v_1 0 0).[10] Tuning the central wavelength of our fs-pump laser up to 4 nm to the blue side of the (14 0 0) band did not yield significant changes in the two time constants. Thus, the "mode selectivity" seen in the low-excitation regime seems to be blurred in the high-excitation region of the spectrum, where mode-specific structure also appears to "wash out" in the

low-resolution spectrum (Fig. 6.1). Note that this small tuning is comparable to the fwhm (~ 3.5–4 nm) of the pulse. If the transient were composed of a superposition of two components (decay and off-resonant ionization), we would have expected changes in the A/B ratio of the fast and slow components associated with tuning the central wavelength of the pump from a maximum in the low-resolution spectrum to as much as 4 nm away.

In addition to the above results on the parent molecule, we also studied the transients of the observed mass fragments. The ClO transient in Fig. 6.9 resembles the OClO transient, also shown in this figure, but there are two differences: First, the rise of the ClO is shifted with respect to the rise of the OClO transient by 20 to 40 fs. This shift is real, as the ClO transients were recorded with the same experimental conditions as the OClO transients, by only changing the detection electronics (gate of a boxcar) from the mass of the OClO to the mass of the ClO. The shift is displayed in the inset of Fig. 6.9. Second, the final value of ClO^+ reaches an asymptote of 15 to 25 % of the total signal, as seen in Fig. 6.9. On a time scale of up to 15 ps (the maximum pump-probe delay in these experiments) this final value remained constant.

Power dependence studies also showed an approximate linear dependence of the total signal with respect to pump and probe laser intensities. The fact that the ClO signal reaches a final value is consistent with the expectation that the neutral fragmentation of OClO leads to ClO + O after the pump-pulse excitation. As the IP of ClO is 11.01 ± 0.01 eV,[38] it takes six photons of our probe laser to ionize this species. This non-zero ClO signal at all excitation wavelengths (including 308 nm, where previous femtosecond experiments were performed) is formed on the fs time scale and remains for long times.

For the short-time behavior, the OClO and the ClO transients match in shape, but, of course, with the time shift. This suggests that they have the same
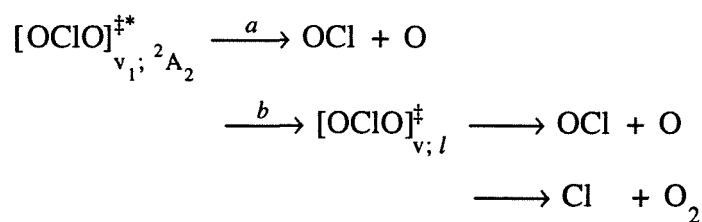
origin; they are directly related to the fragmentation dynamics of the OClO. Note that only one additional probe photon is needed to reach the ionic fragmentation channel from the ionic OClO ground state (Fig. 6.7). Typical time scales in the ionic ground state are ~35 fs for the symmetric stretch and ~70 fs for the bending motion.[34] These times correspond to the observed shift of about 20 to 40 fs of the ClO^+ transient with respect to the $OClO^+$ transient. We therefore suggest that the time shift is due to the propagation of a wave packet in the $OClO^+$ ground state from the region initially excited by four probe photons into a region where the Franck-Condon (FC) factors are more favorable for the ClO^+ + O fragmentation. Absorption of a fifth probe photon would then lead to such fragmentation. The transient of the ClO^+ thus reflects both the neutral product formation and then ionization (long-time constant level) and the parent OClO ionization and subsequent ion fragmentation with decay (short time behavior).

Discussion

The observed biexponential decay of OClO over the entire range of v_1 studied indicates that the dynamics do not reflect a direct process only. There are a number of characteristics which assign the origin of the observed behavior. First, the decay constant of the fast component, which ranges from about 30 fs at $v_1 = 17$ to about 120 fs at $v_1 = 11$ is different from the two pulse crosscorrelation; as mention before, the cross-correlation is symmetric whereas the fast component is not. Second, the slow component of the decay, which ranges from about 300 fs at $v_1 = 17$ to about 500 fs at $v_1 = 11$, depends on the excitation energy. Third, the ratio of the fast to slow component, which does not change with intensity (pump or probe), changes with v_1, but not when the pump is tuned within a specific v_1 band (~4 nm range). From these observations, we conclude that the fast component is not an

"off-resonance" transient peak, consistent with the fact that the pump is tuned to the strong absorption of the v_1 bands and not to an off-resonance absorption region. The fact that we did not see change in the transient behavior over a given range of v_1 indicates that there is no mode selectivity at these high energies and that homogeneous dynamics from an initial state are operative. For example, one may attribute the fast component to a level involving the asymmetric stretch ClO + O products channel and the slow component to the symmetric stretch level which ultimately produces Cl + O_2. However, this assignment is inconsistent with the A/B ratio as the absorption of the v_1 dominates, and also the yield for the Cl + O_2 channel at 350 – 370 nm is less than 0.2%.[11]

The simplest mechanism to emerge involves the decay of the v_1 state on the $^2A_2$ potential and the formation of intermediates of OClO on the nearby PES(s). The reaction involves the following elementary steps:

$$
[OClO]^{\ddagger *}_{v_1;\, ^2A_2} \xrightarrow{\ a\ } OCl + O
$$

$$
\xrightarrow{\ b\ } [OClO]^{\ddagger}_{v;\, l} \longrightarrow OCl + O
$$

$$
\longrightarrow Cl + O_2
$$

$$
\tag{4}
$$

The total rate of the initial decay is determined by both $a + b$ channels. Fundamentally, process a is the one described in Fig. 6.3. Excitation of the symmetric stretch is bound provided the system is along the line of the saddle (in a deterministic classical picture), but of course any motion (even zero-point motion) can take the system into the second dimension of the asymmetric stretch to yield OCl + O. In an adiabatic picture (and on one surface), v_1 excitation in the transition-state region leads to v'' excitation in the OCl with a net translational energy for the recoil of OCl and O. We can estimate the time scale for this process

based on the energetics, assuming a simple exponential repulsive potential. Taking the steepness of the potential to be 0.7 Bohr (0.37 Å) (extrapolated from the asymmetric stretch coordinate in Fig. 6.2), and knowing that the translational energy release is about 1 eV (the excess energy above the OCl + O threshold minus the internal energy of OCl), the time for bond breakage (at 5.5 Bohr, see Fig. 6.2) is approximately 40 fs.[39-41] Naturally, at least 2-*d* calculations are needed for accurate comparisons.
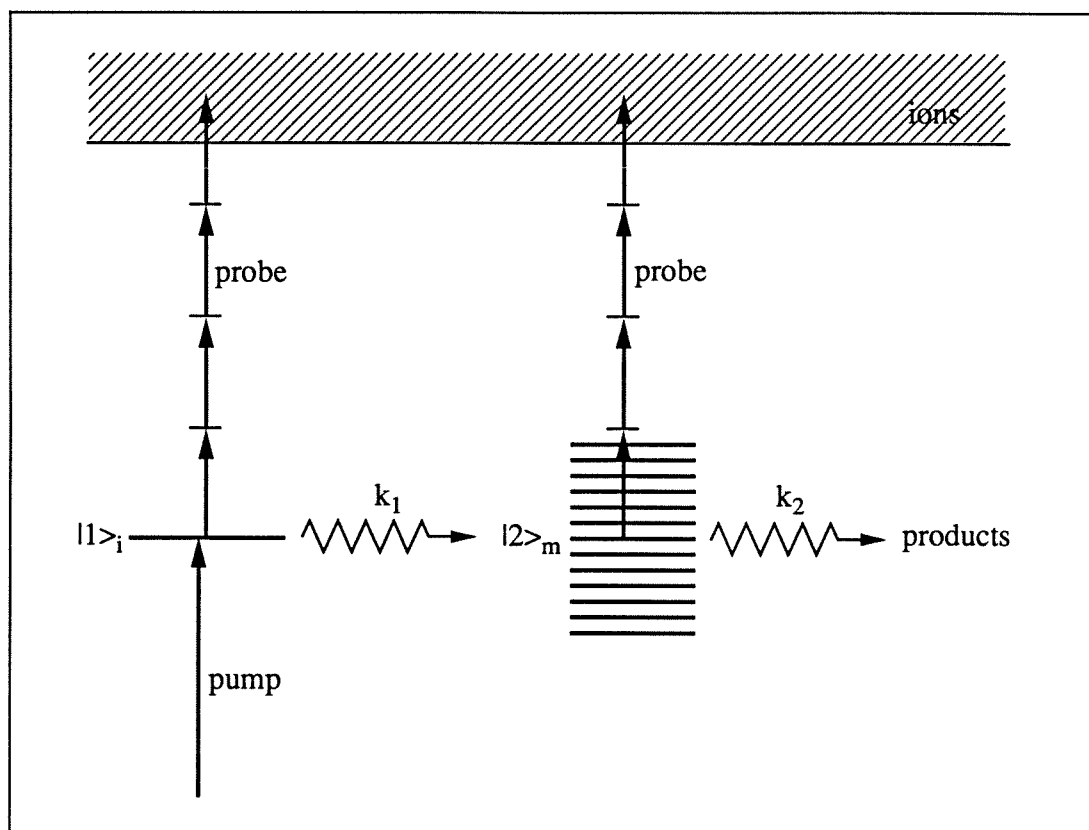

Figure 6.11 The scheme for the coupling of the initial $\{|1\rangle\}_i$ state to a manifold $\{|2\rangle\}_m$ of levels, followed by a dissipative decay to translational continua (see text).

The total rate for producing the intermediate(s) $[\text{OClO}]^{\ddagger}_{v;\,l}$ in different vibrational levels (v) of the lower-energy (l) PES(s) via channel b is determined by

the effective coupling of the $^2A_2$ state to the nearby $^2B_2$, $^2A_1$, or to the ground state, $^2B_1$. Quantum mechanically, one must consider the coupling of the $|^2A_2, v_1>$ level to the quasi-energetic levels of the intermediate which then couple to the translational continuum of the OCl + O or Cl + O_2 channels. This type of coupling (see Fig. 6.11) can find analogies in the problems of IVR and non-radiative decay (for reviews, see Refs. 42,43). To compare with experimental rates we adapt a simple kinetic model (biexponential decay) which captures the essence of the quantum treatment, keeping in mind that the fundamental limitation of the kinetic description is the absence of coherence.[42,43] This type of two-step model has been invoked in describing similar biexponential behaviors associated with the dynamics of IVR in stilbene by MPI,[22] IVR/predissociation of van der Waals complexes by fluorescence or MPI,[24,44] and more recently for H-atom transfer.[45] Biexponential decay[46,47] has also been observed in relation to inter-electronic state coupling.[48]

In the case of OClO, the initial state $|^2A_2\ v_1>$ ($\equiv |1>_i$ in Fig. 6.11) undergoes energy redistribution into the manifold of the lower-energy surfaces followed by the relatively slow overall decay of the "equilibrated" distribution to give products. Designating the decay constant of the initial non-stationary state by k_1 and the equilibrated distribution by k_2, one can obtain an expression for the population change with time. Ionization out of the ($|1>_i$) state is described by an effective four-photon ionization cross section σ_1, and by σ_2 for ionization out of the ($|2>_m$) manifold. Solving the corresponding rate equations leads to a molecular response function for the ion yield M(t) as a function of pump-probe delay time (t), of the form:

$$M(t) = 0 \qquad\qquad \text{for } t < 0$$

$$M(t) = (\sigma_1 - \sigma_2 K)e^{-k_1 t} + \sigma_2 K e^{-k_2 t} \qquad\qquad \text{for } t \geq 0$$

(5)

In (5), the linear pump excitation is invoked and K is given by $k_1/(k_1 - k_2)$. The expression for $M(t)$ given here is related to $M(t)$ in equation (3) by $A = \sigma_1 - \sigma_2 K$; $B = \sigma_2 K$; $\tau_1 = 1/k_1$; $\tau_2 = 1/k_2$: the ratio A/B is given by $(\sigma_1/\sigma_2)((k_1 - k_2)/k_1) - 1$. In Ref. 22, the explicit influence of a resonant intermediate for probing in this kind of model is investigated. It was found that only the ratio of the two rates is affected, not the rates themselves. For this reason, we describe our four-photon probe process by an effective ionization cross section, and the effect of the intermediate is discussed only when we consider power dependencies (*vide supra*). Note that we have neglected reversibility of $(|2\rangle)_m$ to $(|1\rangle)_i$ based on the relative density of states. However, σ_1 should be on the order of $10\,\sigma_2$ for typical time constant and amplitude values (Fig. 6.10), otherwise the response function would not have an instantaneous rise. REMPI probing from two different electronic structures could explain different ionization cross sections[46] simply by different selection rules or ionization potentials for the four probe photons involved in the ionization process.[49]

The nature of the $[OClO]^{\ddagger}_{v;\,l}$ intermediate depends on the potential. On the ground state $^2B_1$, the intermediate is a vibrationally-hot ground state molecule with energies of ~1 eV above dissociation (Fig. 6.2) to ClO + O. In C_{2v}, Herzberg-Teller vibronic coupling is allowed between $^2A_2$ and $^2B_1$ as the direct product contains the b_2 irreducible representation of the asymmetric stretch vibration. In Ref. 3, this route was considered less likely at lower energies because of the selectivity in line broadening with respect to the spin state prepared and the "large" density of states. At higher energies, the situation is different, particularly that the number of states is increased significantly. We can estimate the time scale for the decay of the "equilibrated" $(|2\rangle_m)$ distribution, described by k_2, by calculating the rates based on microcanonical transition-state theories. This is similar to the treatment given in Ref. 23 for the dissociation of NCNO. However, since the energy above dissociation

is large (~ 1 eV), we expect the transition state to be more of a tight-type. Accordingly, we adopted the simple RRKM expression:

$$k(E) = \frac{N^{\ddagger}(E - E_0)}{h\,\rho(E)}$$

(6)

for an order-of-magnitude estimate. In equation (6), $N^{\dagger}(E - E_0)$ is the number of states in the transition-state at energy E, excluding the reaction coordinate. E_0 denotes the reaction threshold, while $\rho(E)$ is the density of states of the reactant. The estimate was made by taking the vibrational frequencies from Peterson and Werner[12] (see also Table I) for the three electronic states under consideration (ignoring anharmonicities). E_0 was chosen to be D_0 for the X^2B_1 ground state. Taking the degeneracy of the problem into account (both bonds are equivalent), we multiplied the calculated rates by a factor two. Expressed in lifetimes, we obtain the following results by this estimate: the X^2B_1 state shows increasing decay times from 90 fs to 130 fs in the wavelength range from 310 nm to 350 nm. Similar estimates were made for the other states. Decay of the $^2B_2$ state results in a constant fragmentation time of about 30 fs in this energy range. The $^2A_2$ state shows an increase in the decay times from 30 fs to 50 fs.[50]

The experimental observation of an increase of the slow time constant from about 300 fs at 310 nm excitation to about 500 fs at 350 nm excitation is in agreement with RRKM trends which shows an increase of the decay time with decreasing excitation energy. The fact that tuning the pump laser in small energy ranges (up to 4 nm) did not affect the decay times is consistent with the interpretation that the biexponential decay is due to energy redistribution followed by a decay of a distribution of levels of the intermediate(s) formed. As mentioned above, the calculation of k(E) is intended to serve as an order-of-magnitude

estimate and more accurate calculations, similar to those done on NCNO (Ref. 51) are underway. We also plan to compare with calculations made for analysis of the recent sub-picosecond study of NO_2 dissociation by the Wittig group.[52] In the preliminary study of the OClO-water clusters we have observed the fast component but the signal-to-noise ratio was not (yet) good enough to obtain an accurate ratio of A/B. It is consistent to see a fast (or faster) component as we expect the cluster modes to help the energy redistribution.

The Cl + O_2 products channel also involves the coupling of two potentials. The transition from the ground state $^2B_1$ to the $^2A_2$ state results in the promotion of an electron into an orbital (b_1) which is Cl–O antibonding but O–O bonding. The bond angle accordingly decreases from 117° to ~107° and the Cl–O bond length increases from 1.47 Å to 1.62 Å.[1] Even though the bond angle decreases, the increase in bond length requires very large amplitude motion for concerted[1] O_2 + Cl to occur. However, if the intermediate [OClO]‡ has some population on the $^2B_2$ surface, then this intermediate will be produced with a compressed angle of ~90° (see Fig. 6.2); the electronic coupling between $^2A_2$ and $^2B_2$ provides a sensible route for having the two oxygens closer to each other on the $^2B_2$ surface. (The $^2A_1$ state may be involved indirectly.) To break the bond, the molecule in the transition-state region of the $^2B_2$ surface, which is rather strained, will concertedly release a large amount of kinetic energy, consistent with the beam experiments of Davis and Lee.[11] However, the rate of crossing into this transition-state will depend, at a given energy, on the vibrational energy redistribution on the $^2B_2$ surface and, in particular, on the bend time scale. If we relate (in part) our long decay (hundreds of fs depending on v_1) to such a crossing, then only a few bend motions (see Table I) are required, since the period is about 100 fs. Once the system gets into the transition-state region, within a vibrational period the Cl and O_2 separate yielding the large release of kinetic energy. Because of this barrier crossing and downhill

kinematic, the translational energy distribution will not reflect the rate. The initial state absorption line width measurement, even if homogeneous, as discussed below, will not give the dynamics of this or the $^2B_1$ intermediate.

The coupling of the $^2A_2$ to the $^2B_2$ potential is by spin-orbit coupling[3] and is not allowed in C_{2v} by a Herzberg-Teller mechanism ($A_2 \otimes B_2 = b_1$). Also in C_S this coupling is not allowed. Thus, the interplay between the spin-orbit coupling to $^2B_2$ and the vibronic coupling to $^2B_1$ determines the nature of the intermediate, and at higher energies, where the $^2B_1$ density of states is increasing, vibronic coupling may become the dominant interaction. This brings to focus two points: First, the yield for the Cl + O_2, as mentioned above, decreases considerably at higher energies. Second, asymmetric vibrational excitation decreases the yield of Cl + O_2 (promoted by the bending mode; see Ref. 11 and previous section) as this excitation represents a promoting mode to the ClO + O channel via vibronic coupling. Additionally, the trapping of ClOO in matrices by Arkell *et al.*,[53] which suggested[1] the isomerization of OClO to ClOO, may be the result of an interesting change in dynamical time scale. With energy dissipation to phonons the intermediate (*e.g.*, $^2B_2$) could cool down and the rate of crossing the transition-state would become slow enough to compete with isomerization into ClOO.

To be complete, we must address the line width problem. At the energies studied here, Vaida's group reported the high resolution spectrum (Fig. 6.4). From the fit of a rotational band contour, they inferred a width of ~4 ps for $v_1 = 10$ and indicated that these widths "saturate" giving a value of ~1 ps at 303 nm (v_1 between 18 and 19). Several points must be considered. The mechanism discussed above reflects "overlapping resonances" because of the coupling with lower-energy potentials. This results in a background, and it is impossible to consider the system as homogeneously broadened in the sense of a two-level problem with $\Delta\bar{v}_{width}$ (cm^{-1}) = $1/(2\pi c \tau)$ (for a Lorentzian line shape). Second, there is a finite convolution due to

the inhomogeneous rotational distributions of both states. For $v_1 = 11$, as an example, the two components of the OClO decay are $\tau_1 \sim 120$ fs and $\tau_2 \sim 500$ fs. We therefore expect a broad component of 44 cm^{-1} and narrower resonances of 11 cm^{-1} within this envelope. The high-resolution line width has a large apparent width (~ 40 cm^{-1}) which is comparable to the 44 cm^{-1} broadening, but clearly does not give the separate true dynamics of the initial state and the intermediates (bond breakage).

An envelope of 44 cm^{-1} must be less than the $\Delta \bar{v}_1$ separation (~ 700 cm^{-1}) in order for the v_1 progression to be observed and "predissociation" to be identified. Indeed, this is experimentally true, and brings another important point: the excitation in the v_1 manifold is in the transition-state region of the $^2A_2$ potential. The v_1 "sharp" progression is therefore the (transverse) vibrational structure of the transition-state[54] and to be observed the lifetime for motion along the asymmetric stretch must be longer than the symmetric stretch vibrational period. In the example given above, the spacing between the v_1 transitions is ~16 times greater than the width of an individual v_1, indicating that the lifetime is longer than the symmetric vibrational period by a factor of ~3 (note that even if the lifetime and the vibrational period are the same, the ratio of the separation to line width is ~6 because of the 2π factor on going from lifetime to width). If the potential along the symmetric stretch is anharmonic, then the period will be even longer than that determined by the $v_1 = 1$ frequency. When there is separation of the symmetric stretch transitions, one speaks loosely of "predissociation" but it should be noted that this is not vibrational predissociation in its strict sense where vibrational energy transfer is part of the dissociation dynamics (as, for example, in the dissociation of van der Waals complexes ($A_2 \cdot X$)). The analogy made here with excitations to the transition-state region is similar to the case of HgI$_2$ discussed above,[17-19] and to the photodetachement experiments of Neumark *et al.*[55] where

direct absorption has been made. Butler has made this analogy between absorption and "resonance" dynamics recently.[56] For OClO, the initial transition-state region excitation and coupling with nearby surfaces are the two key dynamical features for the elementary fragmentation to OCl + O and Cl + O_2.

Conclusions

This contribution presents femtosecond real-time studies of OClO elementary fragmentation in a supersonic molecular beam. Mass-spectrometry detection has been used to identify the reactants, products, and some selective clusters of OClO with water. These dissociation products, ClO, O, and Cl (and the isomer ClOO), played an important role to the first millisecond flash photolysis experiments[57,58] and to the ozone depletion problem.[59] Here, the wavelength range from 308 to 352 nm was covered, corresponding to symmetric stretch excitation of $v_1 = 17$ to 11. The parent ion $OClO^+$ is observed for the first time with femtosecond pulses, making it possible to monitor the initial dynamics of OClO. This ion was not detected in ns-laser REMPI experiments performed in this excitation energy range due to the efficient ultrafast photochemistry.

The observed decay shows a biexponential behavior; both time constants decrease with increasing excitation energy. The form of the transients and their change with energy reflects the reaction intermediates, and our analysis considers the nearby potentials ($^2B_2$, $^2A_1$) and the ground state ($^2B_1$) as the source of interaction. In addition to the direct fragmentation to ClO + O, the dissociation proceeds through the intermediates to give the primary products ClO + O on the ground state and/or the minor products Cl + O_2 on the $^2B_2$ state. The change in the relative yield, the kinetic energy release, and the increase or decrease in the rates with selective vibrational modes (*e.g.*, bending or asymmetric vibrations) are

consistent with our picture. Furthermore, the change in bonding upon excitation, the nature of the transition-state on both surfaces, and the calculated rates of the reaction support the conclusion. Some comments on the relevance of line width measurements are made, emphasizing the insensitivity of the width to the dynamics of the intermediates and the inhomogeneity due to overlapping resonances and rotational convolutions.

The observed ClO transient reflects two different contributions: ionic fragmentation, showing a similar (but time-shifted) transient as the parent $OClO$ at short delay times, and neutral fragmentation leading to a final non-zero value of ClO^+ at longer delay times. It was shown that the neutral fragmentation of $OClO$ excited by a femtosecond laser pulse at 308 nm leads to ClO formation on a time scale of a couple of hundred femtoseconds. Previous work reported no ClO appearance up to several hundred nanoseconds.

The preliminary studies of $OClO$ clusters with water, $(OClO)_n(H_2O)_m$ with n ranging from 1 to 3 and m from 0 to 3, opens up the possibility to study the heterogeneous photochemistry of these species in the time domain. We hope to extend the femtosecond dynamics studies reported here to these clusters and also to lower energies in isolated $OClO$ and the related systems of $ClOCl$ and $ClONO_2$.[60] Theoretical wave packet 2-*d* studies, similar to those made on IHgI,[19] are part of these efforts.

References

[1] J. L. Gole, J. Phys. Chem. **84,** 1333 (1980).

[2] S. Michielsen, A. J. Merer, S. A. Rice, F. A. Novak, K. A. Freed, and Y. J. Hamada, J. Chem. Phys. **74,** 3089 (1981).

[3] D. A. McDonald and K. K. Innes, Chem. Phys. Lett. **59,** 562 (1987).

[4] E. C. Richard, T. W. Jones, and V. Vaida, J. Phys. Chem. **93,** 6346 (1989).

[5] J. H. Glownia, J. Misewich, and P. P. Sorokin, in *Supercontinuum Lasers,* edited by R. R. Alfano (Springer, Berlin, 1990), pp. 370.

[6] W. G. Lawrence, K. C. Clemitshaw, and V. A. Apkarian, J. Geophys. Res. **95,** 18591 (1990).

[7] E. Ruehl, A. Jefferson, and V. Vaida, J. Phys. Chem. **94,** 2990 (1990).

[8] E. Bishenden, J. Haddock, and D. J. Donaldson, J. Phys. Chem. **95,** 2113 (1991).

[9] E. C. Richard and V. Vaida, J. Chem. Phys. **94,** 153 (1991).

[10] E. C. Richard and V. Vaida, *J. Chem. Phys.* **94,** 163 (1991).

[11] H. F. Davis and Y. T. Lee, J. Phys. Chem. **96,** 5681 (1992).

[12] K. A. Peterson and H. J. Werner, J. Chem. Phys. **96,** 8948 (1992).

[13] V. Vaida, E. C. Richard, A. Jefferson, L. A. Cooper, R. Flesch, and E. Ruehl, Ber. Bunsenges. Phys. Chem. **96,** 391 (1992).

[14] V. Vaida, S. Solomon, E. C. Richard, E. Ruehl, and A. Jefferson, Nature **342,** 405 (1989).

[15] A. Wahner, G. S. Tyndall, and A. R. Ravishankara, J. Phys. Chem. **91,** 2734 (1987).

[16] D. S. Bethune, A. J. Schell-Sorokin, J. R. Lankard, M. M. T. Loy, and P. P. Sorokin, in *Advances in Laser Spectroscopy,* Vol. 2, edited by B. A. Garetz and J. R. Lombardi (1983), p. 1.

[17] R. M. Bowman, M. Dantus, and A. H. Zewail, Chem. Phys. Lett. **156,** 131 (1989).

[18] M. Dantus, R. M. Bowman, M. Gruebele, and A. H. Zewail, J. Chem. Phys. **91,** 7437 (1989).

[19] M. Gruebele, G. Roberts, and A. H. Zewail, Phil Trans R. Soc. Lond. A **332,** 35 (1990).

[20] A. W. Richardson, R. W. Redding, and J. C. D. Brand, J. Mol. Spectrosc. **29,** 93 (1969).

[21] The rotational constants of OClO have been determined in Ref. 20 and references therein. Relevant to this work, from the available data, we calculate the rotational dephasing (see P. M. Felker and A. H. Zewail, J. Chem. Phys. **86,** 2460 (1987)) based on the values of the constants: $A = 1.056$ cm^{-1}; $B = 0.309$ cm^{-1}; and $C = 0.281$ cm^{-1}. At a rotational temperature of ~50 K, we calculate a dephasing time of ~1 ps, longer than the observed time scales of the decay. This indicates the insignificance of the rotational contribution to the initial decay. The lack of large polarization anisotropy on the signal is most likely due to the 4-photon MPI mode of probing.

[22] J. W. Perry, N. F. Scherer, and A. H. Zewail, Chem. Phys. Lett. **103,** 1 (1983).

[23] L. R. Khundkar, J. L. Knee, and A. H. Zewail, J. Chem. Phys. **87,** 77 (1987).

[24] J. L. Knee, L. R. Khundkar, and A. H. Zewail, J. Chem. Phys **87,** 116 (1987).

[25] T. Baumert, M. Grosser, R. Thalweiser, and G. Gerber, Phys. Rev. Lett. **67,** 3753 (1991).

[26] M. Dantus, M. H. M. Jansen, and A. H. Zewail, Chem. Phys. Lett. **181,** 281 (1991).

[27] G. Herzberg, *Molecular Spectra and Molecular Structure III. Electronic Spectra and Electronic Structure of Polyatomic Molecules* (D. Van Nostrand Company Inc., 1966).

[28] E. W. Schlag and H. J. Neusser, Acc. Chem. Res. **16,** 355 (1983).

[29] D. P. Taylor and P. M. Johnson, J. Chem. Phys. **98,** 1810 (1993) and references therein.

[30] L. R. Khundkar and A. H. Zewail, Chem. Phys. Lett. **142,** 426 (1987).

[31] M. J. Rosker, M. Dantus, and A. H. Zewail, J. Chem. Phys. **89,** 6113 (1988).

[32] T. Baumert, R. Thalweiser, V. Weiss, and G. Gerber, Z. Phys. D. **26**, 131 (1993).

[33] R. I. Derby and W. S. Hutchinson, Inorg. Synth. **4**, 152 (1953).

[34] R. Flesch, E. Ruehl, K. Hottmann, and H. Baumgaertel, J. Phys. Chem. **97**, 837-844 (1993).

[35] N. Basco and R. D. Morse, Proc. R. Soc. Lond. A. **336**, 495 (1974).

[36] J. A. Coxon, Can. J. Phys. **57**, 1538 (1979).

[37] T. Baumert, V. Engel, C. Meier, and G. Gerber, Chem. Phys. Lett. **200**, 488 (1992).

[38] D. K. Bulgin, J. M. Dyke, N. Jonathan, and A. J. Morris, Chem. Soc. Faraday Trans. 2 **75**, 456 (1978).

[39] L. R. Khundkar and A. H. Zewail, Annu. Rev. Phys. Chem. **41**, 15 (1990).

[40] A. H. Zewail, Faraday Discuss. Chem. Soc. **91**, 207 (1991).

[41] Q. Liu and A. H. Zewail, J. Phys. Chem. **97**, 2209 (1993).

[42] P. M. Felker and A. H. Zewail, Adv. Chem. Phys. **87**, 265 (1988) and references therein.

[43] J. Kommandeur, W. A. Majewski, W. L. Meerts, and D. W. Pratt, Ann. Rev. Phys. Chem. **38**, 433 (1987) and references therein.

[44] D. H. Semmes, J. S. Baskin, and A. H. Zewail, J. Chem. Phys. **92**, 3359 (1990).

[45] J. L. Herek, S. Pedersen, L. Banares, and A. H. Zewail, J. Chem. Phys **97**, 9046 (1992).

[46] J. L. Knee, F. E. Doany, and A. H. Zewail, J. Chem. Phys. **82**, 3359 (1985).

[47] A. Lorincz, D. D. Smith, F. Novak, R. Kosloff, D. J. Tannor, and S. A. Rice, J. Chem. Phys. **82**, 1067 (1985).

[48] J. L. Knee, L. R. Khundkar, and A. H. Zewail, *J. Phys. Chem.* **89**, 3201 (1985).

[49] For pure IVR on one PES, bi-exponential decay is also predicted.[42] However, one does not obtain selectivity in ionization from the initial and final vibrational levels unless intermediate states are involved or near-threshold ionization is used as selective means for the FC factors. In the case of OClO,

there was no change in form over the energy range studied; this fact is hard to reconcile with IVR on one surface. It should be noted that for the coupling scheme of two surfaces (Fig. 6.11), if we consider reversibility then a bi-exponential decay is also predicted even if the initial state is the only one ionized. Because of the relative density of states, we invoked MPI out of the two states, but this is not cardinal if reversibility is strong.

[50] The calculations were performed using the Whitten-Rabinovich approximation and compared to a direct count RRKM routine provided by C. Lienau from the J. Troe group. Both programs gave the same result. For example, at 310 nm, ρ (E) = 1.18/cm^{-1} and $N^{\ddagger}$ = 212, where at 350 nm, ρ (E) = 0.9/cm^{-1} and $N^{\ddagger}$ = 114 for the X^2B_1 state. In the direct count we obtained ρ (E) according to:

$$\rho(E) \ = \ \frac{1}{\Delta v} \sum_{i=1}^{\Delta v} \rho_i (E_i)$$

where Δv is the laser bandwidth (cm^{-1}) and $\rho_i(E_i)$ is the density of states per cm^{-1}, in increments of 1 cm^{-1}.

[51] S. J. Klippenstein, L. R. Khundkar, A. H. Zewail, and R. A. Marcus, J. Chem. Phys. **89**, 4761 (1988).

[52] G. A. Brucker, S. I. Ionov, Y. Chen, and C. Wittig, Chem. Phys. Lett. **194**, 301 (1992).

[53] A. Arkell and I. Schwager, J. Am. Chem. Soc. **89**, 5999 (1967).

[54] S. Pedersen, L. Bañares, and A. H. Zewail, J. Chem. *Phys.* **97**, 8801 (1992).

[55] D. M. Neumark, Ann. Rev. Phys. Chem. **42**, 153 (1992) and references therein.

[56] L. J. Butler, Chem. Phys. Lett. **182**, 393 (1991).

[57] G. Porter and F. J. Wright, Discuss. Faraday Soc. **14**, 23 (1953).

[58] G. Porter, in *The Chemical Bond - Structure and Dynamics*, edited by A. H. Zewail (Academic Press, Inc., San Diego, 1992), p. 113.

[59] H. S. Johnston, Ann. Rev. Phys. Chem. **43**, 1 (1992) and references therein.

[60] T. K. Minton, C. M. Nelson, T. A. Moore, and M. Okumura, Science **258**, 1342 (1992).